A Noninvasive Biomechanical Approach for Application to Cell Physiology and Developing Organs

Etienne Marcelin Mfoumou

A Thesis
In the Department
of
Mechanical and Industrial Engineering

Presented in Partial Fulfillment of the Requirements
For the Degree of
Doctor of Philosophy (Mechanical and Industrial Engineering) at
Concordia University
Montreal, Quebec, Canada

September 2012

CONCORDIA UNIVERSITY
SCHOOL OF GRADUATE
STUDIES

This is to certify that the thesis prepared

By: **Etienne Marcelin Mfoumou**

Entitled: **A noninvasive biomechanical characterization approach for application to cell physiology and developing organs**

and submitted in partial fulfillment of the requirements for the degree of

DOCTOR OF PHILOSOPHY (Mechanical Engineering)

complies with the regulations of the University and meets the accepted standards with respect to originality and quality.

Signed by the final examining committee:

Chair
Dr. C. Mulligan

External Examiner
Dr. B. Tan

External to Program
Dr. R. Zmeureanu

Examiner
Dr. C. Y. Su

Examiner
Dr. S. Rakheja

Thesis Co-Supervisor
Dr. I. Stiharu

Thesis Co-Supervisor
Dr. S. Narayanswamy

Approved by
Dr. A. Dolatabadi, Graduate Program Director

September 13, 2012

Dr. Robin A.L. Drew, Dean
Faculty of Engineering and Computer Science

ABSTRACT

A noninvasive biomechanical characterization approach for application to cell physiology and developing organs

Etienne Mfoumou, Ph.D.

Concordia University, 2012

The current focus of biomedicine is on the genomics and proteomics basis of disease, resulting from changes in biophysical or biochemical properties of living cells. These alterations have been commonly viewed as the end-result of the disease process, but recent advances in mechanobiology and nanotechnology suggest that cell and tissue responses to mechanical or chemical stress may actively contribute to the progression or delay of diseases. Meanwhile, current bioassays for investigating these issues are invasive, expensive and time consuming. In order to address these limitations, this thesis opens a new avenue on fast, noninvasive and low cost techniques to study the physiology of biological systems; these techniques make use of vibration monitoring, ultrasound irradiation, spectrophotometry, as well as emerging trends in nanotechnology.

First, the gene expression profile of human normal bronchial epithelial cells was compared with single-wall carbon nanotubes-treated cells, and revealed significant changes in the expression of specific genes. This served as a first step in clarifying the mechanisms of action and investigating the toxicity in this model. Next, an alternative way to assess cell toxicity based on spectrophotometry and the density of cell culture medium is presented. Different cell lines and different levels of substrate's physico-chemical modifications were analyzed. It is shown, using immunocytochemistry that

changes in substrate's mechanical properties can trigger cell differentiation and changes in phenotype. Spectrophotometry of a micro-volume of the culture medium also allowed quantitative assessment of cell toxicity, with no need of cell detachment. Moreover, the role of ultrasound on the key genes associated with cell proliferation and invasion was investigated. We consistently found that low power ultrasound inhibits cell proliferation and cell invasion by down-regulating specific corresponding proteins. We further moved from single cells to groups of organized cells and applied an eigenvalue solution approach to study the modal parameters of a simplified model of chick embryo. These parameters are obtained using both the Mode Indicator Functions (MIF) and an implemented inverse problem based on least squares approach using the Prony method, even when the mechanical excitation cannot be controlled. This is important for the understanding of damages of developing groups of organized cells when exposed to vibration or shock.

Overall, the techniques presented offer the opportunity to minimize the use of invasive diagnosis methods while avoiding loss time loss due to repeated investigations of different sets of samples. Hence, they provide new avenues for noninvasive characterization of cells or cell aggregates in response to different types of excitation.

ACKNOWLEDGEMENTS

I would like to express my sincere thanks to my supervisors, Dr. Sivakumar Narayanswamy and Dr. Ion Stiharu, for their guidance, support, and continuous encouragement throughout my doctoral study. Their genuine enthusiasm for this research topic created an atmosphere that was truly instrumental in the success of this work. It was a privilege to carry out research under their supervision.

I would also like to thank Dr Ala-Eddin Al Moustafa for his unwaivering encouragement and support. I am grateful to have been offered the opportunity to work in his lab at the Lady Davis Institute for Medical Sciences at the Jewish General Hospital in Montreal. His mentorship has allowed me to be able to bring my contribution at the interfaces of engineering with medicine and life science, toward the development of novel noninvasive techniques. My thanks are also extended to members of his lab, in particular Amal Kassab and Amber Yasmeen for their help on bioassays.

Finally, I would like to thank my family and friends for their unconditional support during my studies. My profound gratitude goes to my wife Liliane Souga, for her patience, understanding, and unconditional support and help.

This thesis is dedicated to my wife Liliane, and my twins Elda and Soraya who were born during my doctoral study.

Table of contents

List of abbreviations

AFM	Atomic Force Microscopy
BDM	2,3 butanedione monoxime
BT	Breast Tumor
CAS	Chemical Abstracts Services
CDK	Cyclin Dependent Kinase
cDNA	Complementary DNA
CNT	Carbone Nanotube
CPCI-S	Conference Proceedings Citation Index
DMEM	Dulbecco's Modified Eagle's Medium
FBS	Fetal Bovine Serum
DNA	Deoxyribonucleic acid
DOF	Degree Of Freedom
ECM	Extracellular medium
EGF	Epidermal Growth Factor
FACS	Fluorescence Activated Cell Sorting
FAK	Focal Adhesion Kinase
FRF	Frequency Response Function
FTIR	Fourier Transform Infrared
FUS	Focused Ultrasound
HEPES	(4-(2-hydroxyethyl)-1-piperazineethanesulfonic acid)
HNBE	Human Normal Bronchial Epithelial

HPV	Human papillomavirus
IR	Infrared
MEMS	Micro-electro-mechanical-system
MIF	Mode Indicator Function
NAC	Nucleic Acid Concentration
NEF	Normal Embryonic Fibroblast
PBS	Phosphate Buffer Saline
PDMS	Polydimethylsiloxane
PVDF	Polyvinylidene difluoride
RNA	Ribonucleic acid
RPMI	Roswell Park Memorial Institute
RT-PCR	Reverse Transcription - Polymerase Chain Reaction
SCI	Science Citation Index
SWCNT	Single-Wall Carbon Nanotube
TCP	Tissue Culture Plate
US	Ultrasound
UV	Ultraviolet
WoS	Web of Science

List of symbols

a	Amplitude attenuation coefficient
a	Radius of inclusion (chapter 7)
a_s	Scattering coefficient
A	Residue
b	Viscosity
B	Normalized amplitude
c	Concentration of a colored compound
c_i	Damping of element i
c_0	Sound speed in the medium
C_m	Specific heat per unit mass
C	Damping matrix
E	Young's modulus
f	Frequency
F	Force
H	Frequency Response Function
$h(t)$	impulse response function
I	Intensity transmitted (sound or light)
I_0	Intensity at initial distance
k_i	Stiffness of element i
K	Stiffness matrix
l	Path length of light in a solution

m_i	Mass of element *i*
M	Mass matrix
p	Acoustic pressure amplitude away from the transducer
p_0	Acoustic pressure amplitude at the surface of the transducer
Q	Modal scaling factor
x	distance
T	Temperature
t	Time
u	Sound field
ω	Angular frequency
Z	Normalized distance
α	Absorption coefficient
ε	Nonlinear parameter
μ	Shear elasticity
θ	Angle
λ_r	System pole
Ψ_r	Mode shape
ψ	Modal coefficient
ρ	Density
$[\,]$	Matrix

List of figures

List of tables

CHAPTER 1. INTRODUCTION AND LITERATURE REVIEW

1.1 Brief history and applications

1.1.1 Introduction

The morphological, physiological, structural, genetical, biophysical, biochemical and antigenic features of the tumoral cells provide the numerous targets for chemotherapy, genetic therapy, immunotherapy and biochemical therapy of malignant diseases [1-3]. Despite the fact that there has been continuous progress in cancer diagnosis and treatment as a result of recent discoveries in cellular and molecular oncobiology, structural and functional genomics, proteomics and metabolomics, pharmacogenomics and toxicogenomics, antineoplastic treatment is still of little effectiveness [4-8]. One of the most significant objectives of contemporary studies consists in improving approaches to control the carcinogenesis. In this fight against cancer, chemotherapy is the most prominent approach. Meanwhile, it is of little effectiveness because of its negative impact on normal cells. Consequently, for improving oncochemotherapy, it is necessary to extend research programs on potential new oncolytic agents or therapeutic ways that would specifically target tumor cells.

In light of the above affirmations, supplementary researches have been required in order to improve the understanding of cytophysiology and development process of cell aggregates. Translational research is an effective key for this purpose and nanoparticles, acoustic irradiation, mechanotransduction as well as vibration analysis have been shown

to potentiate a better understanding of action mechanisms at cell aggregate, cellular, sub cellular and molecular levels.

1.1.2 Carbon nanotubes and cellular functions in vitro

Nanomaterials and nanotechnology is in forefront of materials research. Nanotechnology involves utilizing materials which possess at least one physical dimension between 1 and 100 nm to construct structures, devices, and systems that have novel properties. This area of research has raised a strongly increasing interest among researchers.

Indeed, many biological components, such as DNA, involve some aspect of nano-dimensionality. In the imminent ageing society of the 21st century, nonmaterial have been widely investigated for potential application in the medical field [9,10]. In this context, the nano-dimensionality of nature has logically given rise to the interest in using nanomaterials to prepare scaffolds for tissue engineering. These materials have the potential to induce a significant impact on tissue engineering [11-14]. Carbon nanotubes (CNTs), one of the most representative nonmaterial, with unique electrical, mechanical, and surface properties, were first reported in the year of 1991 and up to now appear well suited as a biomaterial [14-29]. Its popularity is illustrated in Figure 1-1 below; the figure presents the total number of articles covered by SCI shown as a rough measure for the growth of scientific literature.

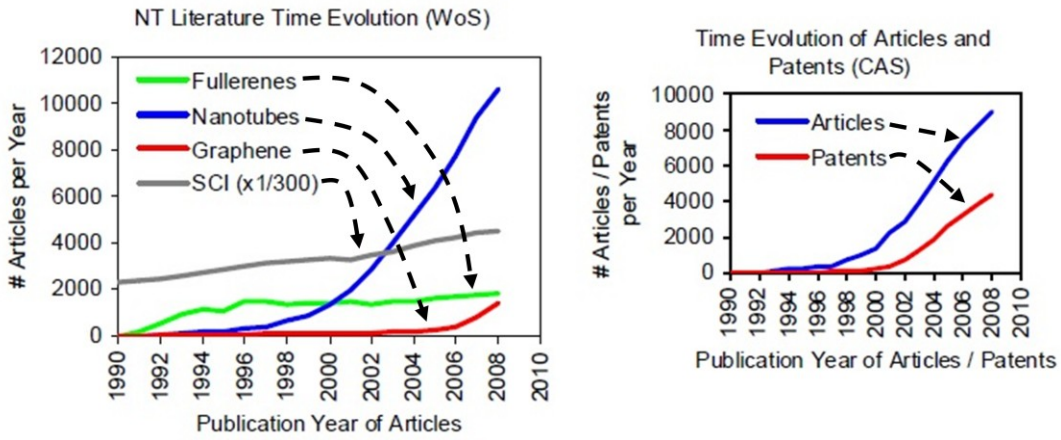

Figure 1-1 Time dependent number of articles Left: Dealing with fullerenes, nanotubes, and graphene (Source: SCI and CPCI-S under WoS). Right: Dealing with nanotubes and covered by the CAS literature file (Source: CAplus under STN International).

Several other studies have been carried out on the interaction between CNTs and a variety of cells including osteoblasts, showing CNTs to be excellent substrates for cellular attachment and growth [30-38]. An important feature of functionalized CNTs (f-CNTs) is their high propensity to cross cell membranes, allowing their use for the delivery of therapeutically active molecules [39]. For instance, Liu et.al. [40] have described attaching RNA to CNTs, which enter T cells and deliver the RNA and when placing T cells in a solution of CNT-RNA complex, receptor proteins on the cell surfaces went down by 80 percent.

Despite the significance of studies on this topic, there is a clear discrepancy in the literature about CNTs uptake mechanisms (phagocytosis, diffusion and endocytosis). These discrapencies are attributed to the differences in chemical and physical properties of tested nanotubes (degree of dispersion, formation of supramolecular complexes and

nanotube length). Meanwhile, it has been recently demonstrated that their uptake seems to be independent of functional groups on CNT surface [41]. Further findings related to the clarification of CNTs' mechanisms of action and investigation of toxicity are presented in this thesis.

1.1.3 Spectrophotometry in cell biology

A study of the interaction of light (or other electromagnetic radiation) with matter is an important and versatile tool for the physicist. Indeed, much of our knowledge of chemical substances comes from their specific absorption or emission of visible light. Therefore, absorption spectrophotometry has been a widely used technique in analytical chemistry based on the property of molecules to absorb light at specific wavelengths.

A spectrophotometer consists of two instruments, namely a spectrometer to produce light of any selected color (wavelength), and a photometer to measure the intensity of light. The instruments are designed so that the liquid sample can be placed between the spectrometer beam and the photometer, which delivers a voltage signal to a display device. This signal changes as the amount of light absorbed by the liquid sample changes. A typical block diagram of a single beam spectrophotometer is illustrated in Figure 1-2. The prism serves as the dispersing device while the monochromator refers to the dispersing device (prism), entrance slit, and exit slit. The exit slit is moveable in the vertical direction so that those portions of the power spectrum produced by the power source (light source) that are to be used can be selected.

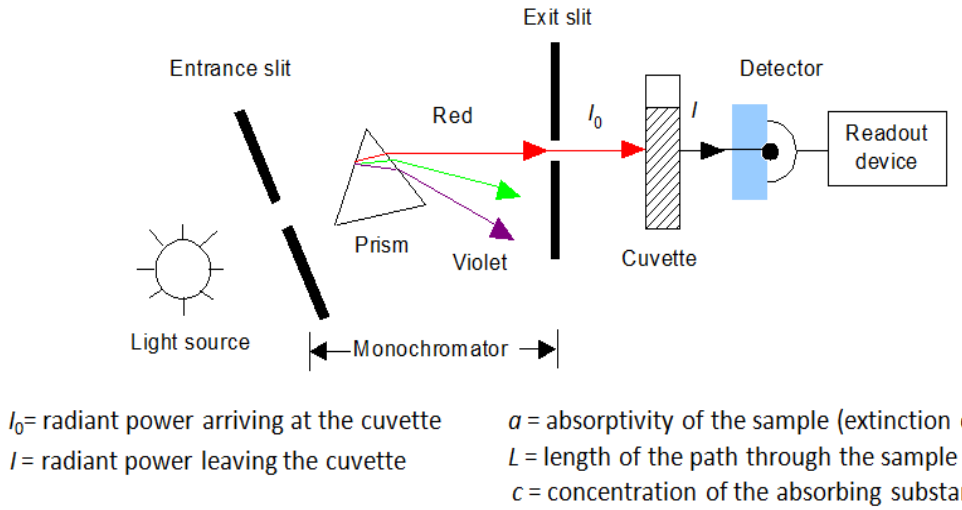

Figure 1-2 Block diagram of a single beam spectrophotometer.

In the infrared range, FTIR spectroscopy is a vibrational spectroscopic technique that has been used to optically monitor the molecular changes associated with diseased tissues. This technique aims at finding more conservative approaches to measure characteristics within tumor tissue and cells, yielding accurate and precise assignment of the functional groups, bonding types, and molecular conformations. It has the advantage of being relatively simple, reproducible, non-destructive to the tissue, and only small amounts of sample with a minimum sample preparation are required. Moreover, expensive reagents are avoided and due to the longer wavelength of IR compared to UV or visible radiation, it penetrates to a greater depth and is absorbed with less scattering by the tissue or cells.

The frequency band in IR technology is given in units of reciprocal centimeters (cm^{-1}) rather than hertz (Hz), because the numbers are more convenient. The reciprocal centimeter is the number of wave cycles in one centimeter; whereas, frequency in cycles

per second or Hz represents the number of wave cycles in $3x10^{10}$ cm (distance covered by light in one second). Wavelength units are in micrometers or microns (μ) instead of nanometers for the same reason. Attempts to apply this technology to biology began as early as the 1910s, when the use of IR spectroscopy for the analysis of biological samples was first suggested. By the late 1940s, the technique was being successfully explored for investigation of biological materials and therefore, has become an accepted method to characterize biomolecules [42]. A wide range of biological studies have been covered by FTIR analysis. In the study of cervix, Wood et al. [43] reported on FTIR spectroscopy as a biodiagnostic tool for cervical cancer. In their study, the spectra of the normal epithelial cells illustrated intense glycogen bands at 1022 cm^{-1} and 1150 cm^{-1}, as well as a pronounced symmetric stretch at 1078 cm^{-1}. This study demonstrated the potential of the automated FTIR cervical screening technology in the clinical setting. The same group carried out an FTIR micro spectroscopic investigation of cell types and potential confounding variables in screening for cervical malignancies [44]. They found that leukocytes, and particularly lymphocytes, have spectral features in the phosphodiester region (1300 - 900 cm^{-1}), which suggests changes indicative of malignancy. Sindhuphak et al. [45] also screened 275 cervical cell samples of Thai women undergoing hysterectomy and compared the results to histology. FTIR results versus histology showed sensitivity of 96.3% and specificity of 96.4%, whereas false-negative and false-positive rates were respectively 3.7 and 3.6%. Another study has been conducted by Mordechai et al. [46] based on formalin-fixed melanoma and cervical cancer to detect common biomarkers that occur in both types of cancer, compared to the respective non-malignant tissues. In this study, the spectra were analyzed with a target on biomolecules

such as RNA, DNA, phosphates and carbohydrates. they found that carbohydrate levels showed a good diagnostic potential for detection of cervical cancer. On the other hand, variation of the RNA/DNA ratio as measured at 1121/1020 cm^{-1} showed similar trends between non-malignant and malignant tissues in both types of cancer, with a higher ratio for malignant tissues.

In the study of lung, Wang et al. [47] investigated lung cancer cells in pleural fluid and showed significant spectral differences between normal, lung cancer and tuberculous cells. The most considerable differences were found in the ratio of peak intensities of 1030 and 1080 cm^{-1} bonds, which mainly originate in glycogen and phosphodiester groups of nucleic acids. Yano et al. [48] have focused on direct measurement of human lung cancerous and non-cancerous tissues for the assessment of the efficiency of using FTIR as a clinical tool. They found that peaks obtained from bands at 1045 cm^{-1} and 1465 cm^{-1}, originating from glycogen and cholesterol, were exceptionally useful factors in discriminating cancerous tissues from non-cancerous ones. Yang et al. [49] investigated tumor cell invasion and compared the FTIR results with histology. They generated mapping images of a three-dimensional artificial membrane made of collagen type I (one of the main components of basal membranes of the lung tissue), and validated with standard histological section analysis. The FTIR image produced using a single wave number at 1080 cm^{-1}, corresponding to PO^{-}_{2} groups in DNA from cells, correlated well with histology, which clearly revealed a cell layer and invading cells within the membrane. Moreover, the peaks corresponding to amide A, I and II in the spectra of the invading cells shifted compared to the non-invading cells; this may relate to the changes in conformation and heterogeneity in the phenotype of the cells. Their data demonstrated

that FTIR can be used as a fast and reliable technique in the assessment of tumor invasion in vitro.

Other applications of FTIR analysis covered in the literature deal with breast [50,51], gastrointestinal tissue [52-55], brain [56-58], prostate [59,60], colon [61-64], and others [65-73]. However, little is known in the literature on the use of cell culture media, instead of the cells directly, to address these issues, making up one of the targets of this work, presented later in the thesis.

1.1.4 Physico-chemical substrate modification for in vitro cell growth

The first idea on how cells surrounding environment, the ECM, affects the cellular adhesion and motility is to investigate the effect of chemical or biological changes. Several studies in the literature focus on how substrate mechanical changes influence cellular adhesion and motility [74-77]. These works have allowed explaining the impact of substrate mechanical properties in many fundamental biological processes such as embryo-genesis [78], phagocytosis [79-82], or metastases development [76,83]. However nanosized chemical domains, which are present in the local cellular environment, can be difficult or expensive to produce and their effects on cellular behaviour have not been widely studied. One versatile and easy to implement method for producing such nanosized features on different types of substrates is plasma lithography. This technique makes use of low energy plasma modification to spatially change the surface chemistry of a substrate. Exposed to typical air (or oxygen) plasma interacting with the polymer substrate, the cell contacting surface becomes hydrophilic and presents altered functional groups which can then have the effect of being more amenable to cell growth [84,85].

This technique has been used, among other applications, to pattern surfaces for self assembly of nanoparticles and proteins [86,87], as well as cells [88,89].

In a cross disciplinary approach, the effects of cross-linker concentration and curing time on PDMS rigidity, and the effect of different plasma treatments on PDMS surface hydrophobicity was recently investigated [90]. This study showed that adequate tuning of the PDMS surfaces physical chemistry can control the fibroblast adhesion and morphology, and this is in direct relation to tissue modelling and reorganization.

1.1.5 Acoustic and vibration of cells, similarities with developmental biology

Ultrasound is a mechanical wave with periodic vibrations of particles in a continuous and elastic medium at frequencies above 20 kHz. In liquids, its velocity (about 1000 to 1700 m/s) translates into wavelengths of the order from micrometers to centimeters. As a consequence, the acoustic field produced cannot couple with energy at the molecular level. Therefore, US can be perceived as a safe approach with a good tissue penetrating ability, which is an excellent feature from a clinical point with a prompted extensive evaluations for medical purposes [91]. This technique has been in routine use for diagnostic imaging of soft tissue. Therapeutic applications have been related to the thermal effects caused by US absorption hyperthermia and thermal ablation. The interaction of US with liquid is known to be accompanied by the phenomenon of cavitation, which yields an enormous concentration and conversion of the diffuse sound energy.

Unlike thermal applications of US, the therapeutic use of the non-thermal effects have been less studied, although cavitation causes chemical reactions (sonochemistry) and these reactions might have some biological implication in vivo. However sonochemistry, while exhibiting unique features, shares some characteristics with combustion and radiation chemistry [92]. Moreover, sonodynamic therapy approach is based on the synergistic effect of US and sonosensitizers; this effect can be localized by focusing the US on a well defined region and choosing compounds with tumor-affinity [93,94]. This study has led to a review on the ability to enhance drug cytotoxicity with US that enables efficient but localized effects on a pathological region, with minimal damage to surrounding healthy tissue [95]. Other recent studies of US approaches for targeted drug delivery and nonviral gene transfection has revealed new possibilities [96-98]. These studies used contrast agents to facilitate delivery and suggested that US delivery resulted from cell sonoporation. Using voltage-clamp techniques, Pan et al. [99] obtained real-time measurements of sonoporation of Xenopus oocyte (commonly used cell for electrophysiological recordings) in the presence of Optison (an agent consisting of albumin-shelled gas bubbles). Indeed, US increased the transmembrane current as a direct result of decreased membrane resistance due to pore formation, and they discovered that the resealing of cell membrane following US exposure required calcium ions entering the cell through US-induced pores.

Other works are reported in the literature based on pulsed FUS (pFUS). This technique, despite utilizing relatively high intensities (1000-2000 W/cm^2), uses non-continuous exposures that lower the energy deposition rate while allowing cooling to occur between pulses, thereby minimizing thermal effects and enhancing effect created by non-thermal

mechanisms [100,101]. This technique has shown promise for a variety of applications including drug and nanoparticle delivery, but little is known about the effects these exposures have on tissue, specifically with regard to cellular pro-homing factors (growth factors, cytokines and cell adhesion molecules). Consequently, Burks et al. [102] examined changes in murine hamstring muscle following pFUS and demonstrated that it has little effect on the histological integrity of muscle and does not induce cell death. Meanwhile, the observed molecular changes in muscle were found to potentially be utilized to target cellular therapies by increasing homing to areas of pathology. A representative result of their work is shown in Figure 1-3. Blue represents DAPI-stained nuclei and green represents TUNEL-positive nuclei. No apoptotic nuclei were observed following pFUS or in untreated control muscle at the same time points. However, several apoptotic nuclei were observed near the margin of the cFUS treatment volume following cFUS treatment.

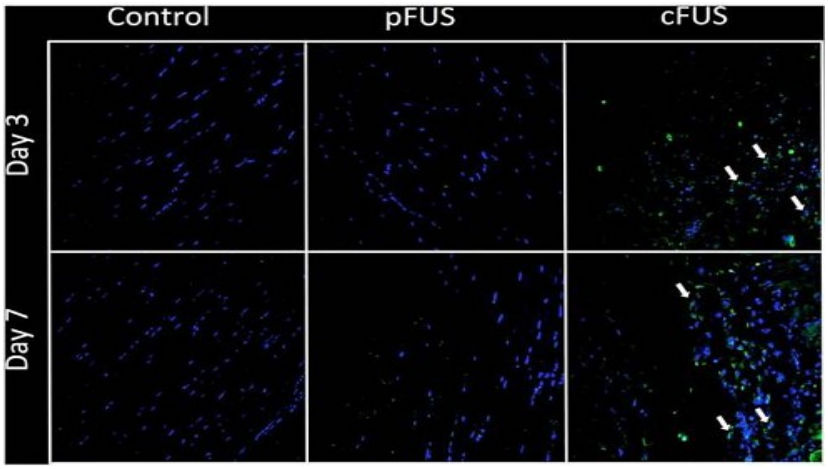

Figure 1-3 Effect of FUS on apoptosis.

In order to further the understanding of living cells, researchers have focused on developmental biology in the literature. This branch of biology covers the total development process from the zygote to the adult with special focus on the embryo, because the embryo is a transition between genotype and phenotype [103]. In 1892, the French biologists Lobstein and Recamier speculated the concept of the embryonic origin of tumours. In 1970s, Pierce [104] proposed a theory based on cancer as a developmental biology and pointed out that tumourigenesis concerned intimately with developmental biology in a large extent. With the recent advances in the fields of developmental biology, molecular biology, tumour immunology and experimental embryology, it appears that the development of early embryo shares many similarities with cancer development with regard to both biological behaviours and molecular basis [105,106]. This has promoted the merging of developmental biology and cancer biology. As such, the co-culture of early embryos and cancer cells is an important means to observe the biological behaviour changes of either embryos or cancer cells in vitro. Zhang et al. [107] co-cultured mouse embryo with malignant tumor cells, investigated the development of blastocyst by observing the hatchment, attachment and outgrowth. Then they observed the changes of cancer cells in the embryonic circumstances, and detected the proliferation and apoptosis of cancer cells. They found that the embryos developed normally in the tumor environments, and the rate of hatchment, attachment and outgrowth increased significantly. They also observed that under the co-culture system, the early embryo developed normally, as well as the cancer cells. They concluded that there may be similarities between the embryos and cancer cell's choice of living. Other papers reported in the literature deal with migration and invasion [108], gene expression and protein

profiles [109], signaling pathways [110,111], cell differentiation [112], the mechanism of immune escape [113], and others. These can all be related to the techniques presented in this thesis, toward a better understanding of concepts in developmental biology.

1.2 Thesis motivation

The multidisciplinary approach adopted in this thesis is focusing on the synergistic interaction between mechanical engineering, cellular physiology and developmental biology that is expected to lead to substantial scientific progress toward the understanding of cancer treatment. With respect to fundamental research, this thesis is placed in the context of a lack of knowledge on the influence of nanoparticles as well as ultrasound irradiation on the protein content and potential differentiation of adherent cells. Ultrasound extends over almost ten orders of magnitude of the acoustic frequency range, most of which is unexplored in biology. The understanding of the effect of CNTs on cells is important because nanomaterials have promise in medicine, such as acting as vehicles to deliver drugs to specific cells or to specific locations in the human body. By fully understanding their interaction, the scientific community will be able to conceivably design products that heal cells rather than harm them or the inverse. This motivation also applies to the understanding of the effect of cellular transduction by changing the substrate mechanical or chemical properties in vitro, mimicking the in vivo ECM.

The thesis emphasizes the importance of mechanotransduction on the understanding of cellular physiology and developmental biology. Spectrophotometry of cell culture media, direct US exposure of cancer cells, vibration analysis and modal parameters extraction are used as high-sensitive tools to characterize and induce changes in biological samples.

Consequently, new methods of non-invasive diagnostics and therapy can be developed based on the above acquired knowledge.

Overall, a better understanding of the interactions between mechanical engineering and biology as envisaged in this thesis may help tease out a connection between molecular vibration, cellular dynamics and gene expression. This important view may promote the intersection between developmental biology and cancer biology (tuned by engineering techniques) with twofold implications. On one hand, it enlightens researchers to study cancer from the perspective of developmental biology, which may reveal brand-new diagnostic and therapeutic targets for cancer. On the other hand, it suggests that researchers may envision embryo development as a process of tumour initiation and progression and incorporate decades of accumulation of models and theories on cancer into the investigation of embryogenesis, thus enhancing our in-depth understanding of this process in our life history. As such, there is a great deal of potentially relevant translational research directions in these applications, dealing with the interfaces of mechanical engineering with medicine and life science. Therefore, this thesis explores some of the new avenues in such a cross-disciplinary field of research.

1.3 Thesis objective and scope

The main purpose of this thesis is a prenormative research in the area of engineering non-invasive approaches for triggering, then monitoring and characterizing cells toward the understanding of their metabolism. The work herein presented makes use of standard biological assays, ultrasound excitation of cells, spectrophotometry of the cell culture

medium, plasma lithography, and cell culture substrate mechanoregulation to address the following specific objectives:

(i) The effectiveness of a non-invasive cell conditioning approach to the understanding of cancer biology;

(ii) The effectiveness of performing a micro-volume analysis of cell culture medium (instead of milli-volume analysis nowadays) to understand cellular metabolism;

(iii) The importance of mechanical properties estimation on the understanding of cellular and developmental biology;

(iv) The formulation of an inverse problem to mechanical parameter extraction of cell aggregates.

1.4 Methods

1.4.1 Cellular mechanotransduction

The mechanism by which mechanical forces influence cellular biochemistry and gene expression is obviously difficult to envision, because of the micro-size of cells. In fact, it does not involve a classic coupling between stimulus and response as, for example, in the case of hormonal stimulation, where no molecular signal is present prior to the stimulus and the relevant receptor binding sites are unoccupied. In the presence of hormone stimulus, it binds to its receptor and initiates an intracellular signaling response. In contrast, due to cell shape determined through a balance of mechanical forces [114,115],

any mechanical stimulation that impinges on an adherent cell is acting on a pre-existing force balance (pre-stress). This pre-stress in the cell was reported in the literature to be able to govern the response to mechanical stimulus [116,117].

In the case of adherent cells as used in this thesis, forces applied at the macroscale (through radiation force, mechanical vibration, or substrate stiffness change) will also result in changes in cytoskeletal biomechanics on the micro scale. These changes originating from the ECM will not transfer forces equally on the surface of neighbouring cells. Instead, a tug on the ECM will be felt by the cell via its focal adhesions and hence, via its transmembrane integrin receptors that link to the cytoskeleton. By mechanically stimulating integrins on the surface membrane of cultured cells, these cells respond by increasing recruitment of focal adhesion proteins and mechanically adjust themselves against additional stress [118,119]. By applying the same stress to other transmembrane receptors that do not mediate cell adhesion, there is very little or no response. This is illustrated in Figure 1-4 below. The phase-contrast image of a rat cardiac fibroblast plated on a large grid pattern is shown in (a); the cell creates distortions (arrowheads) by applying force to the elastomer (Young's modulus = 18 kPa). The same cell as in a 10 minutes after BDM-induced relaxation is shown in (b), emphasizing the recovery of the regular grid pattern. Moreover, the phase-contrast image of a contracting cardiac myocyte plated on elastomer with embedded photo resist pattern of dots (Young's modulus = 19 kPa). The dots can be clearly seen even under thick parts of the cell. The arrowheads and the magenta dots underline the pinching action of the contraction on the elastomer. The relaxed phase of the cardiac myocyte is shown on (d).

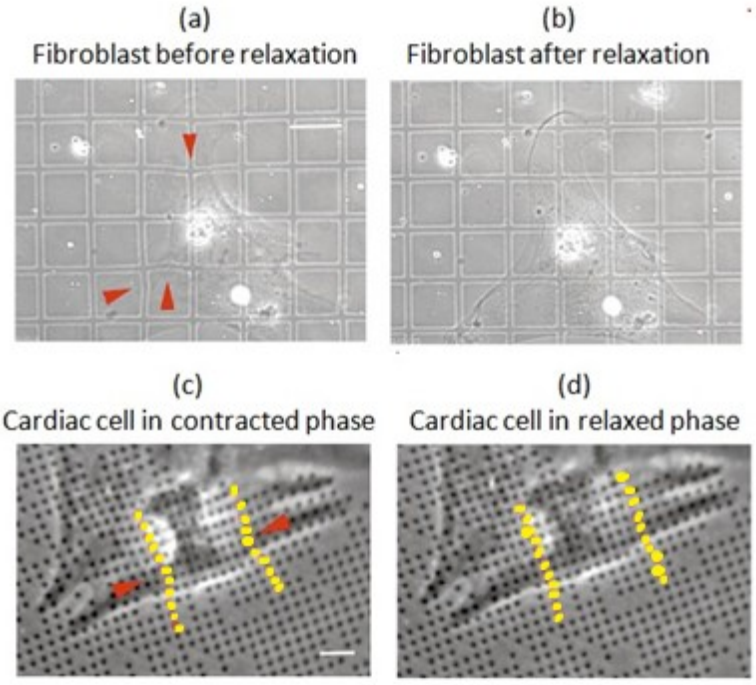

Figure 1-4 Cells plated on the patterned elastomer create distortions [118]

A similar approach is used in this thesis to monitor specific proteins associated with cell proliferation and cell invasion.

1.4.2 Acoustic conditioning of cells: interaction mechanism

The analytical derivations presented in this sub-section and the next one are shown for illustrating the interaction mechanism of cells with an acoustic field. Indeed, for considering the acoustic conditioning of cells used in this thesis towards a potential therapeutic method, it is important to ensure that the temperature rise caused by the absorption of ultrasound by cells is within safe limit. By using standard polystyrene tissue culture plates, the energy of the ultrasonic beam is first traveling through the culturing plate before reaching the cells. Some of the primary energy is absorbed locally through

polystyrene (by various mechanisms including viscous shearing effects and relaxation processes), and this may lead to heating.

Neglecting the path length (1mm) of sound beam through the polystyrene wall as a transmitting medium as well as nonlinear effects such as the influence of the glue attaching the transducer to the bottom of the culturing plate (all of which would make the influence on cells even lower), the acoustic pressure amplitude in the ultrasonic beam at a distance x from a point at which it is p_0 (surface of the transducer) is given by [120]:

$$p(x) = p_0 e^{-ax} \qquad (1.1)$$

where a is the amplitude attenuation coefficient.

In relation to the heating potential of an ultrasonic beam, it is more useful to rewrite the previous equation in terms of the energy flux crossing an area in a specified time, representing the intensity (α^2):

$$I(x) = I_0 e^{-2ax} \qquad (1.2)$$

Where I_0 is the intensity at the point $x = 0$.

The attenuation coefficient is expressed as the sum of the scattering coefficient a_s and the absorption coefficient α giving:

$$a = a_s + \chi \qquad (1.3)$$

To a first approximation, the amount of heating is determined by the magnitude of α. The literature reports measured values of α to be between 60 and 90% of the total attenuation coefficient for different tissues [120]. It is also known that for soft tissues, the attenuation coefficient increases linearly with frequency for the frequency range used in medical ultrasound (250 kHz – 2 MHz for regional generation of heating and mechanical changes in biological tissues, and 2-18MHz for ultrasonography). Moreover, it appears from equation (1.2) that the energy lost by absorption from a beam of intensity *I* crossing a sample (cell) of thickness 10µm is $0.002 \cdot \alpha \ I$. Thus, if there is no heat loss from the absorbing volume, the rate of temperature rise $\frac{dT}{dt}$ is expressed as follows:

$$\frac{dT}{dt} = 0.002 \frac{\alpha \ I}{\rho \ C_m} \qquad (1.4)$$

where ρ is the density, and C_m is the specific heat per unit mass.

For soft tissues, we may take ρ=*1000 k*g.m^{-3}; α = 110 W.m^{-1}MHz^{-1}; C_m = 4180 J.kg^{-1}K^{-1} [120]. This gives a temperature rise of 5.263*10^{-8}**I***f*$^{-1}$ ^{o}C.s^{-1}, where *f* is the frequency in MHz. As a consequence, a temperature rise of 0.0131^{o}C and 0.026 ^{o}C would be anticipated for a 400-kHz, 1-W cm^{-2} and 2-MHz, 1W cm^{-2} respectively continuous exposure during 100 s (in case of no frequency sweep), which is far below the temperature rise that would be considered potentially dangerous (e.g. 1-2^{o}C), as reported by von Schulthess and Smith [121]. In real tissue, heat would be carried out of the sample

volume by convection and conduction, and the final temperature rise would always be less than that predicted by equation (1.4). This disqualifies heat as a leading mechanism behind the observation made under the given experimental conditions, but also shows that the result obtained represents a real biological effect whose relevance in vivo requires careful consideration. The observation would be the same if cells were exposed to pulsed waves, since this type of wave produces less heat than continuous waves. Thus, thermally induced bioeffects are unlikely to be significant when cells are exposed to ultrasound intensities of the order considered in our investigation when suspended in poorly absorbing liquids in vitro.

1.4.3 Acoustic conditioning of cells: numerical analysis with Burger's equation

When a finite amplitude wave propagates in biologic tissues, the nonlinear effects should be considered, including the second harmonic generation, wave distortion and shock wave. The Burger's equation, an ideal tool for this purpose, is a fundamental partial differential equation of the form [122]:

$$ub - uua = \sigma ua \qquad (1.5)$$

This equation describes the evolution of the field *u=u(a,b)* under nonlinear advection and linear dissipation. It occurs in various areas of applied mathematics and is used in this work for analyzing the acoustic field in the cell culture medium because of its simplicity and predictable dynamics. The challenge is to resolve the sharp gradients/shocks when

sound propagates at small and vanishing viscosity and accurately track their evolution. Let's consider Burger's equation in the form [122]:

$$\frac{\partial u}{\partial x} - \frac{\varepsilon}{c_0^2} u \frac{\partial u}{\partial} = \frac{b}{2c_0^3 \rho} \frac{\partial u}{\partial} \tag{1.6}$$

Where u is the sound field, ε is the nonlinear parameter, c_o is the sound speed in the medium, τ is the time, x is the distance in the sound field, ρ_o is the density of the medium, and b is the viscosity. In this form, the equation enables to study in detail various effects that appear in the propagation of waves in dissipative media with a quadratic nonlinearity.

Equation (1.6) is remarkable in that it can be linearized and reduced to the form of an ordinary differential equation of heat conduction. Hence, it is possible to follow the propagation of an initial disturbance of arbitrary form. However, we will consider in this work how the disturbance, given at the input in the form of a harmonic wave, behaves in a situation of small inertial forces in the medium (small values of the Reynolds number).

For simplification purpose, the parameters in equation (1.6) are normalized as follows:

$$\begin{cases} Z = \dfrac{x}{x_{sh}} = \dfrac{\varepsilon \ \omega \ A}{c_0^2} \cdot x \\ V = \dfrac{u}{A} \\ \theta = \omega \ \tau = \omega \ (t - \dfrac{x}{c_0}) \\ \gamma = \dfrac{b \cdot \omega}{2 \cdot \varepsilon \ c_0 \cdot \rho \ \cdot A} \end{cases} \tag{1.7}$$

x_{sh} is the distance at which a shock wave appears; A is the amplitude of the propagating wave, and ω its angular frequency.

The dimensionless expression of equation (1.6) becomes:

$$\frac{\partial V}{\partial Z} - V\frac{\partial V}{\partial \tau} = \frac{\partial^2 V}{\partial \tau^2} \tag{1.8}$$

Neglecting the nonlinear term in equation (1.6), the linearized form of this equation with physical parameters is expressed as follows:

$$\frac{\partial u}{\partial x} = \frac{b}{2c_0^3\rho_o}\frac{\partial^2 u}{\partial t^2} \tag{1.9}$$

for which the solution is given in the form:

$$u = A \cdot e^{-\frac{b\cdot\omega^2}{2\cdot c_o^3\cdot\rho_o}\cdot x} \sin\ \omega\ \left(t - \frac{x}{c_o}\right) \tag{1.10}$$

which can be written as:

$$V = e^{-\alpha Z}\sin\theta \tag{1.11}$$

Using successive approximation method for analytical solution, we seek a solution in the form:

$$V = \mu^{(1)} + \mu^2 V^{(2)} + \ldots \tag{1.12}$$

Restricting ourselves to problems of the second approximation, we consider the following system of equation:

$$\begin{cases} \dfrac{\partial V^{(1)}}{\partial Z} - \gamma \dfrac{\partial^2 V^{(1)}}{\partial \theta} = 0 \\ \dfrac{\partial V^{(2)}}{\partial Z} - \gamma \dfrac{\partial^2 V^{(2)}}{\partial \theta} = \dfrac{1}{2} \dfrac{\partial^2 V^{(1)}}{\partial \theta} \end{cases} \tag{1.13}$$

The solution of the upper equation in (1.13) is already known as:

$$V^{(1)} = \; ?^{-\;Z} \sin\theta \tag{1.14}$$

We substitute this form into the lower equation in (1.13) and obtain:

$$\frac{\partial\, ^{r(2)}}{\partial\, ?} - \; \cdot \frac{\partial\, V^{(2)}}{\partial\,)^2} = \; \frac{1}{2} e^{-\;\gamma Z} \sin 2\theta \tag{1.15}$$

We further search for a solution in the form:

$$V^{(2)} = \; 3(Z) \sin\theta \tag{1.16}$$

Inserting (1.16) into (1.15) gives:

$$\frac{dB}{dZ} + \; 4\gamma\, ? = \frac{1}{2} e^{-\;\gamma\, \cdot} \tag{1.17}$$

Now, let's seek the solution of (1.17) in the form:

$$B = C_1 e^{-\gamma z} + C_2 e^{-\gamma z} \tag{1.18}$$

Substituting (1.18) into (1.17) we get:

$$C_2 = \frac{1}{4\gamma} \tag{1.19}$$

And (1.18) becomes:

$$B = C_1 e^{-\gamma z} + \frac{1}{4\gamma} e^{-\gamma z} \tag{1.20}$$

C_1 is determined by considering that the second harmonic is absent at the input to the system:

$$B\big|_{Z=0} = 0 \Rightarrow C_1 = -\frac{1}{4\gamma} \tag{1.21}$$

We end up with the following expression:

$$B = \frac{e^{-\gamma z} - e^{-\gamma z}}{4\gamma} \tag{22}$$

Figure 1-5 shows the curve which illustrates the path of the amplitude B of the second harmonic, generated by the first one as a function of the distance Z. The amplitude of the second harmonic increases initially according to a linear law, due to the nonlinear pumping of the energy from the wave of fundamental frequency, and then begins to fall

off, due to the predominating effect of dissipative processes [122]. In the context of the investigation in this thesis, the second harmonic generation is evidently negligible, at a distance corresponding to the size of a cell.

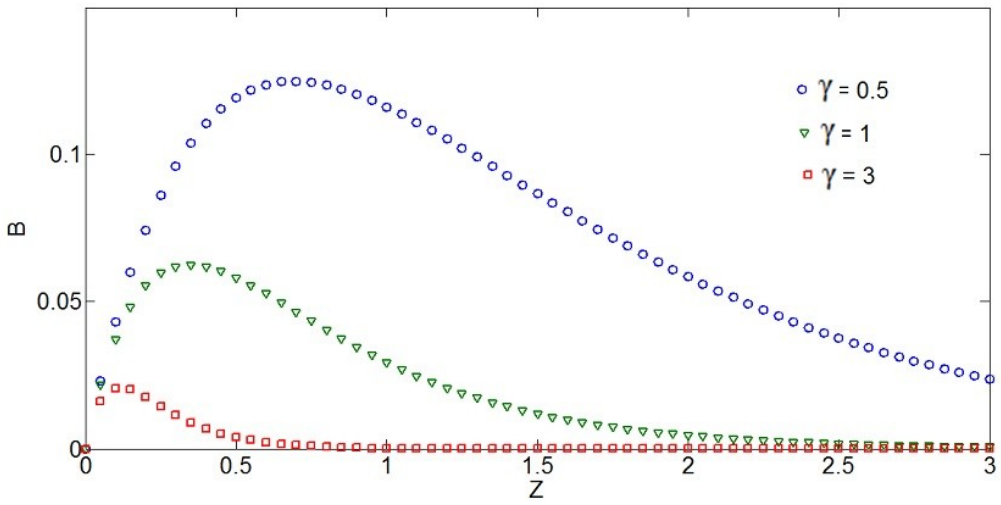

Figure 1-5 Amplitude of the second harmonic (B) generated by the first one for different values of γ - Evidence of nonlinear effect appearance at the distance Z.

Let us now investigate whether a shock wave will be generated or not within the region of interest in our experimental setting (distance corresponding to the size of a cell). A shock wave is generated when a high harmonic becomes maximum. From equation (1.22), this condition is mathematically expressed as follows:

$$\frac{dB}{dZ} =) \Rightarrow Z_{\max} = \frac{\text{'n } 2}{\gamma} \tag{1.23}$$

In physical parameters, the distance at which the second harmonic generated by the first one is maximum is therefore given by:

$$x_{\max} = \frac{\rho c_0^3 \ln 2}{b\omega} \tag{1.24}$$

Equation (1.24) is plotted in Figure 1-6 showing that at 600 kHz, shock wave occurs at a distance of 185 m; at 1.2 MHz, shock wave occurs at a distance of 45 m; thus, extrapolating from equation (1.24) shows that an excitation frequency of 200 MHz is required to generate a shock wave at a distance 1.5 mm, approximate distance from the surface of the transducer to the substrate surface on which cells adhere. Therefore, our chosen excitation frequency range is within a safe limit.

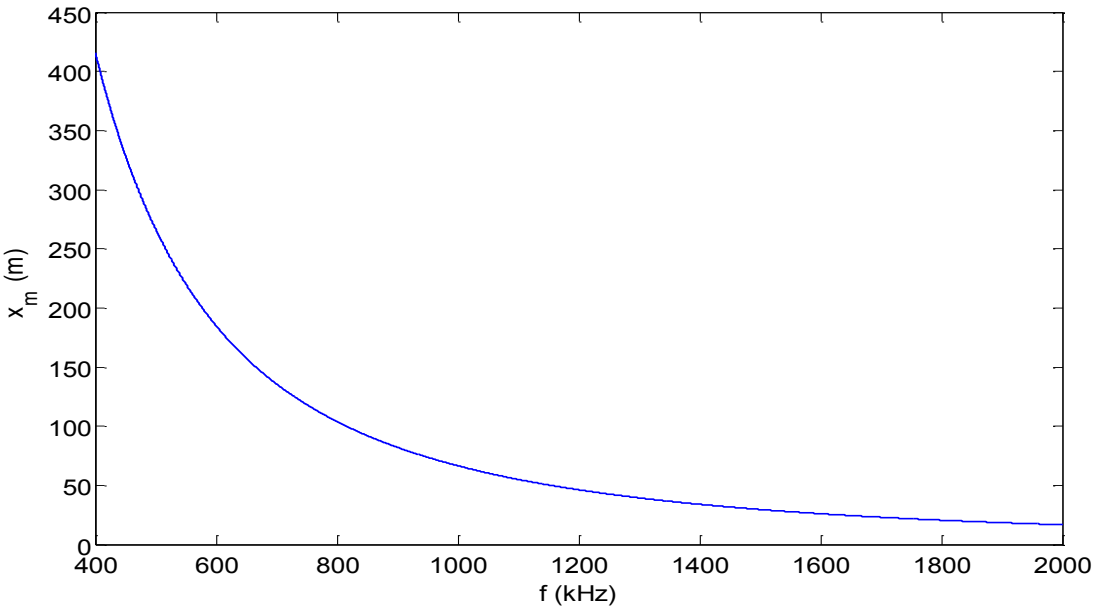

Figure 1-6 Frequency dependency of the amplitude of the second harmonic.

1.4.4 Cell culture substrate stiffness variation and measurement

The PDMS used in this work is a liquid bi-component silicone pre-polymer, Sylgard 184 manufactured by Dow Corning (Midland, MI). The substrate stiffness can be controlled by the base (pre-polymer) to hardener (curing agent) ratio, determining the cross-linker agent concentration in the PDMS solution. The solutions were mixed in sterile conditions and degassed, then poured into cell culture dishes to a depth of about 1 mm. Other key parameters for manipulating the mechanical property are temperature and curing time. As these parameters are closely linked, we choose to cure the PDMS substrates at a constant temperature of 75^{o}C for 2 hours.

For the measurement of the stiffness of the fabricated substrates, we used a Digital Instruments Nanoscope III Multimode to indent the sample with an AFM tip, a three-sided pyramid blunt indenter mounted on a stiff steel cantilever. The nanoindentation test consisted of applying a load (F) on the indenter and subsequently removing the load. According to the procedure described by Cappella et al. [123], the AFM piezoelement was ramped up until the contact between the sample and the tip was observed. From this point, a further piezo displacement z provoked the cantilever to bend of a quantity δ thus applying a load:

$$F = \cdot\delta \tag{1.25}$$

where k is the normal elastic constant of the cantilever. The nanoindentation then took place while the cantilever bends and resulted in a penetration depth given by:

$$p = z - \delta \tag{1.26}$$

The piezo displacement z and the cantilever deflection δ were then recorded in order to obtain a common F vs. p force curve from equations (1.25) and (1.26), from which the stiffness of the substrate was estimated. The tip-sample system showing how the actual distance is obtained is illustrated in Figure 1-7, where p is the actual tip-sample distance, Z is the distance between the sample and the cantilever rest position. These two distances differ because of the cantilever deflection δ_c and because of the sample deformation δ_s.

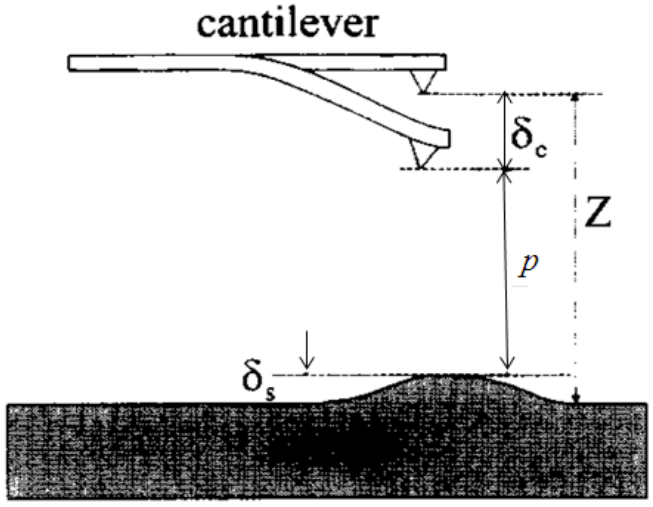

Figure 1-7 The tip-sample system. Spectrophotometry techniques

Spectrophotometry technique is considered a comprehensive and sensitive method for detection of molecular changes in samples. This technique is used in this thesis to show the difference between fresh and conditioned culture media after cell cultivation. The cell culture media used typically contain D-Glucose (4.5g/L), sodium bicarbonate (1.5g/L), sodium pyruvate (1mM), HEPES buffering agent (10mM), and L-glutamine (300mg/L).

When a monochromatic light passes through a sample, there is a quantitative relationship (Beer's Law) between the solute concentration and the intensity of the transmitted light, that is,

$$I = {}_{0} * 10^{-cl} \tag{1.27}$$

where I_0 is the intensity of transmitted light using the pure solvent, I is the intensity of transmitted light when the colored compound is used, c is concentration of the colored compound, l is the distance the light passes through the solution, and k is a constant. The path length was set constant and Beer's Law is written as:

$$\frac{I}{I_0} = 10^{-c} = \tag{1.28}$$

where k is a new constant and T is the transmittance of the solution. In the UV range, NAC as well as the absorbance of both the cell culture media and its nucleic acid were considered. Analysis of 1 µl sample was achieved, without the need for cuvettes or capillaries. Figure 1-6 summarizes the steps for measuring one sample.

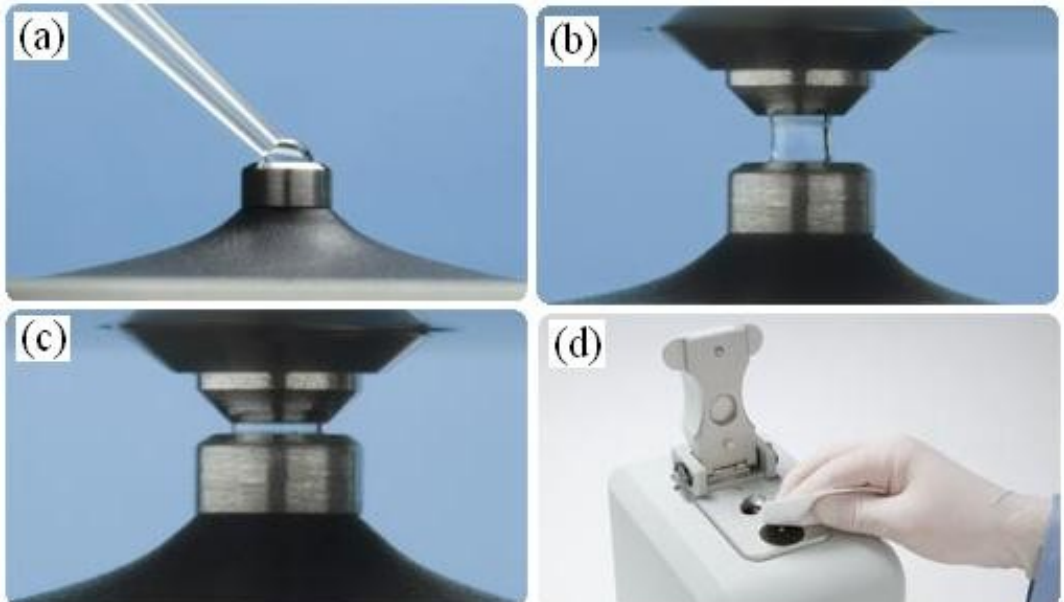

In the near (14000 to 4000 cm^{-1}) and middle (4000 to 400 cm^{-1}) IR ranges, the optical throughput (percent of energy reaching the detector) was used to quantitatively differentiate media from different incubation times and cell types. The Perkin Elmer Spectrum BX FT-IR spectrometer was used for sample collection and testing. The Spectrum BX can operate in ratio, single-beam, or interferogram mode. In order to analyze the collected media, radiant beams are divided, an optical path difference between the beams is generated, and the beams are recombined in order to produce repetitive interference signals. These signals contain Infra-Red spectral information generated after passing through the samples and are measured as a function of the optical path difference by means of a detector.

The liquid sample was sandwiched between two plates of a high purity salt of calcium fluoride. These plates are transparent to the infrared light and do not introduce any lines into the spectra. The path length (the Teflon foil spacer's thickness) was 20 μm. Useful wave number range of this window material is 50000 to 1000 cm^{-1}. The transmission spectra were recorded in the wave number ranges 4000 to 1000 cm^{-1} and 7000-4000 cm^{-1} with a resolution of 4 cm^{-1}. The digitization interval was 2 cm^{-1}. The beam splitter used was made of KBr. The source was a MIR (Multiple Internal Reflectance) laser and the detector a DGTS (Deuterated Triglycine Sulfate) photodetector. The experimental arrangement of FTIR spectroscopy is presented in Figures 1.9.

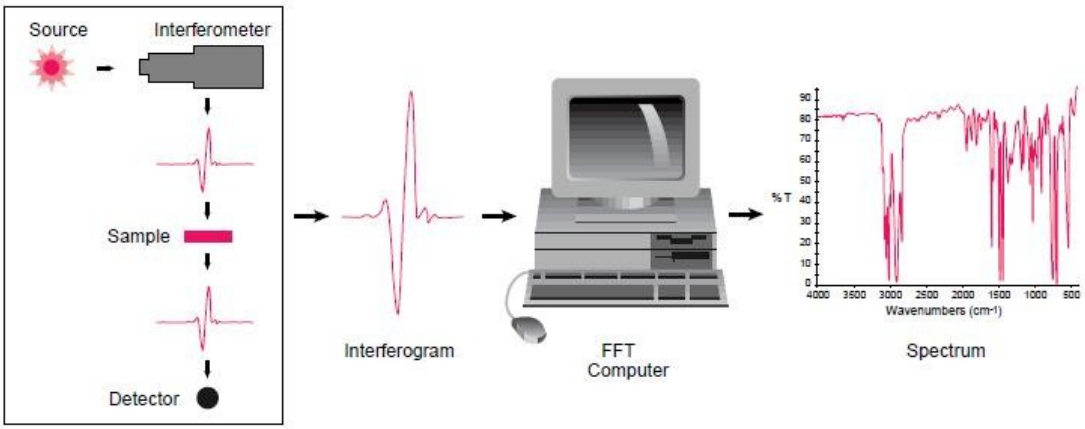

Figure 1-9 Experimental arrangement of FTIR spectroscopy.

1.4.5 Basic cell culture and experimental process flow

The cells were thawed following standard recommendations as follow:

- The vial was removed from liquid nitrogen and transferred to 37^{o}C water bath.
- While holding the tip of the vial, it was gently agitated, being careful not to allow water to penetrate the cap.
- When completely thawed, the content of the vial was transferred to 15 mL test tube.
- 10 mL of warm complete media was slowly added and the tube was spun at 1200g for 5 minutes.

- The media was decanted and the pellet resuspended in a volume of complete media appropriate for flask.
- The flask was incubated at 37^{o}C and 5% CO_2.
- Cells were checked the following day for an estimate of viability.

The basic proliferation assessment by cell counting and the FTIR analysis of the culture media were performed following the process flow shown in Figure 1-10 and described below:

(1) The cells preparation was performed in a biosafety cabinet.

(2) The cells were transferred to an incubator and kept at 37^{o}C and 5% CO_2.

(3a) The culture media are extracted and transferred to 15 mL tubes.

(4a) A gradient separation is performed in order to isolate dead cells.

(5a) The sample to be tested is then collected and,

(6a) FTIR measurements are performed.

(3b) The cells are washed with PBS, then trypsinized in order to detach them.

(4b) The solution is transferred to 15 mL tubes, then spun to separate the pellet.

(5b) Cells are resuspended in 10 mL fresh medium.

(6b) Cell counting is performed using a standard haemocytometer under microscope.

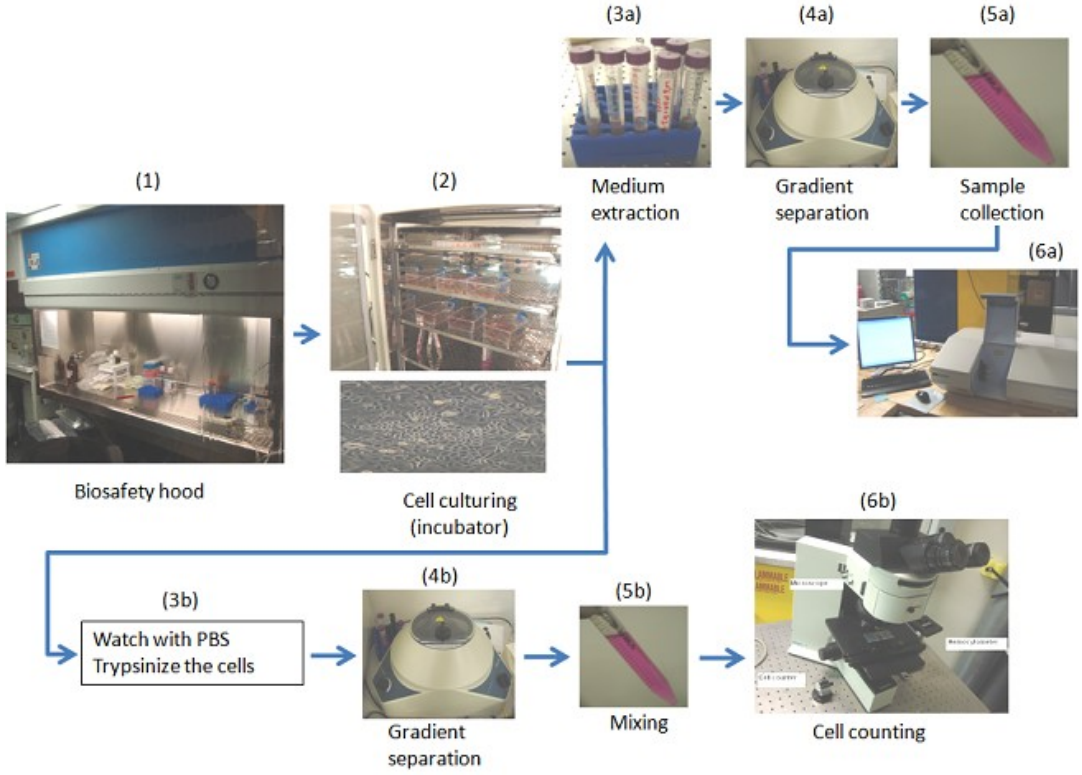

Figure 1-10 Cell cultivation, cell counting and media analysis

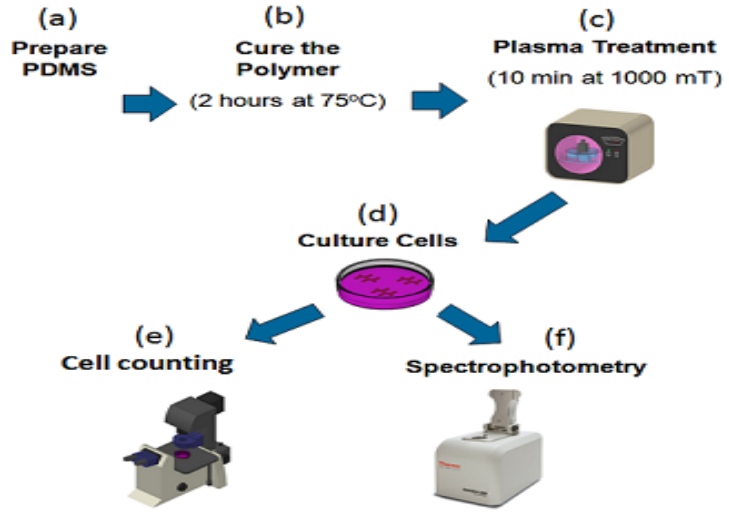

Figure 1-11 Cell cultivation on PDMS substrates.

Figure 1-11 illustrates the flow process of experimentation on cells cultured on PDMS substrates. The steps are as follows:

(a) The PDMS base and curer ratio is prepared depending on the substrate stiffness required, then mixed and poured in a culture dish.

(b) The mixture is cured at 75^{o}C for 2 hours on a hot plate.

(c) The substrate is exposed to air plasma for 10 minutes at 1000 mT.

(d) The treated substrate is covered, exposed to a low power UV irradiation for further sterilization, then used for plating cells.

(e) & (f) Cell counting as well as spectrophotometry of the extracted culture media are then performed for interpretation.

All of these methods will help coherently making up the overall thesis contribution described below.

1.5 Thesis contributions

The main contribution of this thesis applies to interfaces of engineering with micro-biomedicine, addresses the reduction of both experimental time and cost, and is threefold. First, the thesis suggests, as illustrated in Figure 1-12, the proof of concept of a novel

approach of cancer cell proliferation assessment that is non-invasive, allows continuous cell growth monitoring of the same cell population by displaying the absorbance level, enables monitoring under different other cell conditioning methods (US, CNTs, substrate stiffness variation, etc.), and it is applicable only to the cell culture media. Although FTIR mainly deals with nonaqueous samples due to strong absorption bands of water [124-126], the technique is shown (in this thesis) to allow quantitative estimation of different samples, or the same sample at different treatment levels, in terms of total energy reaching the detector.

Second, with respect to fundamental research, the thesis proposes the first investigation that categorizes the gene targets of SWCNTs in primary normal lung cells using gene expression through microarray analysis. The comprehensive identification and profiling of gene expression affected by these nanoparticles is established and validated, making this application a systematic approach toward gene marker identification. Moreover, the proposed low power US exposure of cancer cells helps understanding the mechanisms of invasion and proliferation more clearly and thus, provide information relevant to cancer therapy.

Last but not the least in cell conditioning, this thesis reveals that the physicality of the ECM substrate govern cell behavior regardless of hormones, cytokines, or other soluble regulatory factors. Indeed, local alterations in ECM substrate influencing cell adhesion appear to drive regional changes in cell growth and neuroblastoma transdifferentiation. These applications of engineering techniques to biology offer a beneficial platform for innovative biomedical applications and the results are useful in the discovery of new

materials and technologies which are potential therapeutic agents for chronic and fatal diseases.

Figure 1-12 Experimental arrangement and typical result of a real time continuous assessment of cell growth in the middle infrared range.

Further, moving from single cells to groups of organized cells, the thesis proposes an inverse problem formulation for modal parameters extraction of a 4 DOF mimicking early chick embryo model. It is demonstrated that the exact modal parameters of the chick embryo model can be obtained using both the Mode Indicator Functions (MIF) and a least squares approach using the Prony method, even when the mechanical excitation cannot be controlled. These estimators are presented as a promising modal indicator and parameter estimation technique, contributing to limit the cost of experiments at such a

small scale as in the investigation of embryo development. This is important for the understanding of the dynamics of morphogenetic processes, the biomechanics of tissues, the design of implantable medical devices and the biomaterials used in their fabrication. This approach is being extrapolated to the understanding of biological samples behaviour at cellular level, using the frequency resonance hypothesis.

1.6 Thesis organization in the manuscript-based format

This thesis is organized in eight chapters. In the present chapter, an introduction about cells conditioning with nanoparticles, a US field, and ECM manipulation, as well as spectrophotometry in cellular biology are briefly presented in order to avoid repetition in subsequent chapters (published articles from this thesis). The similarities between cellular biology and developmental biology, from a mechanical engineering prospect, are also presented. This is followed by the motivation, the scope and objective, the methods used, and the contribution of this thesis. Chapters 2 to 5 are duplicated from four published journal articles. Chapters 6 and 7 are duplicated from two submitted journal articles. These chapters are organized in a cohesive manner to address the specific objectives of the thesis, defined in Section 1.3, and formatted according to the "Thesis Preparation and Thesis Examination Regulations (version 2011)" of the School of Graduate Studies at Concordia University. In the duplicated articles, sections, figures, tables and equations are numbered according to the thesis preparation regulations. A single comprehensive reference list rather than individual articles reference list is adopted in the References section. In chapter 8, a general conclusion of the thesis is given, together with a suggested

conceptual design of a micro-device capable of handling the techniques presented in this work.

Chapter 2 is based on the following article published in Nanomedicine [127]

Alazzam A, Mfoumou E, Stiharu I, Kassab A, et al. Identification of deregulated genes by single wall carbon nanotubes in human normal bronchial epithelial cells. Nanomedicine 2010 Aug; 6(4):563-9.

To identify genes affected by single-walled carbon nanotubes (SWCNTs) in human normal lung cells, we compared the gene expression profiles of untreated human normal bronchial epithelial (HNBE) cells to profiles of HNBE cells treated with SWCNTs. A complementary DNA microarray analysis consisting of 54,675 human genes revealed marked changes in the expression of 14,294 genes, with 7,029 genes being up regulated and 7,265 being down regulated. This comprehensive list of genes included those associated with cell cycle, apoptosis, cell survival, cell adhesion and motility, signal transduction, and transcription regulation. Additional analysis of 19 genes using reverse transcription-polymerase chain reaction (RT-PCR) confirmed the microarray analysis. More specifically, our study demonstrates to our knowledge for the first time, evidence that 9 of the 19 genes (most of which encode cell apoptotic, signal transduction, and transcription regulator products) are up regulated in the SWCNTs-treated HNBE cells as compared with untreated cells, whereas the remaining 10 of the 19 (involved in cell adhesion and motility, cell proliferation, and cell survival) are down regulated in SWCNTs-treated HNBE cells in comparison with untreated controls. These findings

provide a large body of information regarding gene expression profiles associated with SWCNTs exposure in human lung bronchial epithelial cells, and also represent a source to investigate the mechanism of the effect of SWCNTs in human normal lung cells. From the clinical editor: In this study, the gene expression profile of human normal bronchial epithelial cells was compared with single-wall carbon nanotubes-treated cells. A cDNA microarray analysis consisting of 54,675 human genes revealed significant changes in the expression of 14,294 genes, with 7,029 genes being up-regulated and 7,265 being down-regulated. This serves as a first step in clarification of mechanisms of action and to investigate toxicity in this model.

Chapter 3 is based on the following article in press in Medical Hypotheses [128].

Etienne Mfoumou, Narayanswami Sivakumar, Ala-Eddin Al Moustafa, and Ion Stiharu. A new concept to measure cell proliferation using Fourier transform infrared spectroscopy. Medical Hypotheses 79:171-173, 2012.

In our laboratory, we recently developed a new technique to study cell proliferation that is based on infrared spectro-photometry and the density of cell culture medium. The fluid exchange between intra and extra cellular environments is the key to our method. Using this technique, we found that cell proliferation assessment may be performed much faster than presently existing methods, using two separate pieces of equipment (a cell culture incubator and an interferometer). We confirmed the viability of our method using five different cell lines, breast cancer cells (BT20), mouse normal embryonic fibroblast (NEF) as well as those expressing E6/E7 onco-proteins of human papillomavirus (HPV) type 16, and a human cervical cancer cell line (HeLa). Based on our findings, we propose the design of a mini-incubator allowing cell culture as well as infrared spectra collection of

the culture medium, as an accessory to the FTIR work bench, which would become a promising arrangement for continuous cell proliferation monitoring. Moreover, the use of the collected culture medium will be highly efficient in terms of reducing both experimental time and cost.

Chapter 4 is based on the following article in press in Clinical Cancer Investigation [129]

Mfoumou E, Stiharu I, Narayanswamy S, Al Moustafa AE. Low Power Ultrasound Inhibits Cell Proliferation and Invasion of Human Cancer Cells in Vitro. Clinical Cancer Investigation Journal, 2012, 1(2):51-6.

The role of low power ultrasound waves on the key genes associated with cell proliferation and invasion was investigated in vitro on breast (BT20 and BT20-E6/E7) and cervical (HeLa) cancer cells. The cells were plated and incubated both with and without ultrasound exposure, and proliferation as well as invasion assays were performed to investigate the outcome of ultrasound irradiation. Western Blot was then performed to study the expression pattern of some selected genes associated with the effect of ultrasound on these cancer cells. Fluorescence Activated Cell Sorting (FACS) was finally performed to examine the effect of ultrasound on cell cycle progression. We found that low power ultrasound inhibits cell proliferation and provoke G0-G1 cell cycle arrest and reduction of S as well as increasing G2-M phase of HeLa cells in comparison with the wild type cells. This is accompanied by a down-regulation of Cdk-6 (cyclin dependent kinase) which is a major control switch for the cell cycle. Moreover, low power ultrasound inhibits cell invasion via down-regulations of Id-1, Caveolin and EGF-R which are widely considered main regulators of cell invasion and metastasis of human carcinomas cells. Our results suggest that low power ultrasound applied to human breast

and cervical cancer cells could be an effective method to reduce cell proliferation and invasion of these cancers.

Chapter 5 is based on the following article in press in Spectroscopy Letters [130].

Etienne Mfoumou, Sivakumar Narayanswamy, Ion Stiharu, and Ala-Eddin. Al Moustafa. On the feasibility of an in vitro noninvasive absorbance-based cell proliferation analysis technique, using cell culture media. In press. Spectroscopy Letters, 2012. ID: 686143 DOI:10.1080/00387010.2012.686143.

The preliminary results of a study on the applicability of using spectrophotometry of the culture medium toward understanding of cells response to different environments is reported. The cells are cultivated on polydymethylsiloxane (PDMS) substrates, and physico-chemically manipulated by varying the substrate stiffness and the dose of surface plasma treatment. By growing cervical cancer (HeLa) cells on PDMS with varying stiffness and plasma treatment levels, we tested the hypothesis that the influence of substrate stiffness and treatment can be detected through the spectrophotometry of a micro volume of cell culture medium. The results imply an opportunity of using the spectrophotometry of culture media with an integrated minimal sample retention system as a practical and non-invasive alternative to traditional bioassays requiring cells detachment.

Chapter 6 is based on the following article submitted to Cells and Materials [131].

Etienne Mfoumou, Ion Stiharu, Sivakumar Narayanswamy, and Ala-Eddin. Al Moustafa. Elasticity-triggered biological responses of SH-SY5Y neuroblastoma cells in vitro. Under review, Biomedical Materials and Engineering, 2012.

The cellular adhesion and polarization have direct implications in the tumoral-metastatic cells development or in tissue engineering mechanisms. The properties of cells surrounding environment play a role in this matter and this work aims at investigating the influence of substrate mechanical properties on neuroblastoma transdifferentiation, adhesion and polarization. The method is based on modifying bulk rigidity and surface energy of PDMS substrate. We obtained a wide range of substrate rigidities and turn them to hydrophilic with an air plasma treatment. An immunocytochemistry test is performed and a correlation between bulk rigidity, cell adhesion, cell polarization and cell growth is shown.

Chapter 7 is based on the following article submitted to Mechanics of Research Communications [132].

Etienne Mfoumou, Ion Stiharu, Jean Atangana Ateba, Sivakumar Narayanswamy, and Ala-Eddin. Al Moustafa. Mechanical vibration analysis and its application to modal parameters estimation in early avian embryo. Under review, Mechanics of Research Communications, 2012.

Mechanical forces play an important role during early embryo development. Although physical and mechanical properties of organs are available in the literature for different stages of growing chick embryos, the modal parameters of each organ remain largely unknown. A simplified model of 4 degrees-of-freedom (DOF) mass-spring-damper (MKC) system made of the body (limb), the liver, the heart and the brain is considered in

this paper. A data set of material parameters corresponding to a stage 14 chicken embryo development is obtained from the literature. An eigenvalue solution approach using frequency response function matrices is applied to study the mechanical vibrations of the system. We demonstrate that the exact modal parameters of the chick embryo model can be obtained using both the Mode Indicator Functions (MIF) and a least squares approach using the Prony method, even when the mechanical excitation cannot be controlled. These estimators are presented as a promising modal indicator and parameter estimation technique, contributing to limit the cost of experiments at such a small scale as in the investigation of embryo development. Therefore, our study can help illuminating the mechanical vibration analysis of incubated eggs and its relation to embryogenesis. This is important for the understanding of the dynamics of morphogenetic processes, the biomechanics of tissues, the design of implantable medical devices and the biomaterials used in their fabrication.

Chapter 8 presents the general conclusion of the thesis and suggests future works.

CHAPTER 2. The effect of carbon nanotubes on living cells: application to human normal bronchial epithelial (HNBE) cells

This chapter presents a large body of information regarding gene expression profiles associated with SWCNTs exposure in human lung bronchial epithelial cells. This work is based on an article published in Nanomedicine [127], and covers the objective (i) of the "Thesis objective and scope" in section 1.3.

2.1 Introduction

Carbon nanotubes (CNTs) offer exciting opportunities for science and applications. In recent years CNTs research has become established as a highly interdisciplinary field to exploit their outstanding features [133]. Conceptually, single-walled carbon nanotubes (SWCNTs) are considered as small strips of graphene sheets that have been rolled up to form perfect seamless single walled nanocylinders. CNTs have the added advantage of being potential nanofluidic devices for controlled drug delivery [133,134].

Great interest has been generated in fullerenes in general, but especially in CNTs and carbon nanohorns as biologically compatible materials and drug carriers mainly because of their distinct architecture, hollow interior, and cage like structures. However, the small size, large surface area, and high reactivity of these materials are the main factors for potential toxicity [135]. Moreover, CNTs will have widespread applications in many technological fields; thus, worker-consumer exposure is likely to occur, posing emerging

health concerns [135,136]. Initial toxicological studies demonstrated that pulmonary deposition of SWCNTs or multiwall carbon nanotubes causes acute pulmonary inflammation as well as chronic responses such as fibrosis [137,143].

These studies suggest that CNTs may induce toxicity in normal bronchial epithelial cells. However, how CNTs provoke susceptibility to the toxicity and pulmonary inflammation is not clear. Thus, genome-wide monitoring of gene expression is important to understand the extent of the effects of CNTs.

To this end we have carried out a complementary DNA (cDNA) array analysis using Affymetrix probe sets complementary to approximately 54,675 human genes, to monitor the levels of expression within human normal bronchial epithelial (HNBE) cells treated with SWCNTs and within unexposed cells. We identified a comprehensive list of genes that are differentially expressed between cells treated with SWCNTs and in untreated control cells; the majority of these genes have, to our knowledge, been identified for the first time as targets of the effects of SWCNTs. We believe that our data reveal the complex nature of the genetic changes after the accumulation of SWCNTs in human normal lung cells.

2.2 Methods

2.2.1 HNBE cells and SWCNTs preparation

Primary HNBE cells were obtained from Lonza Group (Shawinigan, Quebec, Canada). Cells were seeded on plastic dishes and fed every 48 hours with keratinocyte Serum-Free Medium supplemented with 5 mg/100 mL of bovine pituitary extract (Invitrogen Canada

Inc., Burlington, Ontario, Canada). At 80% to 90% confluence the cells were trypsinized with 0.05% Trypsin in 0.53 mM ethylenediamine tetra acetic acid and reseeded at a ratio of 1:3. These cells had doubling times in approximately 4 days, being shorter in early passage than late passages before senescence after eight passages. The purified SWCNTs, which are composed of more than 90% carbon, were obtained from Sigma-Aldrich (Oakville, Ontario, Canada). SWCNTs were dissolved and diluted to a concentration of 1 mg/mL stock in 1× phosphate-buffered saline. The particles were vortexed for 1 minute and then indirectly sonicated (Hielscher Ultrasonic, Ringwood, New Jersey) for 10 minutes at 4°C immediately before preparing treatment dilutions into serum-free and growth factor–free medium. The dilutions were again vortexed before being added to the cells at 60% to 70% confluence; the cells were incubated with a final concentration of 0.1 mg/mL SWCNTs. This concentration was selected based on the studies of Simon-Deckers et al. [144] and Tabet et al. [145] on the effect of SWCNTs in vitro.

2.2.2 Cell morphology, growth, and viability analyses

Cells (1 × 106 per milliliter) were plated in 100-mm dishes in their regular medium (untreated cells) or containing 0.1 mg/mL of SWCNTs for 2 days. Cell morphology analysis was subsequently performed using an inverted phase-contrast microscope. For cell growth and viability assay the cells were collected by trypsinization, washed, and counted after 2 days using trypan blue exclusion and a haemocytometer. These analyses were repeated three times.

2.2.3 RNA isolation and microarray analysis

Total RNA was extracted with TRIZOL (Invitrogen Canada Inc.) according to the manufacturer's instructions. Biotinylated probes for microarray analysis were prepared using 10 μg of total RNA as described below. The total RNA was mixed with 100 pmol of T7- (T) 24 primer (Genosys, San Diego, California) and denatured for 10 minutes at 70°C, then chilled on ice. First-strand cDNA synthesis was performed using Superscript II reverse transcriptase (Life Technologies, Toronto, Ontario, Canada), and second-strand synthesis was performed using DNA polymerase I, Escherichia coli DNA ligase, and RNase H (Invitrogen Canada Inc.). The biotinylated probe was prepared from the entire cDNA reaction using the ENZO Bioarray High Yield RNA Transcript Labeling Kit (ENZO Diagnostics, Toronto, Ontario, Canada). Incubating the purified probe in 1× fragmentation buffer for 35 minutes at 95°C reduced the average probe length. Hybridization was performed at 45°C for 20 hours using 15 μg of biotinylated probe. Following hybridization, the non-specifically bound probe was removed by 10 low-tringency washes and four high-stringency washes performed using a GeneChip Fluidics Station 400 (Affymetrix). Specifically bound probe was detected by incubating the arrays with Streptavidin Phycoerythrin (SAPE) (Molecular Probes, Eugene, Oregon) and scanning the chips using a GeneArray Scanner (Hewlett-Packard, San Diego, California). The scanned images were analyzed using the GeneChip Analysis Suite 3.3 (Affymetrix), and the statistical analysis of our microarray data was performed using FlexArray software (http://www.affymetrix.com/index.affx).

2.2.4 Reverse transcription–polymerase chain reaction (RT-PCR)

RT-PCR amplification was performed using primer sets for Rho GTPase 26, microtubule 2, GTP-binding protein 2, protein phosphatase 1, interleukin receptor 1, inhibin beta E, growth differentiation factor 15, forkhead a2, activating transcription factor 3, serpin peptidase inhibitor 4, chemokine 11, interferon 1, kinesins (14, 15, and 20A), leupaxin, cyclin B1, repetin, hyaluronan-mediated motility receptor, and glyceraldehyde 3 phosphate dehydrogenase (GAPDH) genes (Table 2-1).

Gene name	Primers
Rho GTPase-activating protein 26	5′-GGT CTG TTG CAG GGT TTG TT-3′
	5′-CTT CTG GCC TGT CAA AAA GC-3′
Microtubule 2	5′-AAA GCT GAT GAG GGC AAG AA-3′
	5′-GGC CCC TGA ATA AAT TCC AT-3′
GTP-binding protein 2	5′-TTA CAG CGA CTC ACG GAC AG-3′
	5′-TCT TGC TGA CCA CGA TGA AG-3′
Protein phosphatase 1	5′-GTG TAT TGG CCA GGA GAG GA-3′
	5′-GGC CTT CAA GAA AGC ACT TG-3′
Interleukin receptor 1	5′-AAG GAG TTT GCC TAC GAG CA-3′
	5′-TTT CTG GGA ATT TTG CTT GG-3′
Inhibin beta E	5′-TTG CTG CCT CTT TCC ATT CT-3′
	5′-CAT CCG TCT TGA CCA CAT TG-3′
Growth differentiation factor 15	5′-GAG GTG CAA GTG ACC ATG TG-3′
	5′-AAT GAG CAC CAT GGG ATT GT-3′
Activating transcription factor 3	5′-TCG GAG AAG CTG GAA AGT GT-3′
	5′-TCT GGA GTC CTC CCA TTC TG-3′
Forkhead a2	5′-ACC ACT ACG CCT TCA ACC AC-3′
	5′-GGG GTA GTG CAT CAC CTG TT-3′
Serpin peptidase inhibitor 4	5′-CCA CAG AAA AAG CTG CAA CA-3′
	5′-GTT TGA CTT TCC ACC CAG GA-3′
Chemokine 11	5′-GCT TCC CCA TGT TCA AAA GA-3′
	5′-TAA GCC TTG CTT GCT TCG AT-3′
Interferon 1	5′-GAG GAA CAT GAG GTG GCT GT-3′
	5′-ATG AGG ATG CCC AGA ATC AG-3′
Kinesin family member 14	5′-CCA ATG CTA TCA GCA GCA AA-3′
	5′-TGT AAT GTC GGG TTC CCA TT-3′
Kinesin family member 15	5′-TCT TTG CAA AAA GCG AAC CT-3′
	5′-ACT GGT CGG GAA TGA AGT TG-3′
Kinesin family member 20A	5′-CTT CCG TGA CAG CAA GTT GA-3′
	5′-TCC TTG ATG AAC GAG TGC AG-3′
Leupaxin	5′-CTG CTC CCA TCC TGG ATA AA-3′
	5′-AGT CCC CAC AAA CAA AGC AC-3′
Cyclin B1	5′-GGC CAA AAT GCC TAT GAA GA-3′
	5′-AGA TGT TTC CAT TGG GCT TG-3′
Repetin	5′-AGC CAA CAT CAC CAA CAC AA-3′
	5′-CCA CAT GGA CCT TCC TGA CT-3′
Hyaluronan-mediated motility receptor	5′-TGG AAG CAA GGC TAA ATG CT-3′
	5′-ACC TGC AGC TTC ATC TCC AT-3′
GAPDH	5′-TGC ACC ACC AAC TGCTTAGC-3′
	5′-GGCATGGACTGTGGTCATGAG-3′

Table 2-1 Primer sets used for reverse transcription-polymerase chain reaction amplification

GAPDH was used to control the amounts of cDNA generated from each sample. Synthesis of the first-strand cDNA was carried out using a cDNA kit for RT-PCR (MBI Fermentas, Toronto, Ontario, Canada). One fifth of the RT product was amplified for 30 cycles (1 minute at 95°C, 1 minute at 58°C, and 1 minute at 72°C) followed by an extension of 7 minutes at 72°C. RT-PCR amplification products were analyzed on a 1% agarose gel stained with ethidium bromide; the RT-PCR analysis was repeated three times for each gene.

2.3 Results

Identification of differential gene expression between HNBE cells treated with SWCNTs and HNBE wild-type (control) cells is the basis for a comprehensive understanding of the effect of SWCNTs in human lung cells, as these differences are likely to represent the coordinated alteration of critical pathways involved in the regulation of cell proliferation, apoptosis, and cell survival. We reasoned that using HNBE cells would be the best way to study the effect of SWCNTs in human normal lung cells. Therefore, we treated HNBE cells with 0.1 mg/mL of SWCNTs for 48 hours, as described in the Methods section. This concentration was determined following multiple trials, and was chosen in order to see the long term effect of SWCNTs in HNBE cells. In the absence of treatment, HNBE cells displayed an epithelial phenotype, and formed a monolayer of well-organized cells. In contrast, and as indicated in Figure 2-1, A, treatment with SWCNTs led to a phenotypic conversion from epithelial to fibroblast-like phenotype. Cells became more elongated and larger in appearance, and showed a decrease in cell-cell contact in comparison with untreated cells; this was accompanied by an inhibition of cell proliferation and cell death

(Figure 2-1, B), showing SWCNTs presence within their cytoplasm. HNBE-treated cells (T) were compared with their control untreated-cells (U). The cell proliferation and viability were assessed by morphology analysis using an inverted phase-contracst microscope and trypan blue exclusion assays as described in the Methods section. Data represent the mean ± SD of three independent experiments.

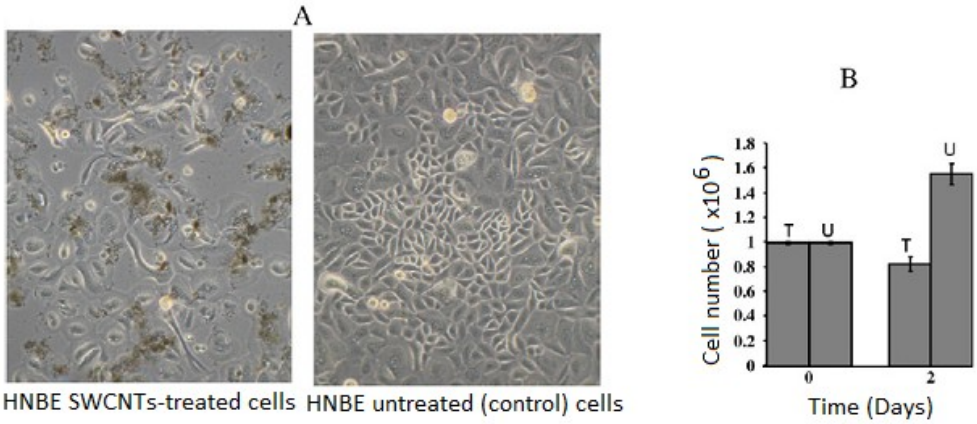

Figure 2-1 Effect of single-walled carbon nanotubes (SWCNTs) on cell morphology, cell proliferation, and viability in human normal bronchial epithelial (HNBE) cells after 2 days of treatment with 0.1 mg/mL of SWCNTs.

We used the cDNA array technique to identify genes that are differentially expressed in HNBE cells treated with SWCNTs in comparison with HNBE wild-type (untreated) cells. Figure 2-2 shows a scatter plot of the differential expression of the 54,675 genes in HNBE cells treated and untreated with SWCNTs. Overall we identified 14,294 genes out of 54,675, which are regulated differently between matched treated and untreated cells.

The full list of those commonly deregulated genes is available as supplementary information on our website (http://concave.concordia.ca). A total of 7,029 genes, with intensity ratios between 1.0 and 8.0, were up regulated, whereas 7,265 genes were down regulated with ratios between –8.0 and –1.0. Thus, 12.8% of the 54,675 genes were over

expressed and 13.2% were under expressed in the SWCNTs-treated cells. It is therefore notable that the expression levels of 74% of all genes studied in this experiment did not differ between SWCNTs-treated and untreated cells.

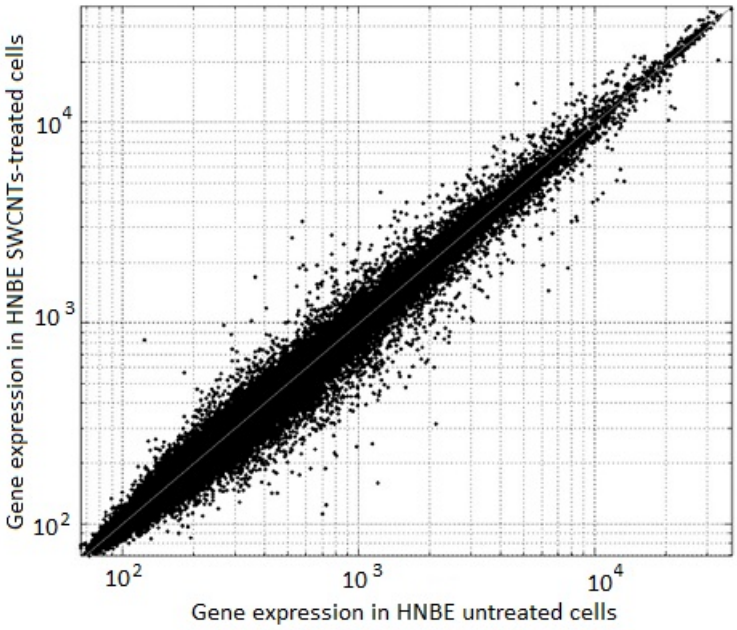

Figure 2-2 Representative scatter plot complementary DNA (cDNA) microarray analysis of HNBE cells treated and untreated with SWCNTs. HNBE-SWCNTs treated cells, 0.1 mg/mL for 48 hours (y-axis) and untreated cells (x-axis) of each sample were labeled and hybridized to the cDNA microarray.

The altered genes included those associated with cell cycle, apoptosis, cell survival, cell adhesion, signal transduction, and transcription regulation (Tables 2-2 and 2-3). In general, most of the genes that are over expressed in SWCNTs-treated cells encode cell apoptotic, signal transduction, and transcription regulator products, whereas those genes that are under expressed are involved in cell adhesion and motility, cell proliferation, and cell survival (Tables 2-2 and 2-3).

Table 2-3 Representative list of underexpressed genes in HNBE cells treated with SWCNTs when compared with untreated cells.*

Average ratio of two experiments	GenBank accession no.	Gene name	Function
1.112	AA971429	Caspase 8	Cell apoptosis
1.914	NM014330	Protein phosphatase 1	Cell apoptosis
2.877	NM001674	Activating transcription factor 3	Cell apoptosis
1.121	N36774	Tumor necrosis factor receptor superfamily, member 1A	Cell apoptosis
2.760	AJ277151	Tumor necrosis factor receptor 4	Cell apoptosis
1.658	BC006196	Tumor necrosis factor receptor 9	Cell apoptosis
2.179	NM002546	Tumor necrosis factor receptor 11b	Cell apoptosis
1.816	AF246998	Tumor necrosis factor receptor 19	Cell apoptosis
2.453	NM001252	Tumor necrosis factor 7	Cell apoptosis
1.781	AI936516	Tumor necrosis factor 8	Cell apoptosis
1.664	AF053712	Tumor necrosis factor11	Cell apoptosis
3.079	BC033638	Caspase 1	Cell apoptosis
2.932	BE467978	Caspase 4	Cell apoptosis
2.084	AL833692	Caspase 11	Cell apoptosis
3.639	BF433388	B-cell CLL/lymphoma 2 (*BCL2*)	Cell apoptosis
2.404	AI498359	BCL2-like 2	Cell apoptosis
1.391	NM019096	GTP-binding protein 2	Cell signaling
2.628	NM020525	Interleukin 22	Cell signaling
2.376	NM003856	Interleukin 1 receptor-like 1	Cell signaling
2.561	AF003934	Growth differentiation factor 15	Cell signaling
2.537	AL110232	Transcription factor EC	Transcription regulator
2.075	AB028021	Forkhead box A2	Transcription regulator
2.701	BC005161	Inhibin, beta E	Cell growth
1.454	BF342661	Microtubule-associated protein 2	Cell structure

Table 2-2 Representative list of overexpressed genes in HNBE cells treated with SWCNTs when compared with untreated cells.*

Average ratio of two experiments	GenBank accession no.	Gene name	Function
−1.463	AA481656	Protocadherin 1	Adhesion
−1.097	NM018937	Protocadherin beta 3	Adhesion
−3.929	BC000019	Cadherin 6 type 2	Adhesion
−2.800	NM004934	Cadherin 18 type 2	Adhesion
−2.529	BC015877	Cadherin 19 type 2	Adhesion
−2.008	AW593060	Cadherin 20 type 2	Adhesion
−2.974	NM004389	Catenin alpha 2	Adhesion
−4.422	U96136	Catenin delta 2	Adhesion
−1.898	AA668763	Leupaxin	Signaling and adhesion
−2.069	AA749101	Interferon 1	Signaling and adhesion
−1.795	NM020242	Kinesin family member 15	Signaling
−2.716	AF002985	Chemokine 11	Signaling
−1.475	NM152364	Repetin	Extracellular matrix
−3.665	AK057680	Matrix metallopeptidase 2	Extracellular matrix
−1.910	NM002423	Matrix metallopeptidase 7	Extracellular matrix
−1.627	NM004994	Matrix metallopeptidase 9	Extracellular matrix
−1.389	U38321	Matrix metallopeptidase 19	Extracellular matrix
−1.747	NM022718	Matrix metallopeptidase 25	Extracellular matrix
−1.619	BE350145	Collagen VI alpha 1	Extracellular matrix
−1.789	U29343	Hyaluronan-mediated motility receptor	Cell motility
−3.122	AB046400	Serpin peptidase inhibitor 4	Cell survival
−1.458	N90191	Cyclin B1	Cell cycle
−1.556	AW183154	Kinesin family member 14	Cell cycle
−1.652	NM005733	Kinesin family member 20A	Cell cycle
−2.105	AA810156	Nuclear fragile X2	Cell cycle

* The full list of genes is available on our website (http://concave.concordia.ca)

Among these groups of genes, we subsequently focused on selected genes involved in apoptosis, cell cycle, cell survival, cell adhesion, and cell motility; therefore, we investigated the expression of 19 selected genes from these groups by RT-PCR (Figure 2-3). The total RNA used in this study was obtained from treated and untreated cells harvested from two separate experiments conducted in the same conditions and representing passage number 3 from two different batches of the same cell line. As expected from the array analysis, 9 of the selected genes (Rho GTPase 26, microtubule 2, GTP-binding protein 2, protein phosphatase 1, interleukin receptor 1, inhibin beta E, growth differentiation factor 15, forkhead a2, and activating transcription factor 3) were

found to be up regulated, whereas the other 10 selected genes (serpin peptidase inhibitor 4, chemokine 11, interferon 1, kinesins (14, 15, and 20A), leupaxin, cyclin B1, repetin, and hyaluronanmediated motility receptor) were down regulated in SWCNTs treated cells versus untreated cells at the RNA level (Figure 2-3 and Supplementary Figure S1, A and B in the online version of this article; Tables 2-2 and 2-3).

2.4 Discussion

This investigation, to the best of our knowledge, is the first microarray study on the effect of SWCNTs on HNBE cells. In this study we identified marked changes in the expression of 14,294 genes, with 7,029 genes being up regulated and 7,265 being down regulated. The majority of these genes are discovered for the first time to our knowledge as targets of SWCNTs exposure in human normal bronchial cells. It has been reported elsewhere that SWCNTs can provoke alveolar macrophage activation, chronic pulmonary inflammation, and granuloma formation in mouse models [146]; the investigators of this study used Affymetrix microarrays to explore the molecular effects on the macrophages when exposed to SWCNTs. They found that SWCNTs are able to activate various transcription factors such as nuclear factor kappa B (NF-κB) and activator protein 1 (AP1), which can lead to the induction of protective and antiapoptotic gene expression in these cell models. In our study we found that the NF-κB is slightly down regulated in HNBE cells treated with SWCNTs; however, we did not find the gene encoding AP1 on our list of genes. Although, our preliminary data show that SWCNTs provoke cell apoptosis of HNBE cells through the activating transcription factor 3 and transcription factor 15 and probably other transcription factors such as activating transcription factors

2 and 7 (unpublished data). On the other hand, Cui et al. [147] examined the effect of SWCNTs on the HEK293 cell line (human embryonic kidney cancer cells) using a small oligo-based microarray analysis related to cell cycle, cell apoptosis, and signal transduction; they identified genes such as those encoding cyclins A1, A2, C, D1, D3, G1, and G2; Cdks 2, 3, 4, and 6 of the cell cycle; and p16, Bax, Hrx, Bak1, p53, and TGFβR1 of cell apoptosis, as well as Mad2, Jak1, Ttk, Tyk2, Pa2g4, and early growth response 1 of the signal transduction group) as being differentially expressed in HEK293 kidney cancer cells treated with SWCNTs in comparison with untreated cells. Herein we report for the first time to our knowledge a complete list of gene targets of SWCNTs in HNBE cells, and we confirmed the deregulation of the majority of genes reported in the study of Cui et al on HEK293 cells (the full list of genes is available on our website: http://concave.concordia.ca). Moreover, in this study we show for the first time to our knowledge that protein phosphatase 1 is over expressed in HNBE SWCNTs-treated cells compared with untreated cells. This gene has an important role in growth arrest and DNA damage, and it is known to be correlated with cell survival [148-150]. Moreover, the activating transcription factor 3 gene was found to be up regulated in SWCNTs-treated cells. This gene has been reported to have an important role in cell apoptosis and carcinogenesis [151,152]. In addition, the interleukin receptor 1 gene is over expressed in HNBE cells treated with SWCNTs; this gene participates in cell signaling of airway inflammation through its activation by interleukin 33 [153,154]. On the other hand, treatment of HNBE cells with SWCNTs induces a down regulation of the hyaluronan-mediated motility receptor gene, which is involved in cell motility and cell growth [155,156]. Other important genes are reported to be down regulated, in this study, in

SWCNTs-treated cells as compared with untreated cells. This includes the chemokine 11 gene, which is part of cell signaling and motility [157,158]. Kinesin family members (14, 15, and 20A) were all found to be under expressed in SWCNTs-treated HNBE cells. These genes are correlated with cell proliferation, cell cycle, and trafficking [159-161]. Accordingly, our study is the first investigation to our knowledge to categorize the gene targets of SWCNTs in primary human normal lung cells using microarray analysis.

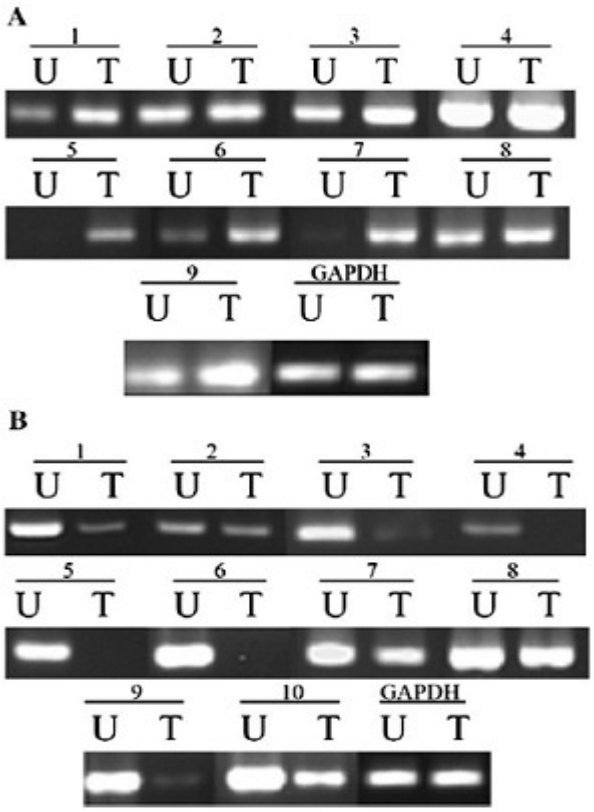

Figure 2-3 Validation of microarray data by reverse transcription-polymerase chain reaction (RT-PCR) on HNBE cells treated with SWCNTs (T) and their corresponding untreated HNBE cells (U).

In conclusion, the comprehensive identification and profiling of gene expression affected by SWCNTs in HNBE cells as reported in this study will add to our understanding of the mechanism of the effect of SWCNTs in human health, especially for the respiratory system. As other studies with new equipment and substances such as cell phones and microwaves have noted [162-164], we believe that this systematic approach toward gene identification will be useful in the discovery of the real effect of new materials and/or technologies on human health.

CHAPTER 3. A novel approach of noninvasive cell proliferation assessment using Fourier transform infrared (FTIR) spectroscopy

Presented in this chapter is the UV spectroscopic investigation of cell culture media toward cell growth analysis. The work is based on an article published in Medical Hypotheses [128]. It covers the objective (ii) of the "Thesis objective and scope" in section 1.3.

3.1 Introduction

The quantification of cellular growth by analyzing their proliferation rate has become an essential tool in any laboratory working on cell-based studies. Such a technique enables not only the optimization of cell culture conditions, but also the determination of growth factor and cytokine activity. Moreover, the efficacy of therapeutic agents in drug screening, the cytostatic potential of anticancer compounds in toxicology testing, and even cell-mediated toxicity can be assessed when quantifying cell growth. Cell proliferation assays also permit the study of the effect of certain genes on cell growth regulation and differentiation in cell biology. These analyses are largely used in cancer research to explore the effect of several oncogenes as well as new drugs *in vitro*. For the purpose of measuring cell proliferation or enumerating cells, fluorescent stains, such as light-scattering, are often used [165]. More importantly, methods for counting cells and quantifying cell proliferation are becoming valuable diagnostic tools in various areas of biological research. Presently, most cell proliferation assays estimate the number of cells

by measuring total nucleic acid or protein content of lysed cells [166,167]. However, the sensitivity of the existing fluorescent dyes allows the detection and quantification of cells only under certain circumstances related to their migration to the target site [168-172].

On the other hand, infrared spectroscopy has proved to be a powerful tool for the study of biological molecules and the application of this technique to biological problems. This area of research is continually expanding, particularly with the advent of increasingly sophisticated sampling techniques associated with FTIR spectroscopy in recent decades.

Biological samples including animal tissues, microbial cells, and clinical samples have all been successfully studied for the characterization of isolated biological molecules, particularly proteins and lipids [173]. We developed a new technique to study cell proliferation that is based on FTIR and the density of cell culture medium. We confirmed the viability of our technique using the BT20 breast cancer cell line and NEF cells and those expressing E6/E7 onco-proteins of HPV type 16, which grow faster than their wild type cells. Using our method, we found that the gap between the two line spectra shows the difference in medium density between wild type cell lines and those expressing E6/E7 onco-proteins (Figures 3-1a and 3-1b). A total of 10^6 cells were initially incubated in 2mL of growth medium; the higher the cell proliferation rate, the higher the transmission spectrum was. This observation was related to the rate of cellular proliferation and is confirmed using traditional cell counting techniques (Figure 3-1c). Moreover, we were able to assess the cellular proliferation ability of the HeLa cell line using our new methodology (Figure 3-1d): 10^6 cells were initially incubated in 2 mL of growth medium. The shift of the spectrum first up, then down, illustrates the need of fast and continuous

monitoring of changes in the culture medium during incubation, for a better understanding of cell growth.

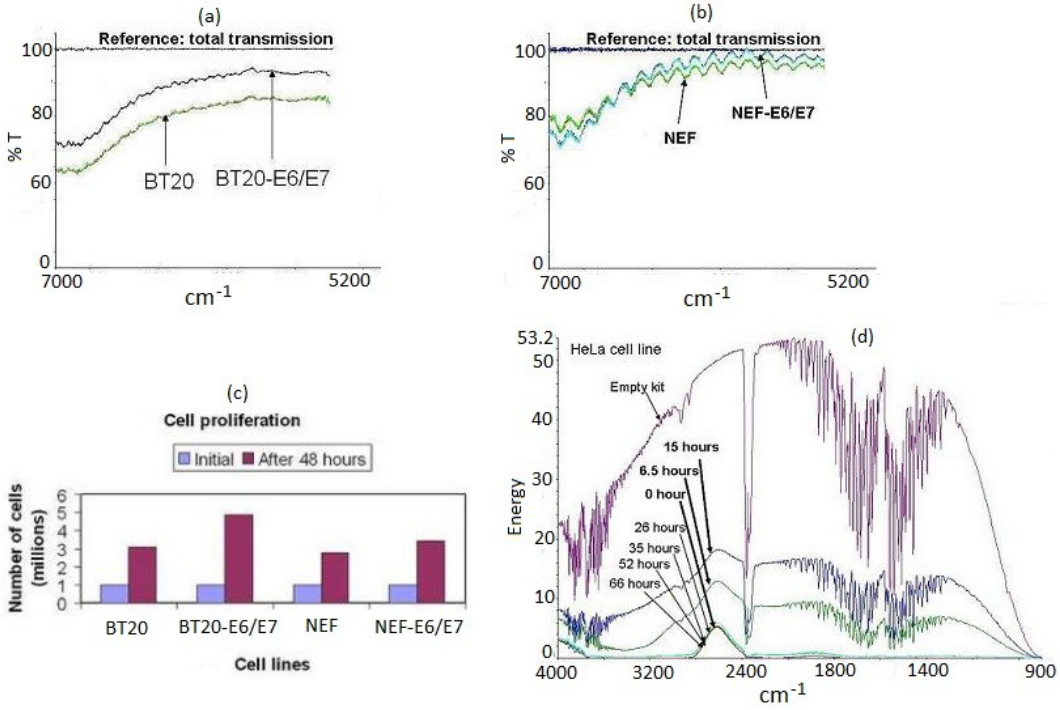

Figure 3-1 (a) and (b) Transmission spectra of the culture media after 48 hours incubation of BT20, BT20-E6/E7, NEF, and NEF-E6/E7 in the 7000-5200 cm-1 near infrared range. (c) Confirmation by cell counting. (d) Single beam spectra of empty kit and culture media after 0, 6.5, 15, 26, 35, 52 and 66 hours cultivation of HeLa cell line.

In this technique, we used two separate pieces of equipment: a cell culture incubator and an FTIR machine. Herein, we propose the integration of the cell culture incubator into the FTIR machine in order to use it as a new methodology to study cellular proliferation.

3.2 The hypothesis

We developed a new technique to study cellular proliferation; our technique is based on infrared spectro-photometry and the density of cell culture medium using two separate pieces of equipment: an FTIR spectrometer and a cell culture incubator. In this paper, we

hypothesize the possibility of combining, simultaneously, the operations of culturing cells and analyzing progressive changes in the medium with infrared technology, for assessing the rate of cell proliferation or the effectiveness of specific drugs on cell growth *in vitro*. Therefore, we firmly believe that the design of a tissue culture mini-incubator, with an overall size small enough to fit into the FTIR workbench while allowing continuous irradiation of the culture medium only, is a promising tool in medical research especially cell biology. Schematic arrangement of the experimental setup is shown in (Figure 3-2).

3.3 Evaluation of the idea

In our experiments, we used human breast cancer cells (BT20) and mouse (NEF) as well as those expressing E6/E7 onco-proteins of HPV type 16 and a human cervical cancer cell line (HeLa) which expresses E6/E7 onco-proteins of HPV type 18. All cell lines were grown in RPMI medium (Gibco, Grand Island, NY) supplemented with 5% Fetal Bovine Serum (FBS; Gibco). Cell cultivation was performed either in 100 ml dishes with 6ml volume of growth medium, containing 1x106 cells or in 6 wells cell culture plates (Corning Incorporated, Corning, NY) with 2ml volume of growth medium containing 1x106 cells; these were then incubated at 37oC in 5% CO2 atmosphere, and the growth media were collected for analysis.

The Perkin Elmer Spectrum BX FT-IR spectrometer was used for sample collection and testing. In order to analyze the collected media, radiant beams were divided, an optical path difference between the beams was generated, and the beams were recombined in order to produce repetitive interference signals. These signals contained Infra-Red

spectral information generated after passing through the samples and were measured as a function of the optical path difference by means of a detector.

The results obtained thus far correlate with cell counting and existing knowledge on E6/E7 oncogenes which promote cell proliferation (Figure 3-1a, 3-1b and 3-1c). Moreover, the medium collected from culturing the HeLa cervical cancer cell line was tested at different incubation durations, confirming the change in medium density with increasing proliferation and cell viability (Figure 3-1d), and illustrating the need for continuous monitoring of cell growth. These results indicate the importance of continuous FTIR analysis for cellular proliferation assessment during incubation periods.

3.4 Discussion and conclusion

There is sufficient evidence in the literature showing that infrared irradiation causes different inhibiting effects on cells [174,175]. It has also been established that conventional FTIR spectroscopy can be used to identify vibrational modes of some major compounds both in normal and tumor tissues and cells [176-181], as well as the identification of various biomolecular components of the cell [182,183], and for monitoring the characteristic changes in the molecular compositions and structures that accompany cellular changes resulting from viral infections or transformations from a normal to a malignant state [184-190]. Moreover, several human cancers have been successfully investigated using FTIR as a diagnostic tool, these include lung, breast, cervical, prostate and colon cancers [191-195].

All of these applications are based on irradiation of the cells with infrared, thus introducing functional changes in the cells' metabolism, and therefore not allowing the

use of the tested cell population in other assays. The proposed technique in this paper, however, is based on the assumption that the culture medium becomes more transparent to infrared as the proliferation rate increases, as shown in (Figure 3-1). Therefore, the combination of cell culturing and monitoring of the variation in the culture medium for cell proliferation assessment is necessary for non-destructive and real time analysis, especially since the two operations performed successfully have shown comparable results. It is therefore worthwhile to design a suitable mini-incubator for that purpose, since none of the existing ones can suit this application. The overall system, a mini incubator incorporated in the FTIR machine (Figure 3-2) may be valuable for all cell proliferation analyses, allowing fast and easy assessment (a 1 to 5 minutes single scan is enough to get a complete spectrum), and requiring no sample preparation. Furthermore, only a small amount of sample (culture medium) is required, which allows testing of micro-volumes instead of milli-volumes. Because multiple spectra can be readily collected in 1 minute or less, sensitivity can be greatly improved by increasing the signal to noise ratio through the co-addition of many repeated scans. These advantages may open new possibilities in medical research. Moreover, we believe that the design of a mini- tissue culture incubator integrated with an FTIR, will be a promising tool for biological research especially for cellular proliferation assays.

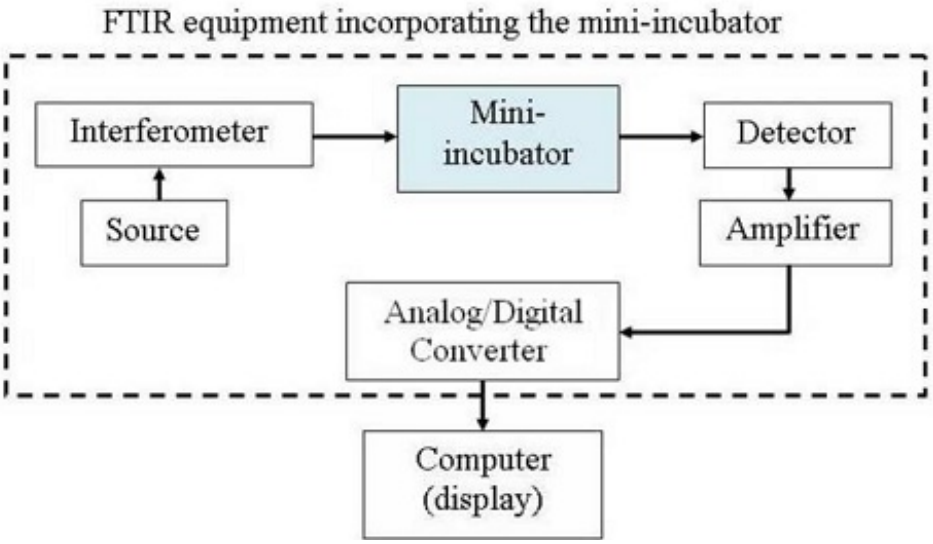

Figure 3-2 Simplified optical layout of the block diagram of the Fourier transform infrared machine, with the proposed incorporated mini-incubator for real time cell proliferation assessment. This will allow simple assessment of changes in the culture medium, without manipulating the cells.

CHAPTER 4. Bio-analysis of living cells from acoustic conditioning in vitro

Presented in this chapter is the effect of low power US on the proliferation and invasion abilities of human cancer cells in vitro. A numerical analysis approach was derived in the "Methods" in section 1.4, and exploited in the experimental study here. The results are discussed and validated with bioassays. This chapter is based on an article published in Clinical Cancer Investigation Journal [129]. It complements the methods presented in chapters 2 and 3, and specifically covers the objective (i) of the "Thesis objective and scope" in section 1.3.

4.1 Introduction

In recent years, bioengineering researchers have expanded their efforts into the area of non-ionizing radiation. Nowadays, the great interest of biology and medicine to ultrasonic methods is evidently proven. Ultrasound usually interacts with human tissue by generating heat [196-199], but also through non-thermal effects which are ascribed to cavitation [200-202]. Moreover, a fast development of nonlinear ultrasound took place in the second part of the last century; this was promoted by the emergence of ultrasonic technology and was emphasizing on high intensity ultrasound generation [203]. Meanwhile, an investigation of the biophysics of ultrasound interaction with biological samples at cellular level is evidently complex, due to the small size of a cell. The interaction of ultrasound with biological tissues has led to several clinical therapies such as physiotherapy [204], transdermal drug delivery[205], thrombolysis [206], and cancer

treatment [207]. These therapies are generally based on physical effects of ultrasound on cells and tissues such as controlled disruption of various biological barriers like cell membranes and tissues for drug and gene delivery [208-210]. Several effects of ultrasound have also been studied in isolated cells, cell suspensions and – or cell cultures *in vitro*. It is worth mentioning here that studies of isolated cells or cells in culture provide a means for examining the effect of ultrasound without numerous biological variables operating in the whole organism. Nevertheless, such simplification reduces the applicability of the experimental data in clinical environment, but allows a better understanding of physiological changes due to ultrasound exposure. However, little is known about subtle biological effects such as specific proteins up or down-regulation on cells. The aim of the present work was therefore to investigate the effects of low power ultrasound on the cell proliferation and invasion *in vitro* as well as some key genes associated with these events.

4.2 Materials and Methods:

4.2.1 Ultrasound exposure system

The experimental arrangement for the ultrasound exposure of cells is shown in Figure 4-1. The experiments were conducted using commercially available piezoelectric ceramic transducers Pz27 Disc 5x1 mm (FERROPERM Piezoceramics A/S, Denmark). The transducer was glued with a thin conductive epoxy layer at the bottom of the culturing plate, acting as an actuator to generate the ultrasound wave on the cells, through the wires connected to a waveform generator (Agilent 33220A/20MHz Function/arbitrary waveform generator, Santa Clara, CA, USA). The signal was a continuous sinusoidal

wave with an amplitude of 3Vrms applied to the transducer, giving a thickness variation in service of 10^{-3} μm (initially measured using an accelerometer). The transducer had a bandwidth of 0.7 to 1.1 MHz, and the frequency was kept at 800-kHz (within the range of therapeutic ultrasound) over an exposure time of 6 hours, in order to see the influence of a longer time of ultrasound exposure. The beam profile was not established. The adopted parameters also prevent of having cavitation effect, which can be an underlying cause of cell damage.

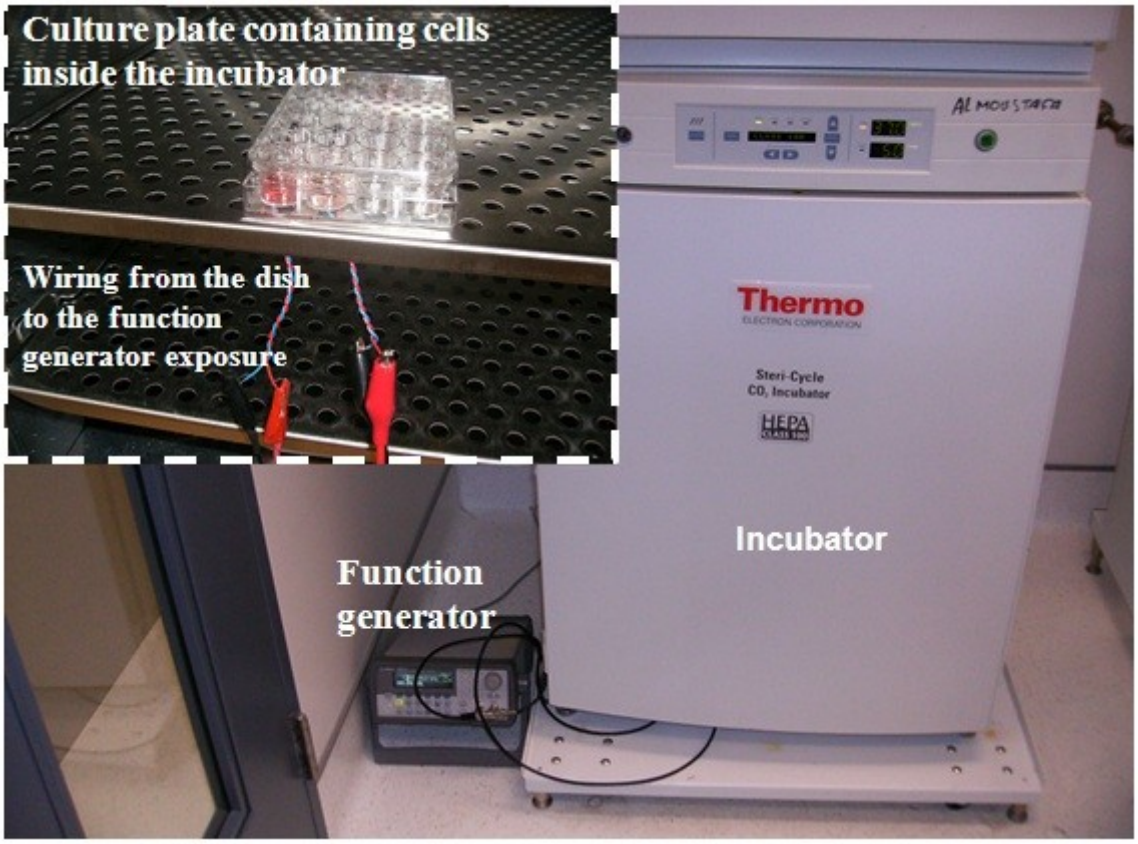

Figure 4-1 Experimental arrangement for the ultrasound exposure of cancer cells under incubation.

The culturing plate is made of polystyrene with a thickness (distance travelled by sound waves before reaching the cells) of 1 mm. Ultrasound waves consist of cycles of compression and expansion exerting a positive and negative pressure. These pressure cycles are known to act on the molecule by pulling them together and pushing them away. The ultrasound power has been calibrated between ($0\text{-}10^{-3}$) W/cm^2 of radiation sound intensity of the transducer, with the PVDF membrane hydrophone method.

4.2.2 Cell lines

Human breast cancer cell lines, BT20 and BT20-E6/E7, as well as human cervical cancer cell line, HeLa were obtained from the American Type Tissue Culture. HeLa cells were selected for their high invasion ability, while BT20 cells were chosen for their relatively low invasion ability compared to HeLa cells [211,212]. All three cell lines were cultured in RPMI medium (Gibco, Grand Island, NY) supplemented with 5% Fetal Bovine Serum (FBS) and 1% penicillin/streptomycin, and 2 mM L-glutamine (Life Technologies, Inc.). Cells were incubated at 37 ^{o}C in 5% CO_2 atmosphere.

4.2.3 Proliferation assay

The cells were cultured in flat-bottomed 12-well plates (Costar, Cambridge, MA). A concentration of $100x10^3$ breast cancer cells (BT20 and BT20-E6/E7) were initially plated and incubated two hours prior to ultrasound exposure. This time is required for the cells to adhere on the substrate before ultrasound excitation. Each cell line was seeded in two wells, one for the control sample (unexposed to ultrasound) and one for the treated sample (to be exposed to ultrasound). Next, ultrasound excitation was turned on for 6 hours, and turned off. Cells were left incubated for 56 additional hours before being taken

out for counting using a hemocytometer. A triplicate test was performed for each sample and the average value was considered for our analysis.

4.2.4 Cell cycle analysis

HeLa and BT20 cell lines were exposed to ultrasound under the conditions described above. Next, cells were harvested, washed, fixed and subsequently treated with 50µg/mL RNase and stained with 50µg/mL propidium iodide for 30 minutes. They were then analyzed in a FACS Calibur machine, and data were evaluated with Cell Quest and ModFitLT v3.1 software.

4.2.5 Invasion assay

Cell invasion was performed in 24-well Biocoat Matrigel invasion chambers (8 µm; Becton Dickinson) according to the manufacturer's protocol (Figure 4-2). Only BT20 and HeLa cell lines were used. A concentration of $50x10^3$ wild type and treated (by exposure to ultrasound) cells were plated in the top chamber. The bottom chamber contained RPMI medium. These cells were also allowed to adhere on the substrate (two hours), and ultrasound was activated for 6 hours, then stopped (Figure 4-2-A). After 16 additional hours of incubation, invasive cells have passed through the Matrigel layer onto the surface of the membrane (Figure 4-2-B). The noninvasive cells were removed with a cotton swab. The cells that migrated through the membrane were rinsed, fixed with methanol and stained with hematoxylin (Figure 4-2-C and 4.2-D). For quantification, cells were counted under a microscope in five predetermined fields. A triplicate test was performed for each sample and the average value was considered in the cell counting. BT20 was used here as a reference because it is a non-invasive cell line. In fact, it has

been shown that the invasion and metastatic abilities of BT20 are induced by E6/E7 oncogenes of Human Papillomavirus (HPV) type 16 [211].

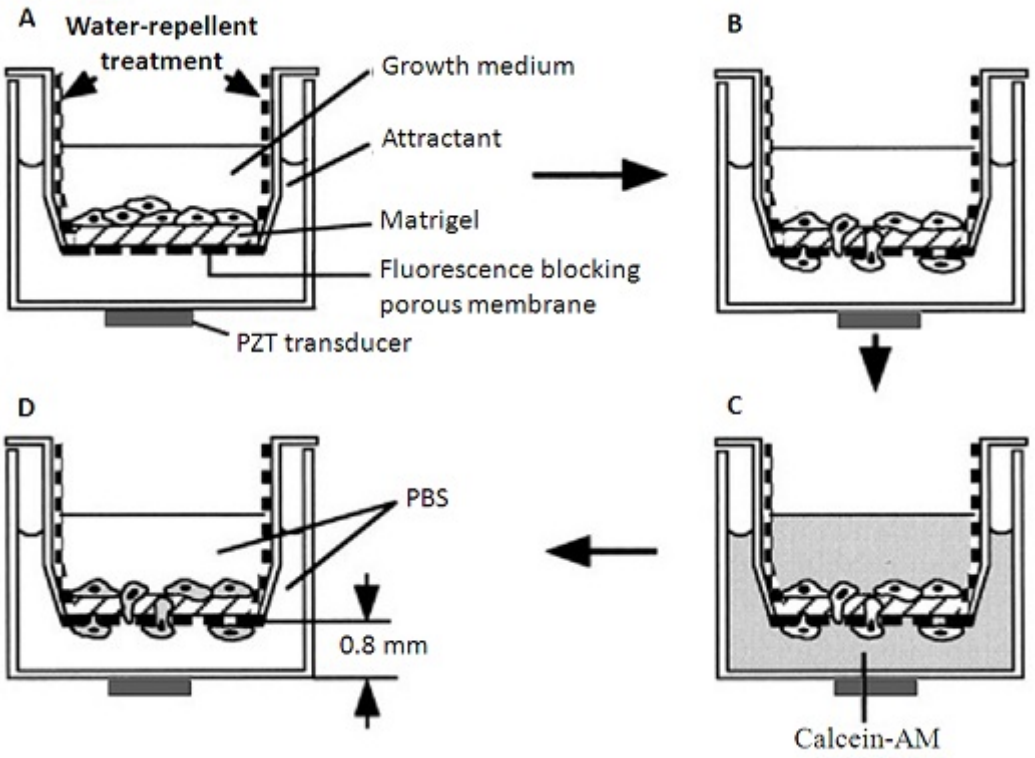

Figure 4-2 In vitro cell invasion protocol.

4.3 Western Blot analysis

This assay was performed as previously described [213]. But in our experiment, anti-Cdk-6, Id-1, Caveolin, EGF-R (clone 13) (Bio/Can Scientific), as well as anti-actin (Clone C4, Roche Diagnostics) were used in the assays.

4.4 Results and discussion

Figure 4-3(a) shows the effect of ultrasound exposure on the two breast cancer cell lines proliferation. The cell proliferation rate consistently decreases with ultrasound wave excitation. This effect was already reported in the literature by Watanabe et al. [210], for cancer cells of mouse T lymphoma (EL-4). In their work, Watanabe et al. reported that when cancer cells are exposed to ultrasound, hydroxyl radicals are generated and DNA molecules from cancer cells become segmented due to hydroxyl radicals. Apoptosis is then induced and the proliferation of cancer cells is suppressed. Our study complements this observation by using a simpler experimental arrangement and pointing out cell cycle arrest by ultrasound to be the reason in the decrease of the proliferation rate.

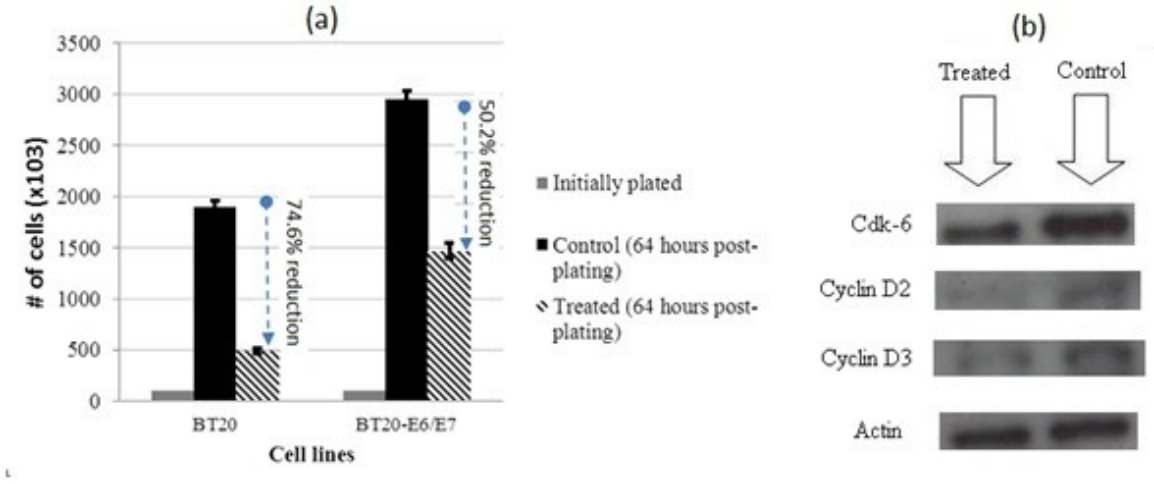

Figure 4-3 (a) Effect of ultrasound exposure on the proliferation rate of two breast cancer cell lines (BT20 and BT20-E6/E7). (b) Western blot analysis of Cdk-6, cyclin D2 and cyclin D3 expression in BT20-untreated and treated cells.

Moreover, with an ultrasound power far below what was reported by Watanabe et.al, we succeeded to achieve a 74.6% and 50.2% reductions in the number of BT20 and BT20-E6/E7 cells respectively, compared to a 90% reduction obtained by Watanabe et.al. [210], in 48 hours with EL-4 cancer cells. The difference observed in the proliferation reduction of BT20 and BT20-E6/E7 is justified by the E6/E7 genes, which are known to be cell proliferation stimulators.

The histogram statistics from the cell cycle data are shown in table 4-1 in terms of percentage gated events in each phase of the cell cycle. A total of 9500 and 9953 events were gated out of 12965 and 12395 for the control and the treated HeLa samples respectively, whereas 9989 and 9810 events were gated out of 12783 and 14019 for the control and the treated BT20 respectively.

Cell lines		Go/G1	S	G2M
HeLa	Control	68.05	17.22	15.05
	Treated	57.91	10.46	30.78
BT20	Control	57.25	22.61	18.03
	Treated	54.02	24.25	21.91

Table 4-1 Cell cycle histogram statistics for HeLa and BT20 cell lines in terms of % gated events. Each value represents the average of a triplicate measurement ($p < 0.05$).

The table shows that, when exposed to a low power ultrasound, the G2M phase of the cell cycle is significantly affected in HeLa cells. In fact, 30.78% G2 in cells exposed to ultrasound versus 15.05% of the "control" population shows that ultrasound significantly induces cell cycle arrest. Moreover, we show that ultrasound exposure of the breast cancer cells studied provokes a loss of cell cycle controllers leading to deregulated cell proliferation. In fact, the cell cycle progression is regulated by the activities of cyclin-

dependent kinases and their subunits known as cyclins [214]. When these key genes are deregulated in human neoplasia, they often result in over/down-expression of CDKs and cyclins, as well as loss of natural inhibitors of CDKs, and consequently hyper-activation of CDKs. In this study, we report for the first time that low power ultrasound can inhibit Cdk-6, Cyclin D2 and Cyclin D3 in human breast and cervical cancer cells as shown in Figure 4-3(b). Therefore, our data suggest that low power ultrasound, when applied in the conditions described here, inhibits cancer cells proliferation in vitro. These results complement those obtained by Hrazdira et al. [215] who showed that exposed to a 0.8MHz low intensity ultrasound (100mW/cm^2) for 10 minutes, HeLa cells exhibited partial inhibition of proliferation. Their study showed that cells were most sensitive when undergoing M- and S-phases of the cell cycle.

Figure 4-4-(a) shows the effect of ultrasound on cell invasion ability with the procedure described in Figure 4-2. From a total of 50x10^3 cells initially incubated, 10% of HeLa cells and 0.32% of BT20 cells not exposed to ultrasound (control samples) have passed the matrigel after 24 hours of incubation. For cells exposed to ultrasound, only 4.19% of HeLa and 0.23% of BT20 have crossed the matrigel layer, giving a reduction due to ultrasound waves of 59.1% for HeLa cells and 28.1% for BT20 cells.

Western blot analysis was further performed. The results in Figure 4-4-(b) confirmed the down-regulation of Id-1, Caveolin and EGF-R genes which are widely considered main regulators of cell invasion and metastasis of human cervical cancer cells [216-220]. Therefore, we report for the first time here that low power ultrasound inhibits cell

invasion of human breast and cervical cancer cells through Id-1, Caveolin and EGF-R down-expression.

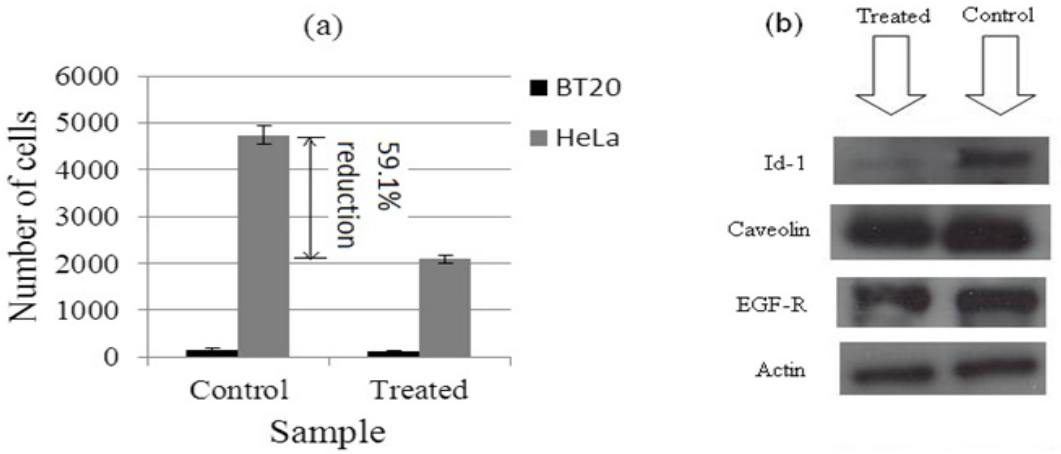

Figure 4-4 (a) Number of cells crossing the matrigel membrane from the procedure described in Figure 4-2. (b) Confirmation of down-regulation of Id-1, Caveolin, and EGF-R by western blot analysis of HeLa cells.

From the above results at low acoustic power, non-thermal mechanisms for biological change may be predominant. In general, as the pressure increases, cavitational and thermal effects become more important until, at a higher level, heating effects mask all others [221]. We have chosen to avoid this in our experiment by the use of low acoustic pressure amplitude with a sound intensity far below the intensity necessary for stable production of bubble in mammalian tissue using a pulse echo technique ($8x10^{-2}$ W/cm^2), as reported by ter Haar [222]. This is also far below the ultrasound intensity of 0.5 to 3.0 W/cm^2 used for therapy as reported by Galperin et al. [223], and up to 2750 W/cm^2 as reported by Chapelon et al. [224]. At such a low ultrasound intensity level, the heat produced is rapidly diffused out, resulting in a negligible change in local temperature

(Figure 4-5). Moreover, it is generally accepted that many non-thermal effects of ultrasound in biologic systems are attributable to cavitation [225]. Therefore, our study provides an additive information to the scientific community, by illustrating the alteration of cellular proliferation and invasion ability due to sound waves, thus strengthening the use of this type of waves as a potential candidate to stimulate therapeutic effects on cells. This is in line with some other studies reported in the literature [226,227].

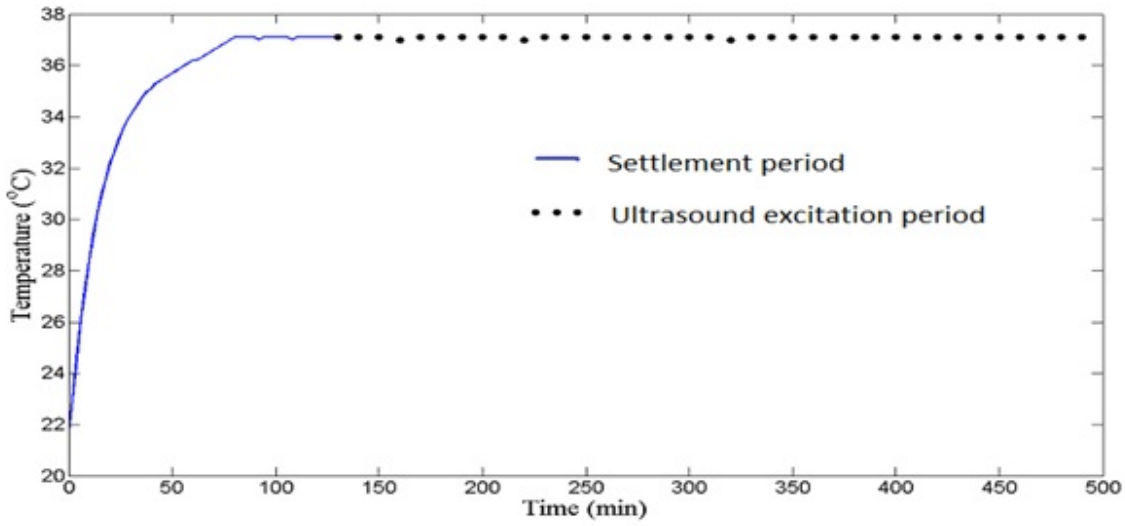

Figure 4-5 Temperature monitoring on the substrate where cells lie during ultrasound exposure. During the 6 hours ultrasound excitation period (dotted line), no meaningful increase in temperature occurs, showing that heating is not the cause of the bioeffects observed on cells.

4.5 Conclusion

We have examined the effect of low power ultrasound in human breast and cervical cancer cell lines, BT20 and HeLa. Its ability to significantly reduce cell proliferation rate of breast and cervical cancer cells, BT20 and HeLa *in vitro*, was demonstrated.

Moreover, it is also shown, for the first time, to consistently reduce cervical cancer cell invasion ability. The data presented suggest that Cdk-6 is one of the most sensitive proteins for action of low power ultrasound among proteins involved in cell cycle, whereas Id-1, Caveolin and EGF-R are the most sensitive involved in cell invasion of the cell lines studied. These results are important for medical applications and suggest that low power ultrasound may show a good promise in cancer therapy. This opens the perspective of using a controlled absorption of ultrasound for a therapeutic purpose. However, non-thermal effects of ultrasound such as radiation stress in biological samples still need a better theoretical foundation and physical understanding; therefore, new theories based on numerical and experimental data should be developed in the future.

CHAPTER 5. Cell culture media UV absorbance-based cell growth analysis

Presented in this chapter is the feasibility of using the spectrophotometry of culture media with an integrated minimal sample retention system as a practical and non-invasive alternative to traditional bioassays requiring cells detachment. This work is based on an article in press in Spectroscopy Letters [130]. It complements the methods presented in chapters 2, 3 and 4, and covers both objectives (i) and (ii) of the "Thesis objective and scope" in section 1.3.

5.1 Introduction

Cellular proliferation and cytotoxicity studies are the mainstay for cell biology and cancer research. On one hand, cell proliferation research involves the analysis of different molecules ability to express cell growth and multiplication. On the other hand, antitumor chemotherapy studies involve the analysis of the ability of specific agents to kill tumor cells. In both cases, an assessment of the change in cell number over time is critical, and performing it in a noninvasive way is challenging. Seen in this light, cell to substrate interaction as well as substrate surface treatment are known to affect cell behavior [228-231]; monitoring this process through the culture media is therefore key in that it has the potential to assess cell viability without requiring detachment of the investigated cell population from the surface during in vitro analysis.

The surface modification of polymers by cold plasma has drawn a lot of attention due to the key feature that the modification is restricted to the outermost layer (several hundred

angstroms) without altering the bulk properties of the material. Plasma treatment is known to modify the surface properties, such as the wettability, adhesion, topography, and biocompatibility which is concerned in our study. It is a rapid, clean and non-solvent process that can be used to introduce a specific element or functional group onto the surface of a polymer by selecting a suitable gas [232]. In this study, we use an oxygen-containing plasma (air) to cause surface functionalization of PDMS substrate for cellular growth. This is due to the incorporation of oxygen-containing components such as $C-O$, $C=O$, $O-C=O$, and $O=C-OO$ onto the surface [233].

In order to identify cells response to variations in physico-chemical substrate properties resulting from different grades of PDMS base-curer ratio (stiffness) and different doses of plasma treatment, the Nucleic Acid Concentration (NAC) as well as the absorbance of both the cell culture media and its nucleic acid were considered. The biocompatibility of the fabricated substrate surfaces was warranted by plasma-induced treatment of the substrate [230] in conjunction with cell counting, and we use the spectrophotometry of the culture media to indirectly assess cell proliferation and toxicity. Such a novel viability test based on the biochemical information extracted from the culture media may be preferred over other tests based on flow cytometry [234,235] or laser scanning cytometry [236]. Indeed, it does not require detachment of the studied cells from the surface during analysis.

5.2 Materials and method

PDMS substrates of various stiffness values were obtained using a Sylgard 184 elastomer kit (Dow Corning, Barry, UK) with the pre-polymer (base) to hardener (curing agent)

ratios of 3:1, 5:1, 8:1, 10:1, 20:1, and 30:1 (w:w), corresponding to cross-linker concentrations of 33.3, 20, 12.5, 10, 5, and 3.3% respectively. We have selected such a wide mixing ratio range in order to highlight the importance of base and crosslinker ratios for stiffness-based biocompatibility of PDMS. The solutions were mixed in sterile conditions and degassed, then poured into 60 mm dishes to a depth of about 1 mm. The mixed and degassed solutions were cured at 75^{o}C for 2 hours. The substrates stiffness values were measured with an Atomic Force Microscope (AFM) in tapping mode (Veeco Instruments, MultiMode AFM) using a 20 nm radius probe (MikroMasch, NSC15).

PDMS consists of repeating units of $-OSi(CH_3)^{2-}$. It is a durable, homogeneous, deformable, and isotropic elastomer with a low interfacial free energy and chemically inert surface. Due to the CH_3 groups, the PDMS surface is very hydrophobic. It can be made hydrophilic by treating the surface with oxygen plasma, which introduces silanol groups (Si-OH) on the surface by oxidation of methyl groups ($Si-CH_3$) of PDMS at the plasma/polymer interface (Figure 5-1). The PDMS substrates were then exposed to an air plasma for 10 minutes at 7.16 W (Low dose), 10.15 W (Medium dose) and 29.6 W (High dose) power levels, using a plasma machine (Harrick, model PDC-002), with air entering the chamber at 150 Pa. All plates were then exposed to UV light in the biological safety cabinet for further sterilization, from a transilluminator for 5 minutes at a distance of 30 cm. Hydrophilic stability was needed, and hence, the liquid culture medium was poured on top of the substrates after sterilization. PDMS was chosen because it is inexpensive, flexible, impermeable to water, and most important for our purpose, non-toxic to cells.

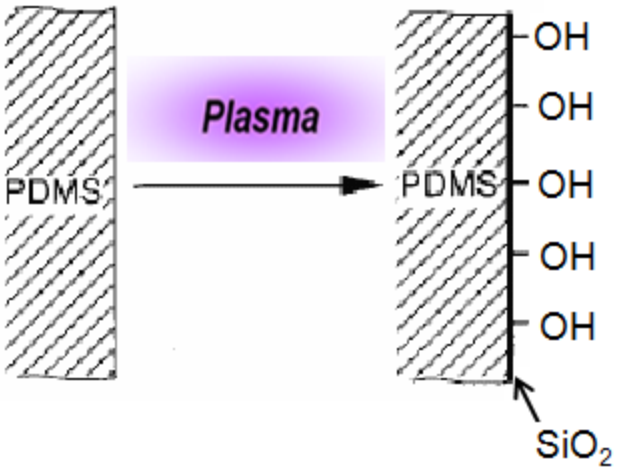

Figure 5-1 Surface modification with air plasma treatment. Silanol groups (Si-OH) are introduced on the surface of PDMS by oxidation of methyl groups (Si-CH3), offering a better growth environment to cells.

The cancerous cervix cell line, HeLa, was chosen because it is relatively robust and hence ideally suited for adhesion experiments. The cell culture medium was the Dulbecco's Modified Eagle's Medium (DMEM) supplemented with 10% (v/v) Foetal Bovine Serum (FBS) and 1% penicillin-streptomycin (100 units/mL, HyClone). Cells were prepared at a concentration of approximately 3000 cells/µl. In this case 10 µl have been added, i.e. roughly 300000 cells per dish (in 60 mm Petri dishes). In order to allow a longer time of observation on the same cell population, we have added enough quantity of cell culture medium (in this case 6 ml) in each dish and 10 µl of cell solution. Cells were then incubated at 37^{o}C in a humidified 5% CO_2 environment.

A volume of 100 µl of the cell culture media was collected at 24, 48 and 96 hours post-plating, spun at 1200 RPM in order to isolate potentially swimming cells, and a volume of 1 µl was analyzed for the absorbance of the media as well as the nucleic acid

concentration in the media. These measurements were performed on a Thermo Scientific NanoDrop 8000 spectrophotometer, according to the instrument's procedures. This equipment functions by combining fiber optic technology and natural surface tension properties to capture and retain minute amounts of sample independent of traditional containment apparatus such as cuvettes or capillaries. Shorter path lengths are employed, which result in a broad range of concentration measurements, essentially eliminating the need to perform dilutions.

For estimating the number of cells, images of cells growing on each substrate were captured using a Nikon, TE2000-S inverted microscope. Twenty distinct snapshots of representative areas of each dish were examined with the freeware ImageJ software (available at http://rsb.info.nih.gov/ij). In order to confidently use this approach in our investigation, a set of 48 hours post-plated cells was made available for cell count using the standard hemocytometer technique and ImageJ software. Similar results were obtained with a difference in cell number ranging from 2 to 5%.

5.3 Results and discussion

The difference in PDMS substrate stiffness rendered by the variation of the cross-linker concentration is shown in Figure 5-2. The stiffness value increases, reaches a maximum, then decreases within the cross-linker concentration analyzed (from 3.33 to 33.33%). This trend is comparable to the one obtained by Evans et al.[229], who measured the Young's modulus of PDMS at cross-linker concentrations varying from 1 to 23%. This technique is a versatile and easy to implement *in vitro* method of inducing mechanotransduction on cells, for which the exchange with the extracellular environment

(here the culture medium) can be noninvasively characterized with spectrophotometry of a small volume of culture medium.

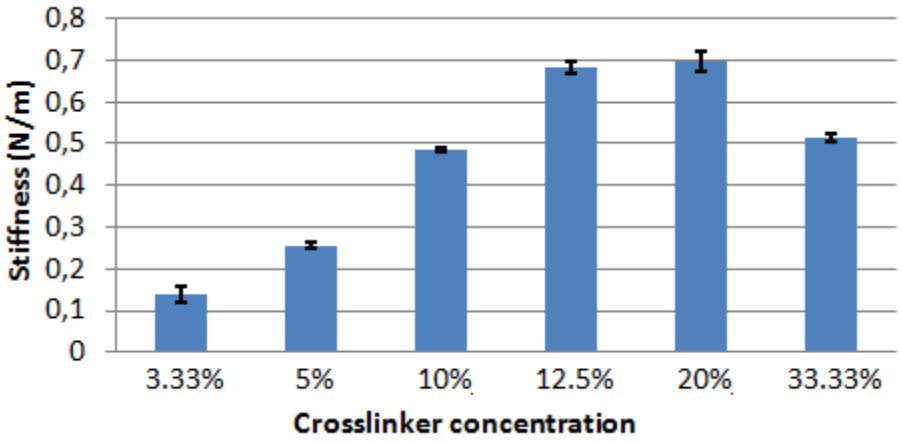

Figure 5-2 Stiffness of PDMS of different grades (cross-linker concentration).The values and error bars represent the mean and standard deviation of ten measurements on each sample.

Table 5-1 shows the effect of substrate stiffness on cell proliferation rate for the highest available plasma dose (29.6 W) in our equipment. Indeed, plasma exposure turns the PDMS substrate from hydrophobic to hydrophilic, offering a better environment for cell growth. From this table, the cell count on the substrate with 10% cross-linker concentration represents 89.5%, 82.8%, and 95.6% of the reference values (cell count on standard tissue culture plate) after 24, 48 and 96 hours of culture respectively. We therefore consider the fabricated and treated PDMS substrates biocompatible enough to pursue our investigation. Moreover, when fabricating substrates for long-term cell culture, the material properties should not adversely affect cell growth. Therefore, proper cure weight ratio of prepolymer to hardener should be selected.

Table 5-1 Effect of substrate stiffness on cell proliferation rate. The values represent the average (Mean) and standard deviation (SD) of a triplicate measurement.

No. of HeLa cells per mm^2				
Hours in culture	TCP	PDMS 10:1	PDMS 30:1	PDMS 50:1
	Mean ± SD	Mean ± SD	Mean ± SD	Mean ± SD
24	201 ± 5	180 ± 6 *	159 ± 4 *	170 ± 7 *
48	436 ± 7	361 ± 5	340 ± 7 **	297 ± 9
96	1957 ± 10	1872 ± 12	1255 ± 15	1170 ± 20 ***

* Indicates significant difference ($P < 0.05$) from value of TCP at 24 hours. ** Indicates significant difference ($P < 0.05$) from value of PDMS 10:1 at 48 hours. *** Indicates significant difference ($P < 0.05$) from value of PDMS 30:1 at 96 hours.

In addition to the substrate stiffness influence, table 5-2 illustrates the effect of the plasma treatment dose (RF power level) on the biocompatibility level of the substrate. The cells from substrates with 3.33% and 10% cross-linker concentrations were counted at 48 hours of incubation and compared. This was done on cells grown on substrates exposed to low dose (7.1 W), medium dose (10.15 W), and high dose (29.6 W) plasma treatment. We observe that the higher the power of irradiated plasma, the better the environment for cell growth. Such a cell response, triggered by the nature of the chemical bonding on the surface of the substrate, can also be subject to spectrophotometry analysis of the culture medium, without the need of detaching the cells.

We aimed at showing that the exchange between cells and the extracellular environment, triggered by the variation in the mechanical property of the substrate and the plasma exposure dose, can readily be obtained by a qualitative and a quantitative analysis of a micro volume sample of the culture medium with a spectrophotometer system. Therefore, Figure 5-3 presents the absorbance of the fresh medium (our reference measurement FM), and of the cell culture media collected after 48 hours of cultivation on substrates exposed to low dose (L, 7.16 W), medium dose (M, 10.15 W), and high dose (H, 29.6 W) plasma irradiation.

Table 5-2 Effect of the plasma RF power level on the biocompatibility level of the substrate. The values represent the average (Mean) and standard deviation (SD) of a triplicate measurement.

No. of HeLa cells per mm^2		
RF power level	PDMS 10:1	PDMS 30:1
	Mean ± SD	Mean ± SD
Low	272 ± 12	189 ± 14
Medium	297 ± 7	204 ± 11
High	361 ± 5 *	340 ± 7

Significant differences ($P < 0.05$) were found between the two substrates at corresponding power level. *indicates significance difference ($P = 0.0001$) from cell count on substrate irradiated with low power level.

The higher the power, the lower the absorbance was. The absorbance values and the error bars represent the mean and standard deviation of a triplicate measurements on each sample. Two dominant peaks in the UV-Vis range were considered: 280 and 560 nm. The absorbance peak at the wavelength of 280 nm is related to proteins, in particular aromatic amino acids (tyrosine, tryptophan and phenylalanine) and nucleic acids [234]. On one hand, the increase in absorbance level of the media after cell culture, compared to the reference medium, is an evidence of biochemical activities between cells and the extracellular environment. On the other hand, an increase in the plasma treatment dose results in a decrease in absorbance of the media, indicative of smaller number of unviable cells or lower level of contamination. Indeed, the culture medium is made of proteins, and, proteins that contain a higher percentage of aromatic amino acids have higher absorptivities at 280 nm than those with fewer. Further experiments will address this observation and will provide a deeper qualitative as well as quantitative interpretation of the process, with the support of proteins level of expression.

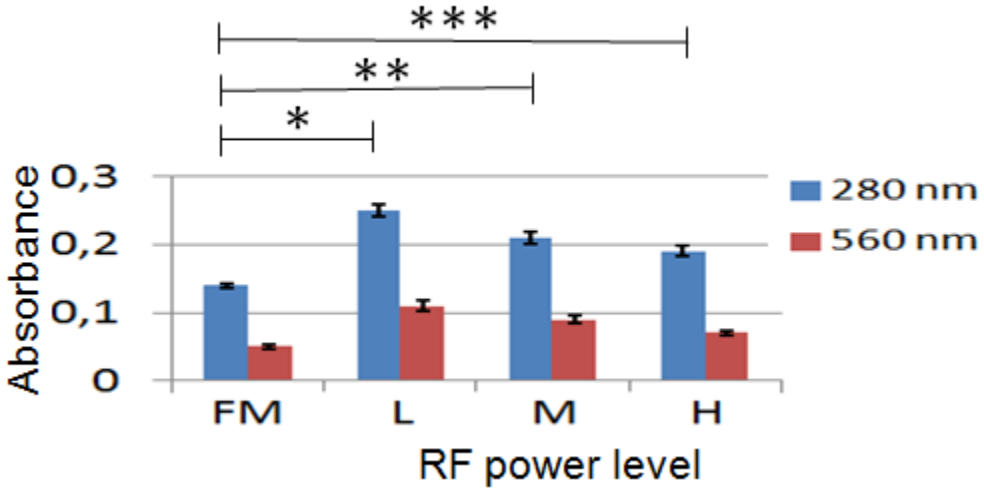

Figure 5-3 Effect of plasma irradiation on the absorbance of the conditioned media. High dose plasma irradiation showed the best result in terms of comparison with FM (*P = 0.0002, **P = 0.0011, ***P = 0.0053).

Figure 5-4 presents the NAC of the fresh medium (reference measurement, FM), and of the cell culture media collected after 48 hours of cultivation on substrates exposed to low dose (L), medium dose (M), and high dose (H) RF power. The absorbance values and the error bars represent the mean and standard deviation of a triplicate measurements on each sample. Once again, media containing a higher concentration of nucleic acid have higher absorptivities than those with fewer. Therefore, this figure shows that an increase in the plasma treatment dose results a decrease in NAC in the medium, indicative of smaller number of unviable cells or lower level of contamination. A similar result is obtained for the effect of plasma irradiation dose on the absorbance of the nucleic acid in the conditioned media (Figure 5-5).

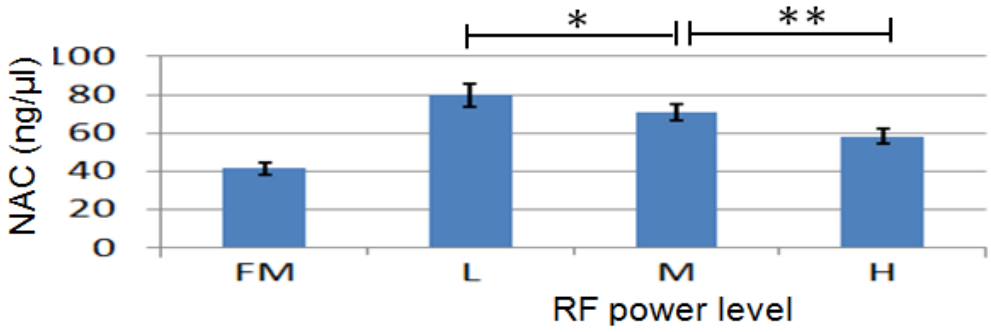

Figure 5-4 Effect of plasma irradiation dose on the nucleic acid concentration of the conditioned media. High dose plasma irradiation showed the best result in terms of less NAC present in the culture medium (*P = 0.0312, **P = 0.0059).

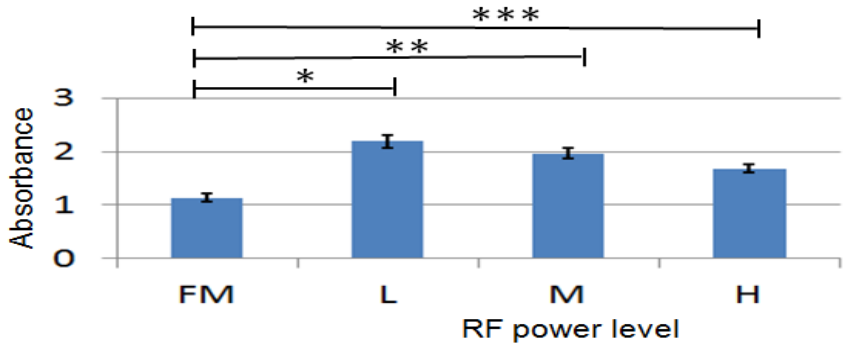

Figure 5-5 Effect of plasma irradiation dose on the absorbance of the nucleic acid of the conditioned. High dose plasma irradiation showed the best result in terms of comparison with FM (*P = 0.0009, **P = 0.0030, ***P = 0.0031).

5.4 Concluding remarks

This rapid communication provides new insight into how spectrophotometry can be noninvasively used toward the understanding of cells response to different environment. The preliminary results in this prompt study on HeLa cells as well as MDA 231 breast cancer cells (data not shown) suggest a fundamental role for mechano-sensing in cells

development, and illustrate that the physico-chemicical environment should be taken into consideration when producing therapeutically relevant *in vitro* cell populations. This study highlights the feasibility of noninvasively monitoring cell proliferation and protein expression with a simple spectroscopic approach. Our hypothesis may offer a quick, low-cost and easy way of quantifying cell numbers (without cells detachment) from proliferation and cytotoxicity studies. Our immediate future goal is to confirm these results with standard biological assays and other cell lines, then establish a comprehensive guideline for using this technique toward a noninvasive cellular analysis and comparative genomics in cellular biology *in vitro*, with minimal consumption of sample. Such a reduction in the volume of sample required for the analysis will also facilitate the inclusion of additional quality control steps throughout the molecular workflow, increasing efficiency and ultimately leading to greater confidence in downstream results.

CHAPTER 6. Elasticity-triggered biological responses of SH-SY5Y neuroblastoma cells in vitro

Presented in this chapter is the effect of PDMS substrate bulk rigidity and surface energy modification on SH-SY5Y neuroblastoma cell line. The approach described shows how mechanical properties of the culture surface can trig cell differentiation, polarization and adhesion. This work is based on an article under review in the journal Biomedical Materials and Engineering [131]. It complements the methods presented in chapters 3, 4 and 5, and covers objective (iii) of the "Thesis objective and scope" in section 1.3.

6.1 Introduction

In the neurosciences many questions exist that center on how ECM affects synaptic and cellular structure. In culture, it is generally believed that using stiffer PDMS substrate leads to a better cell viability [237], still the optimum stiffness is currently undefined. In recent years, it has become desirable and conceptually feasible to study the effects of substrate stiffness on cells in vitro. From these studies has emerged an improved understanding of cell culture on different substrate rigidities. Yet a major need still exists for better for better control of the precise spatial development and geometric interaction of neural cells, both for fundamental studies in vitro and for a variety of focused applications, such as evaluation of pharmaceuticals and development of biosensors. With such cultures it should be possible to determine the type of parameters of change as a function of ECM rigidity and to monitor not only mechanical activity but also metabolic and structural change of neurons.

Many established neuroblastoma cell lines possess at least 3 morphological variants contributing to the heterogeneity in these cell lines: the neuroblastic (N), flat or substrate adherent (S) and intermediate (I) cell types [238-240]. A study of cell surface antigen expression indicated that the S-type cells shared antigenic characteristics more in common with a fibroblast-like meningeal cell rather than a Schwannian cell [241,242]. Meanwhile, neural crest cells can give rise to ectomesenchyme, including skeletal and connective tissues of the head and face which also includes meninges. These features have led to a model in which N-type cells are proposed to resemble embryonic sympathoblasts, S-type cells resemble Schwannian, glial or melanocytic progenitor cells or ectomesenchymal derivatives and the I-type cells have an intermediate phenotype and the potential to differentiate to N- or S-type cells [240].

Ultimately we want to develop a basic understanding of the relationships between the developmental morphologies of cultured neurons and the quantitated mechanical characteristics of the substrates. Progress toward a quantitative understanding of the role of the substrate is crucial not only to neuronal patterning but also to the interpretation of experiments involving regulators of cell metabolism in vitro and future applications requiring the rational design of neuronal substrates.

6.2 Materials and methods

6.2.1 Substrate preparation and characterization

The PDMS used in this work is a liquid bi-component silicone pre-polymer, Sylgard 184 manufactured by Dow Corning (Midland, MI). The substrate stiffness can be controlled

by the base (pre-polymer) to hardener (curing agent) ratio, determining the cross-linker agent concentration in the PDMS solution. Other key parameters for manipulating this mechanical property are temperature and curing time. As the time and curing temperature are closely linked, we choose to cure the PDMS substrates at a constant temperature of 75^{o}C for 2 hours. The solutions were mixed in sterile conditions and degassed, then poured into 24 well plates to a depth of about 1 mm. The mixed and degassed solutions were cured at 75^{o}C for 2 hours. The "untreated" dishes with PDMS substrates were rinsed three times in sterile PBS, then once in 100% ethanol during two minutes, and air dried in sterile conditions. The "treated" dishes PDMS substrates were exposed to air plasma for 10 minutes at 29.6 W using a plasma machine (Harrick, model PDC-001), with air entering the chamber at 150 Pa. All plates were then exposed to UV light in the biological safety cabinet for further sterilization, from a transilluminator for 20 minutes from a distance of 30 cm. The substrate's characterization was performed as described in our earlier work [130].

6.2.2 Cell line and low density culture conditions

The SH-SY5Y cell line used is a thrice cloned subline of SK-N-SH cells which were originally established from a bone marrow biopsy of a neuroblastoma patient with sympathetic adrenergic ganglia origin in the early 1970's [241]. Using current culture technology, neurons are usually randomly organized and their dendrites and axons overlap and are. This makes geometrically dependent studies of minor processes in neuron's development extremely difficult, if not impossible. Therefore, we adopt a low density culture for two reasons: (1) it allows driving and monitoring neuronal growth in

response to substrate stiffness changes; (2) it allows correlating the dynamic changes of the cell activity with its topology and substrate mechanical properties.

The culture medium used was a 1:1 mixture of Eagle's minimum essential medium with nonessential amino acids and Ham's nutrient mixture F-12, supplemented with 15% heat-inactivated fetal bovine serum and 1% penicillin-streptomycin. Derived from immature neoplastic neural crest cells that exhibit properties of stem cells, SH-SY5Y were induced to differentiate upon treatment with retinoic acid (RA) [242].

6.2.3 Proliferation and morphological change measurements

Cells were plated at 300 x 10^6 cells/well on plasma treated PDMS substrates. For the assessment of morphological changes, images of cells growing on each substrate were captured using an inverted phase contrast microscope equipped with a controller software. Eight to ten distinct snapshots of representative areas of each well were examined with the freeware ImageJ software (available at http://rsb.info.nih.gov/ij). Single cells were identified by their boundaries and the approximate perimeter measured by tracing the border of five cells per image and using the "Perimeter" function in ImageJ.

For adhesion analysis, 20 and 60 hours incubated cells were washed twice in PBS, fixed for 15 minutes with 70% (v/v) ethanol to preserve the shape as much as possible, and washed again twice in PBS. After fixation, cells were stained with 0.5% (w/v) crystal violet for 10 minutes and dye was extracted from cells with 0.1M citric acid. Absorbance was measured at 590 nm on an absorbance spectrometer.

6.2.4 Immunofluorescence and adhesion measurement

Cells were stained for F-actin with Alexa Fluor 555 tagged phalloidin (Invitrogen), for nuclei with ProLong Gold antifade reagent with 4',6-diamidino-2-phenylindole (DAPI) (Invitrogen), and for vinculin to mark focal adhesions with monoclonal anti-vinculin-FITC antibodies (Sigma-Aldrich). The cells, on PDMS substrate, were first fixed with 3.7% formaldehyde (Polysciences Inc), and permeabilized with 0.1% Triton X-100 (Astoria-Pacific). Then they were stained and the antifade reagent was added before cover slips were placed over the cells and sealed with nail polish.

6.3 Results and discussion

Figure 6-1 shows the average counted undifferentiated cells on different substrates. These cells being known to grow as a mixture of floating and adherent cells, 300 x 10^6 cells were initially plated and only adherent cells were counted. The cell proliferation trend observed here complies with that of elasticity measurement of the substrate. Error bars represent the measured standard deviation in each set of data and each data point represents means ± S.D. of 8-10 determinations. The experiment was performed in triplicate.

Figure 6-2 shows the average percentage of non-viable undifferentiated cells on different substrates. Only cells presenting no minor process were counted. A minor process was explicitly chosen to be related to the neuritic outgrowth or the branching. The trend observed reflects cells viability and complies with that of the rigidity measurement of the substrate. Error bars here also represent the measured standard deviation in each set of

data and each data point represents means ± S.D. of 8-10 determinations. The experiment was performed in triplicate.

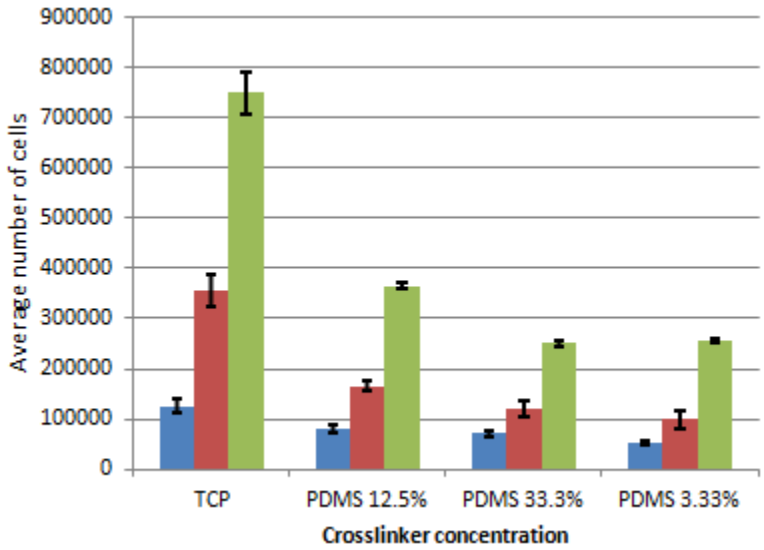

Figure 6-1 Undifferentiated neuroblastoma cell culture on substrates with different mechanical properties.

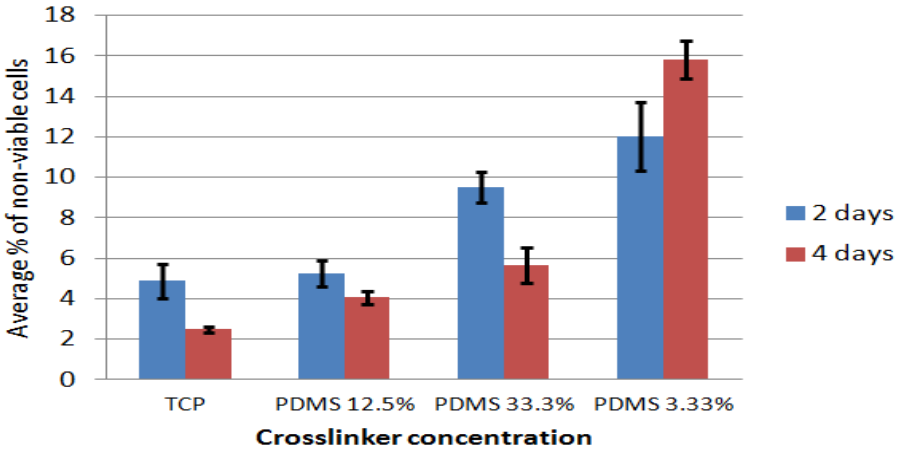

Figure 6-2 Non-viable undifferentiated neuroblastoma cells on substrates with different mechanical properties.

Figures 6-1 and 6-2 reveal that, compared to standard tissue culture dish, PDMS with 12.5% crosslinker concentration is proved to be an optimal substrate for neuroblastoma culture on functionalized (plasma treated) PDMS, under the conditions used in this study. This is in good agreement with the observation made with cervical cancer cell line, HeLa, in our previous work [130]. Figure 6-3 shows typical phase-contrast images of undifferentiated SH-SY5Y neuroblastoma cells on TCP and PDMS after 2 and 4 days in culture, showing that the majority of the cells do not display formation of a single dominant process, evidencing development of axonal/dendritic polarity.

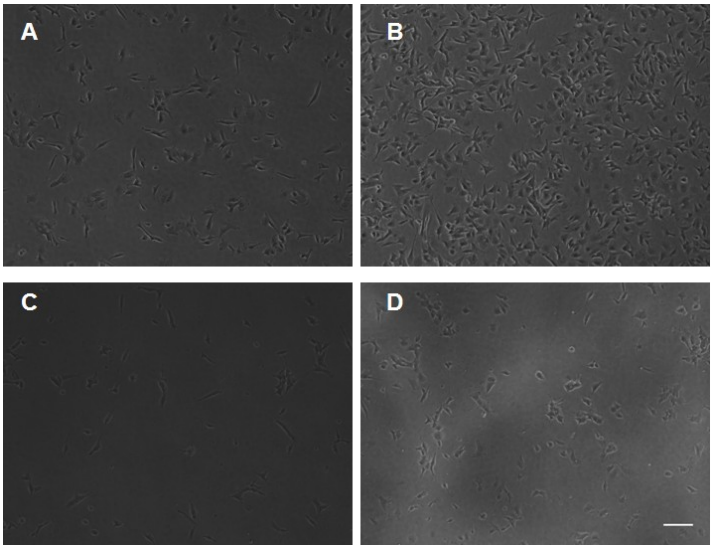

Figure 6-3 Phase-contrast images of undifferentiated SH-SY5Y neuroblastoma cellson TCP (A,B) and PDMS with 12.5% crosslinker concentration (C,D) after 2 days (A,C) and 4 days (B,D) in culture. The scale bar in panel D corresponds to 100 μm.

Upon differentiation with RA, cells stop proliferating, become a stable population, and show extensive neurite outgrowth [243]. Figure 6-4 shows typical phase-contrast images of RA-differentiated SH-SY5Y neuroblastoma cells plated on polystyrene tissue culture

plastic and PDMS substrate. The dendrites and axons overlap extensively and remain undefined, which makes cells' response to changes in substrate stiffness investigation difficult at a single cell level. As a consequence, a low density culture is adopted in our study.

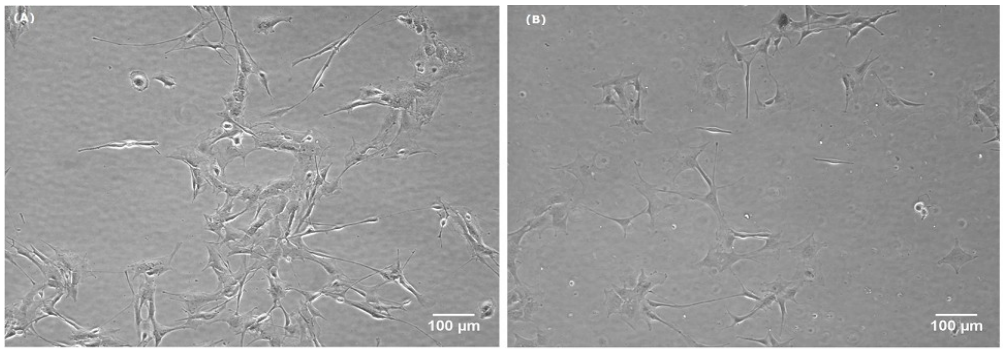

Figure 6-4 Typical phase-contrast images of RA-differentiated SH-SY5Y neuroblastomacells plated on polystyrene tissue culture plastic (A) and PDMS substrate with 12.5% of cross linker concentration (B). The random distribution of the soma and neuritic processes is clearly illustrated.

In Figure 6-5, phase-contrast images of RA-differentiated SH-SY5Y neuroblastoma cells on TCP and PDMS at 4 and 8 days in culture are presented. We observe that many cells exhibit a primary neurite having a length above 100 µm at day #8. The cell bodies are large and well adhered to the substrate and neurite outgrowth is indicative of a developing axonal/dendritic geometric polarity.

Figure 6-6 shows representative fluorescence images of RA-differentiated SH-SY5Y cultured on PDMS with 3.33%, 12.5%, and 33.3% crosslinker concentration. Cells were stained with antivinculin antibodies to mark focal adhesions (Green) and DAPI for nuclei

labelling (Blue). The figure also illustrate the approach used for counting focal adhesion points. A white square in each panel represents a region of interest on a neurite. A zoomed view of the corresponding regions of interest is reported as inset in the upper right corner of each panel. White arrowheads in the inset point to the visible focal adhesions.

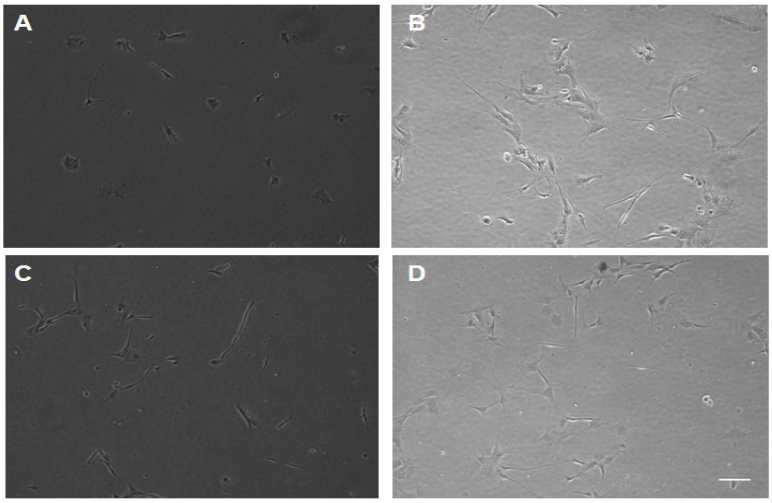

Figure 6-5 Phase-contrast images of RA-differentiated SH-SY5Y neuroblastoma cells on TCP (A,B) and PDMS with12.5% crosslinker concentration (C,D) after 4 days (A,C) and 8 days (B,D) in culture. The scale bar in panel D corresponds to 100 μm.

Evidences of the effect of substrate stiffness on cell adhesion and differentiation are shown in Figure 6-7 below. Figure 6-7(A) shows the average measured length of neurites on different substrate rigidities on day #8 in culture. 96 cells from three experiments were analyzed for the calculations in each group. The average neurite length is shown to decrease with an increase in the substrate rigidity. Figure 6-7(B) presents the average number of focal adhesions on substrates of different rigidity. 40 cells from three experiments were analyzed for the calculations in each group and the average neurite

length also decreases with an increase in the substrate rigidity. Figure 6-7(C) presents the average percentage of cells with responsive Focal Adhesion Kinase (FAK). A responsive cell was defined as a cell having at least 3 focal adhesion points. Here again, 40 cells from three experiments were analyzed for the calculations in each group and the number of responsive cells decreases with an increase in the substrate rigidity. Finally, Figure 6-7(D) shows a classification of focal adhesions by size and by group. Focal adhesion sizes were defined as small (less than 2 µm²), medium (between 2 and 4 µm²), and large (more than 4 µm²). 680 focal adhesions were analyzed and we observe a predominance of large focal adhesions in all cases, with the larger of the stiffer substrate (PDMS 12.5%). These observations are in good agreement with the results reported by Lo et al. [244] on fibroblasts.

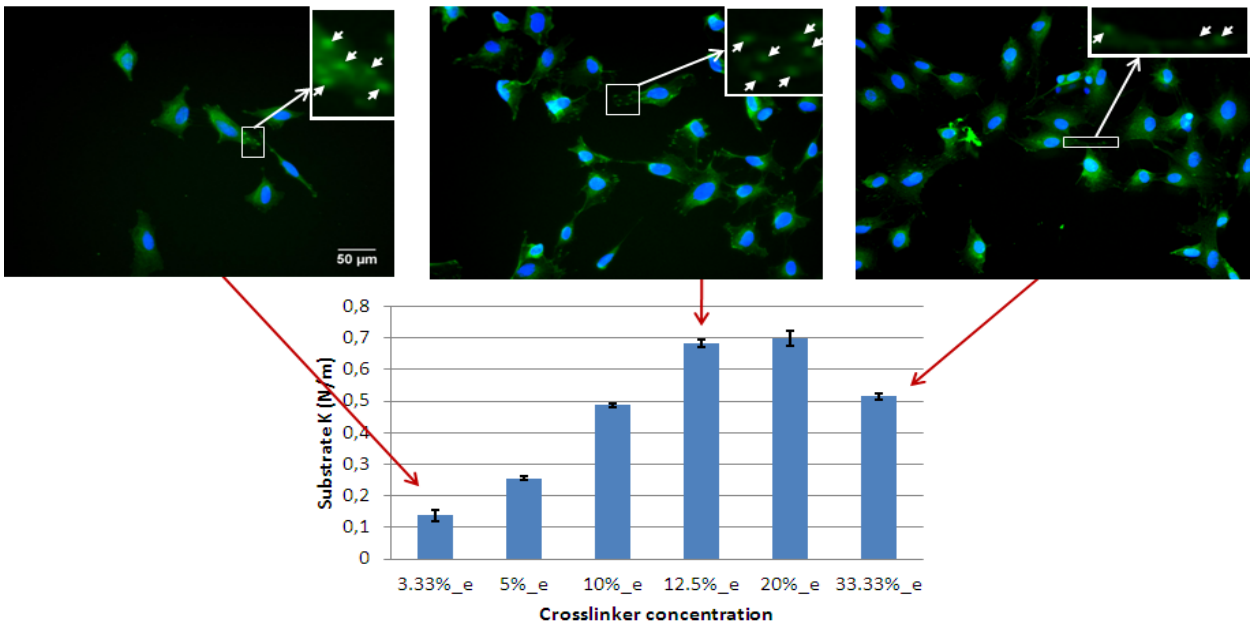

Figure 6-6 Representative fluorescence images of RA-differentiated SH-SY5Yon day #8, cultured on PDMS with 3.33% (left), 12.5% (middle), and 33.3% (right) crosslinker concentration.

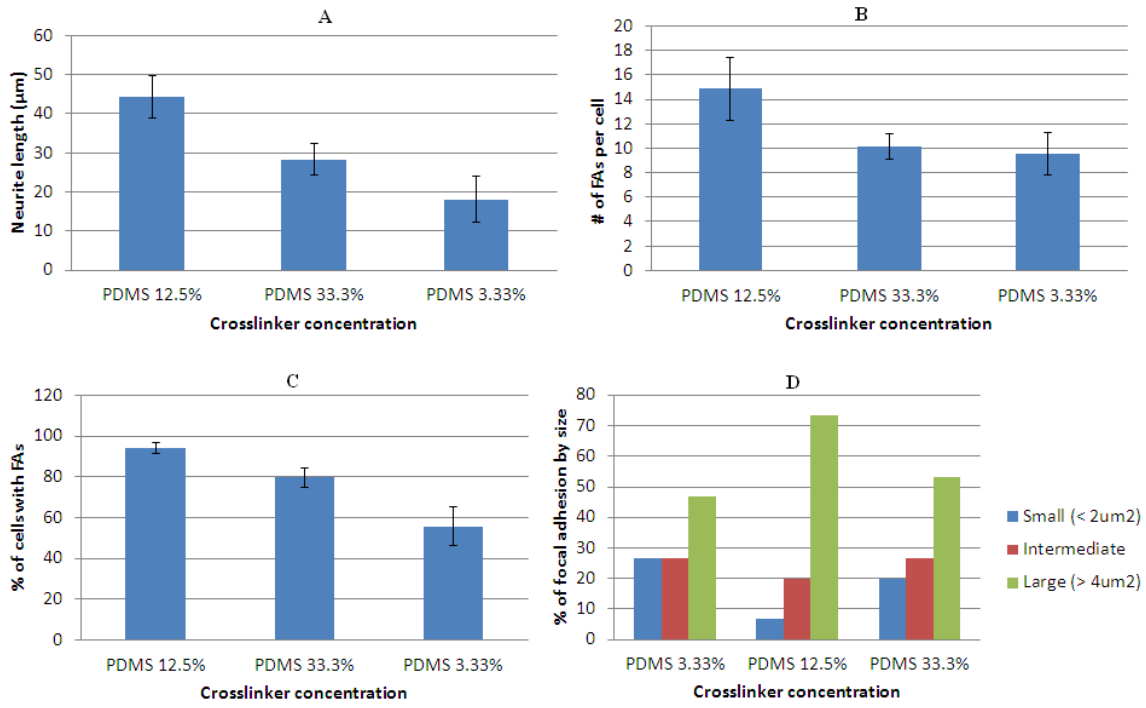

Figure 6-7 Cell adhesion and differentiation as a function of substrate stiffness on day #8 in culture. (A) Length of neurites. 96 cells from three experiments were analyzed for the calculations in each group. (B) Number of focal adhesions. 40 cells from three experiments were analyzed for the calculations in each group. (C) Cells with responsive Focal Adhesion Kinase (FAK). 40 cells from three experiments were analyzed for the calculations in each group. (D) Focal adhesion classified by size. In all cases, error bars represent the measured standard deviation in each set of data.

Comparative results were obtained by Brunetti et al. [244], who seeded SH-SY5Y cells onto micro patterned flat and nanorough gold surfaces; they demonstrated the possibility to realize substrates with cytophilic or cytophobic behavior, by fine-tuning their surface topography at nanometer scale. They observed specific and functional adhesion of cells only onto flat gold stripes, with a clear self-alignment (polarization) of neurons, yielding

a simple approach for the design and development of biomaterials with precise nanostructure-triggered biological responses.

Overall, an advantage of PDMS substrate for cell culture is the reproducible composition and properties associated with the fabrication process. This is in marked contrast to surfaces modified with biologically derived materials such as proteins or membranes[245,246], for which the starting materials may not be well-characterized, and their conformation can vary and have profound effects on the structure at the interface. This limitation makes interpretation of effects difficult, and can lead to problems of reproducibility, which is overcome in our study. Consequently, our study effectively supports the hypothesis that mechanical factors impact cells in fundamentally different ways, and can trigger specific changes similar to those stimulated by soluble ligands. This is in good agreement with previous works reported in the literature [247,248].

6.4 Concluding remarks

This work shows that modifying PDMS cross-linker concentration to tune substrate rigidity plays a role in neuroblastoma adhesiveness and development of axonal/dendritic polarity. A correlation between higher PDMS surface energy (hydrophilicy), higher cell adhesion, higher cell surface, and larger cell polarization has been found. Indeed, an increase in the substrate's stiffness highly favors cell adhesion, which is correlated with significantly more polarized cells. Moreover, stiffer substrates promote significantly faster neurite extension than softer ones, and there is a high compliance of undifferentiated cell proliferation rate with substrate's stiffness variation. Thus the results

show that adequate tuning of the substrate mechanical properties and surfaces physical chemistry can control the neuroblastoma cells adhesion and morphology.

CHAPTER 7. Modal parameters estimation of an early avian embryo model organs considered cell aggregates

Mechanical forces play an important role during early embryo development. Although physical and mechanical properties of organs are available in the literature for different stages of growing chick embryos, the modal parameters of each organ remain largely unknown. A simplified model of 4 degrees-of-freedom (DOF) mass-spring-damper (MKC) system made of the body (limb), the liver, the heart and the brain is considered in this paper. A data set of material parameters corresponding to a stage 14 chicken embryo development is obtained from the literature. An eigenvalue solution approach using frequency response function matrices is applied to study the mechanical vibrations of the system. We demonstrate that the exact modal parameters of the chick embryo model can be obtained using both the Mode Indicator Functions (MIF) and a least squares approach using the Prony method, even when the mechanical excitation cannot be controlled. These estimators are presented as a promising modal indicator and parameter estimation technique, contributing to limit the cost of experiments at such a small scale as in the investigation of embryo development. Therefore, our study can help illuminating the mechanical vibration analysis of incubated eggs and its relation to embryogenesis. This is important for the understanding of the dynamics of morphogenetic processes, the biomechanics of tissues, the design of implantable medical devices and the biomaterials used in their fabrication.

7.1 Introduction

Vibration exposure standards for pregnant women and their developing foetuses have not been established. This is a highly complex issue due to the extreme lack of data on the subject. As a step forward to clarify this issue, it requires epidemiologic and basic scientific studies to explore the feasibility of developing an avian model with the aim of studying the relationship of vibration to discernable organs in a developing embryo. A survey of animal studies in the literature indicated a possible harmful effect of vibration upon embryologic development [249-251].

Based on an experimental modal analysis, the dynamic behaviour of a chicken egg was characterized [252-254]. While these works were focused on the study of the mechanical vibrations as an indicator of egg and egg shell quality, little is known on the contributing effect and the impact of external mechanical vibrations on each developing organ. To address this issue, we adopted a simplified model of discretized stage 14 chicken embryo made of limb (or simply the body), liver, heart and brain, consistent with early morphogenesis [255].

The present study was intended to show the feasibility of a modal parameters extraction approach toward a better understanding of the vibration in the early stage of embryogenesis. For this purpose, the modal analysis technique was used. This technique refers to an experimental or analytical procedure applied in vibration analysis for describing the dynamic behaviour of mechanical systems [256]. In this work, the governing equations were formed by obtaining mass (M), stiffness (K) and damping (C) matrices. The system equation was analytically solved, the frequency response functions

(FRFs) obtained, and the modal parameters extracted from the FRFs. The MIFs as well as the Prony methods were then performed and correlated with the analytical solution obtained by solving the eigenvalue problem. This approach could lead to a better understanding of the effect of a random vibration excitation on specific organs in early chicken embryo, which is nowadays still an unknown in normal embryo development failure.

7.2 Modal parameter extraction and validation

7.2.1 Model description: the chick embryo system

The chick embryo, subject of our study, occupies a unique position among higher vertebrates in that it provides an excellent model to investigate the normal development of the embryo especially in the early stage. Indeed, all of the developing chicken embryo requirements, except oxygen and heat, are provided by the egg contents. As a physical matter, the embryo is a continuous and complex system and have an infinite number of DOF (modes). However, only a finite number of modes can be used to describe the dynamic behaviour of a system, and we have chosen to model a 12 days old chick embryo, which corresponds to the stage in which main organs (brain, heart, liver and limbs) are formed.

In this study, a simplified version of the multi-DOF system presented by Fuellekrug [257] was considered. This model consists of the four main organs listed above, and linked to each other in the following geographical order: brain, heart, liver and limbs (also assumed the rest of the body). The system is assumed passive and therefore, organs are

simply linked as shown in Figure 7-1. Neglecting other connections means that the validity of the results is limited to the cases where there is not much change in the stiffness of these connections, which is the case in our study (the albumen).

The physical parameters of the system, except the brain, were obtained from Forgacs et al. [258], Haba et al. [259] and Xu et al. [260], and summarized in table 7-1, whereas, the damping value of the brain tissue was fixed, and its stiffness was obtained as described in section 7.3 below.

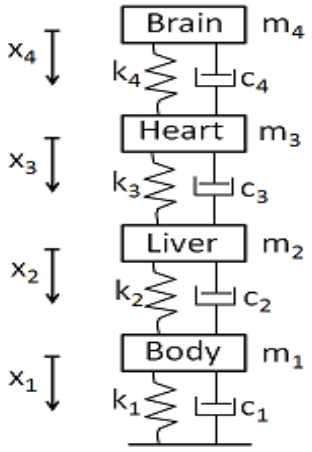

Figure 7-1 An 4-DOF lumped mass vibration system

Table 7-1 Physical parameters of the ideal lumped elements.

Parameters	Body	Liver	Heart	Brain
Mass m_i (g)	10	0.3	0.1	0.4
Stiffness k_i (N/m)	0.0086	0.004	0.0051	0.00005
Damping c_i (Ns/m)	0.0235	0.0073	0.0095	-

7.2.2 The Mode Indicator Function (MIF)

This estimator assists in the selection of poles during the extraction process and was formulated here to provide a better way for identifying closely spaced modes. In the MIF approach, the real part of the FRF is divided by its magnitude. Because the real part rapidly passes through zero at resonance, the MIF usually tends to have a much more abrupt change across a mode. The real part of the FRF will be zero at resonance and therefore the MIF will drop to a minimum in the region of a mode [261].

The MIF is formulated here and computed as follows:

$$MIF1 = \frac{\sum_i \left| \mathrm{Im}(H_i) \right|}{\sum_i \left| H_i \right|} \tag{7.1}$$

The peaks detected in the MIF plot indicate the existence of modes, and the located frequencies give the corresponding damped resonance frequencies.

7.2.3 Least square estimation

For the purpose of our analysis, a routine is implemented to find the poles from a unit impulse response. This routine helps separating physical poles from mathematical ones.

The transfer function of a system can be written in a pole-residue form (modal model) as [267]:

$$H(s) = \sum_{r=1}^{n} \frac{A_r}{s-\lambda_r} + \frac{A_r^*}{s-\lambda_r^*} \tag{7.2}$$

The residue matrices A_r, $r = 1, \ldots, n$, are defined by:

$$A_r = \lim_{s \to \lambda_r} H\ s\ (s - \lambda_r) \tag{7.3}$$

One can easily show that the matrix A_r is of rank one, meaning that A_r can be decomposed as:

$$A_r = \Psi_r \Psi_r^T = \begin{matrix} \psi_r(1) \\ \psi_r(2) \\ \vdots \\ \psi_r(n) \end{matrix} \quad \psi_r(1) \quad \psi_r(2) \quad \ldots \quad \psi_r(n) \tag{7.4}$$

with Ψ_r a vector representing the mode shape of mode *r*. From Eq. (7.2), it appears that the transfer function matrix of the system is the sum of all contributing single DOF transfer functions, obeying to the principle of modal superposition [262]. The full transfer function matrix is completely characterized by the modal parameters, i.e. the poles λ_r and the mode shape vectors Ψ_r.

Taking the inverse Laplace transform of Eq. (7.2) yields the following impulse response function

$$h\ t\ = \ {}_{r=1}^{n} A_r e^{\lambda_r t} + A_r^* e^{\lambda_r^* t} \tag{7.5}$$

which consists of a sum of complex exponential functions.

The poles are then obtained using the least squares complex exponential approach formulated, and a stability diagram is plotted by repeating the analysis for increasing model order number. The stable poles can graphically be presented in ascending model

order. The estimated poles corresponding to physically relevant system modes tend to appear at nearly identical locations for each estimation order. On the other hand, poles resulting from the mathematical solution of the normal equations but meaningless with respect to the physical interpretation, mainly due to the presence of noise, tend to jump around. Given the poles, the residues are finally calculated from the impulse response with a least squares routine, assuming that the impulse response corresponds to a mobility FRF as in Eq. (7.18) below.

7.2.4 Modal validation

Once the modal parameters are determined, several procedures exist allowing validation of the modal model. For this purpose, we are using the modal vector orthogonality.

For an undamped or a proportionally damped system, the coordinate transformation diagonalizes the system mass, damping and stiffness matrices. In the case of modal vectors, the orthogonality properties are given by:

$$\psi_{-}[M]\psi_{-}=[M]_{-} \tag{7.6}$$

and

$$\psi_{-}[K]\psi_{-}=[K]_{-} \tag{7.7}$$

where ψ_{-} is the modal matrix. If the damping matrix is proportional to the mass and/or stiffness matrix, it can be diagonalized as follows:

$$[C] = \alpha [M] + \beta [K] \tag{7.8}$$

The application of orthogonality condition yields

$$\psi^T [C] \psi = \alpha [M] + \beta [K] \tag{7.9}$$

Therefore

$$\psi^T [C] \psi = [C] \tag{7.10}$$

where C is a diagonal matrix.

7.3 Theoretical Background and forward problem

7.3.1 Basics and hypotheses

The experimental modal analysis for obtaining the dynamic behavior of a system has been extensively discussed in the literature [254,263-265]. In this field, the system can be modelled using idealized mechanical elements with lumped constants. The simplicity and transparency of this method are determined by postulating four conditions for the structure under investigation [262]:

(1) The mechanical system is linear; so the principle of superposition applies.

(2) The mechanical system is time invariant.

(3) The system is observable, so the measured outputs must yield sufficient information to construct a reliable mathematical model.

(4) Maxwell's reciprocity principle should apply, meaning that the measurement and excitation points are interchangeable.

7.3.2 Governing equations and analytical solution

The physical system to be studied is comprised of an interconnection of idealized single DOF models, as illustrated in Figure 7-1. Governing equations on the behaviour of this system with 4 DOF and damping are given by [266]:

$$[M]\ddot{x} + [C]\dot{x} + [K]x = F \tag{7.11}$$

where M is the mass matrix, C is viscous damping matrix, K is stiffness matrix, X is the system-response vector in specified degrees of freedom, and F is the external applied force vector.

The Laplace transform of Eq. (7.11) can be written as:

$$(Ms^2 + Cs + K)X(s) = F(t) \tag{7.12}$$

The equations of motion of the system are derived from Eq. (7.11) and yield the following matrices:

$$M=\begin{bmatrix} m1 & 0 & 0 & 0 \\ 0 & m2 & 0 & 0 \\ 0 & 0 & m3 & 0 \\ 0 & 0 & 0 & m4 \end{bmatrix} K=\begin{bmatrix} (k_1+k_2) & -k_2 & 0 & 0 \\ -k_2 & (k_2+k_3) & -k_3 & 0 \\ 0 & -k_3 & (k_3+k_4) & -k_4 \\ 0 & 0 & -k_4 & k_4 \end{bmatrix} C=\begin{bmatrix} (c_1+c_2) & -c_2 & 0 & 0 \\ -c_2 & (c_2+c_3) & -c_3 & 0 \\ 0 & -c_3 & (c_3+c_4) & -c_4 \\ 0 & 0 & -c_4 & c_4 \end{bmatrix} \tag{7.13}$$

The undamped resonance frequencies are determined by setting *C=0* and *F=0*, and Eq. (7.2) becomes:

$$(Ms^2 + K)X(s) = 0 \qquad (7.14)$$

Pre-multiplying Eq. (7.14) by M^{-1}, then by K^{-1} gives:

$$[M][K] + s^2[I] = 0 \qquad (7.15)$$

and

$$[K][M] + \frac{1}{s^2}[I] = 0 \qquad (7.16)$$

Eq. (7.15) and Eq. (7.16) can be solved by setting their determinants to zero, i.e.,

$$\left|[M][K] + s^2[I]\right| = 0 \qquad (7.17)$$

and

$$\left|[K][M] + \frac{1}{s^2}[I]\right| = 0 \qquad (7.18)$$

s^2 in Eq. (7.15) and Eq. (7.17), and $\frac{1}{s^2}$ in Eq. (7.16) and Eq. (7.18), are the eigenvalues.

7.3.3 The frequency response function solution

When excitation is applied, Eq. (7.12) leads to the frequency response of the system as a complex quantity. The modal model is then fully described by a matrix of frequency response functions $H_{pq}(\omega)$, for which elements may be obtained by calculating the ratio

of the response signal at DOF p, $X_p(\omega)$ to the input signal at DOF q, $F_q(\omega)$ in the frequency domain [267], and expressed as follows:

$$H_{pq}\ \omega\ =\ \sum_{r=1}^{n} \frac{A_{pqr}}{j\omega-\lambda_r}+\frac{A_{pqr}^*}{j\omega-\lambda_r^*} \tag{7.19}$$

where ω is the frequency variable;

p is the measured response DOF;

q is the measured input DOF;

r is the modal vector number;

λ_r is the system pole;

n is the number of modal frequencies;

A_{pqr} is the residue.

The residue is expressed as:

$$A_{pqr} = Q_r \psi_{pr} \psi_{qr} \tag{7.20}$$

with Q being the modal scaling factor and ψ the modal coefficient.

In the formulation of Eq. (7.10), the residue is the product of the modal deformations at the input q and response p DOF and a modal scaling factor for mode r. As such, the

product of these three terms is unique, but each of the three terms individually is not unique.

7.4 Experimental determination of brain elasticity/stiffness

7.4.1 Samples

Fertile brown Leghorn chicken eggs (Couvoir Simetin, Mirabel, QC) were incubated at 38^{o}C for 21 days to monitor its elasticity. Every three days embryo were extracted from the eggs using Whatman filter paper rings [268], dissected with scissors and washed in phosphate-buffered saline (PBS) solution at room temperature. The dissections showed that surrounding head mesenchyme can be present and affect the mechanical property assessment. Hence, most of the additional tissues were removed from the brain using sharp metallic tweezers.

7.4.2 Hydrogel preparation

Gelatin gel from porcine skin (Sigma-Aldrich, St. Louis, MO) samples were constructed to act as surrounding medium for an inclusion made of a brain cell aggregate. For the purpose, distilled water was heated at a temperature between 80 and 90^{o}C. Gelatin powder was next poured into water and continuously stirred to insure regular mixing. When the solution was cooled at 50^{o}C, agar powder (Sigma-Aldrich, St. Louis, MO) was added into the solution and mixing continued until a temperature of 22^{o}C was reached. Molten gel was poured into a mold, and cylindrical inclusion was introduced just prior to gelation. After gelation (3 to 4 hours), the inclusion was smoothly removed and replaced by the brain tissue extracted from chick embryo. An elasticity map of a cross-sectional

area including brain tissue was then performed using an ultrasound scanner (Aixplorer, Aix-en-Provence, France). Figure 7-2 illustrates the phantom gel and the positioning of the ultrasonic probe.

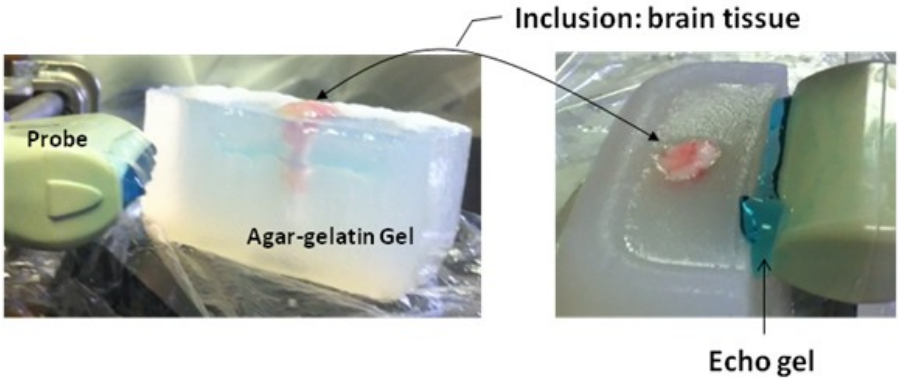

Figure 7-2 Experimental arrangement for measuring chick embryo's brain elasticity.

7.4.3 Elasticity and stiffness values

The setup presented in the previous section allowed to obtain an increase in elasticity within brain tissue as illustrated in Figure 7-3. The measurements were made in triplicate and the error bars represent the Mean ± Standard Deviation of 5 to 8 different sections along the cylindrical inclusion.

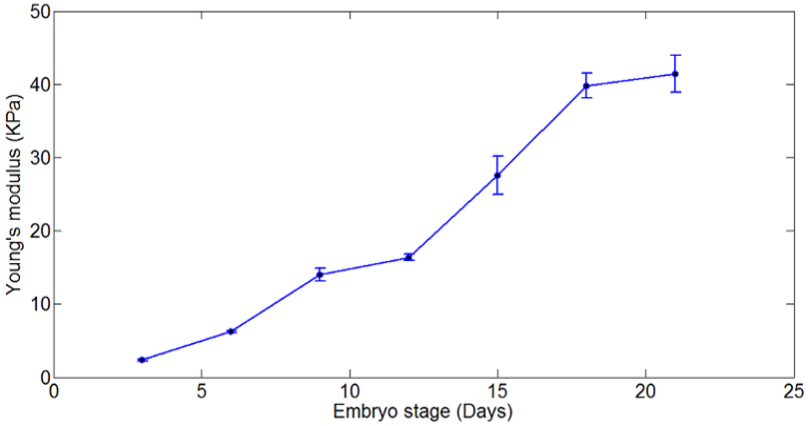

Figure 7-3 Evolution of chick embryo's brain elasticity over 21 days.

The stiffness of the brain tissue can then be obtained at each stage by [269]:

$$k = 6\pi a\mu, \qquad (7.21)$$

where μ, with the SI units Pa, approximates the shear elasticity, and a is the radius of the inclusion. A rough approximation of a purely elastic medium at atomic level yields the brain stiffness value reported in table 7-1.

7.5 Results and discussions

By solving Eq. (7.17) and Eq. (7.18) using the physical parameters reported in table 7-1, the undamped resonance frequencies of the system are obtained and summarized in table 7-2. The same results are obtained by both inversing the stiffness (*K)* and mass (*M) matrices*.

Table 7-2 Eigen frequencies in Hz obtained by successively inversing K and M.

Brain	Limbs	Liver	Heart
0.0555	0.1451	0.5042	1.3526

The FRF of the damped system for different combinations of input and output DOF are illustrated in Figure 7-2 (driving point mobilities) and Figure 7-3 (transfer mobilities). Function H_{pq} is the ratio of the response signal at DOF p, X_p to the input signal at DOF q, F_q in the frequency domain. We note that the addition of damping did not affect the undamped natural frequencies for all modal vectors. This is always the case and would

yield an estimation of the resonance frequencies of chicken embryo organs using lesser physical parameters, thus reducing uncertainties caused by the complexity of estimating the damping of biological samples.

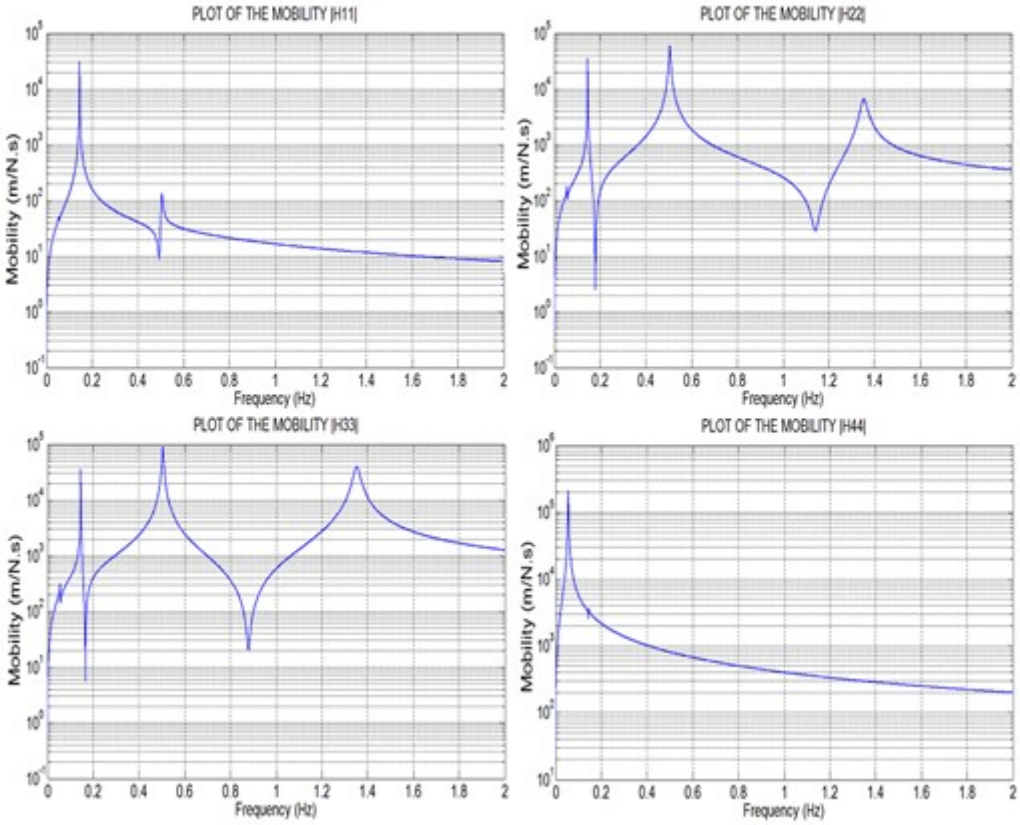

Figure 7-4 FRF of all 4 driving point mobilities. H_{ii} is the ratio of the response signal at DOF i, $X_i(\omega)$ to the input signal at the same DOF i, $F_i(\omega)$ in the frequency domain.

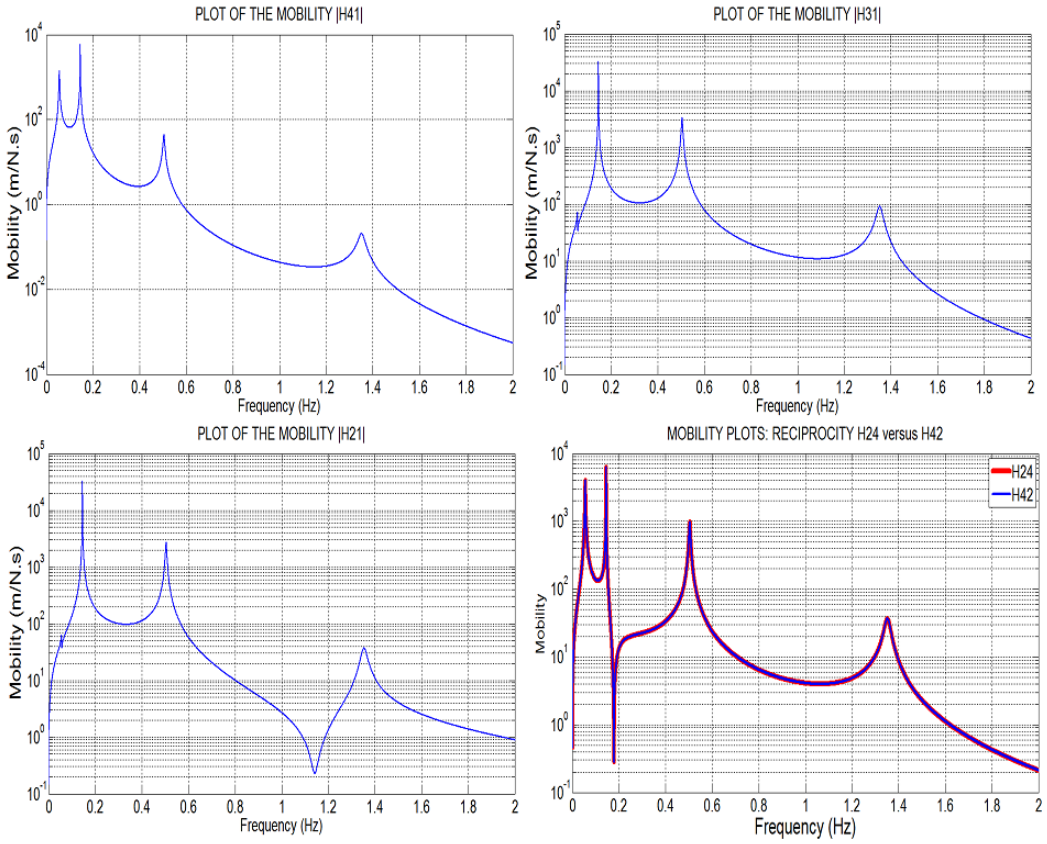

Figure 7-5 Combinations of frequency response transfer mobilities. H_{ij} is the ratio of the response signal at DOF i, $X_i(\omega)$ to the input signal at DOF j, $F_j(\omega)$ in the frequency domain. The bottom-right plot illustrates the Maxwell's reciprocity principle stating that the measurement

It appears from Figure 7-2 and Figure 7-3 above that using only one FRF, it may be difficult to identify how many modes exist. Indeed, all of the modes may not be active in the particular FRF calculated. This is particularly true in our results, as seen in the plots, for the measurements not involving the brain (subscript 4), because of its very high compliance, compared to other organs.

The resonant frequency values obtained here are within the range of those obtained from chicken eggs exposed to different vibration frequencies and amplitudes [250]; the authors observed that the resonance frequency of the egg yolk was 1 Hz, with no motion observed below 0.6 Hz and above 1.7 Hz. However, one should be careful comparing this result with our model, which uses a deeper discretization of the fertilized egg content.

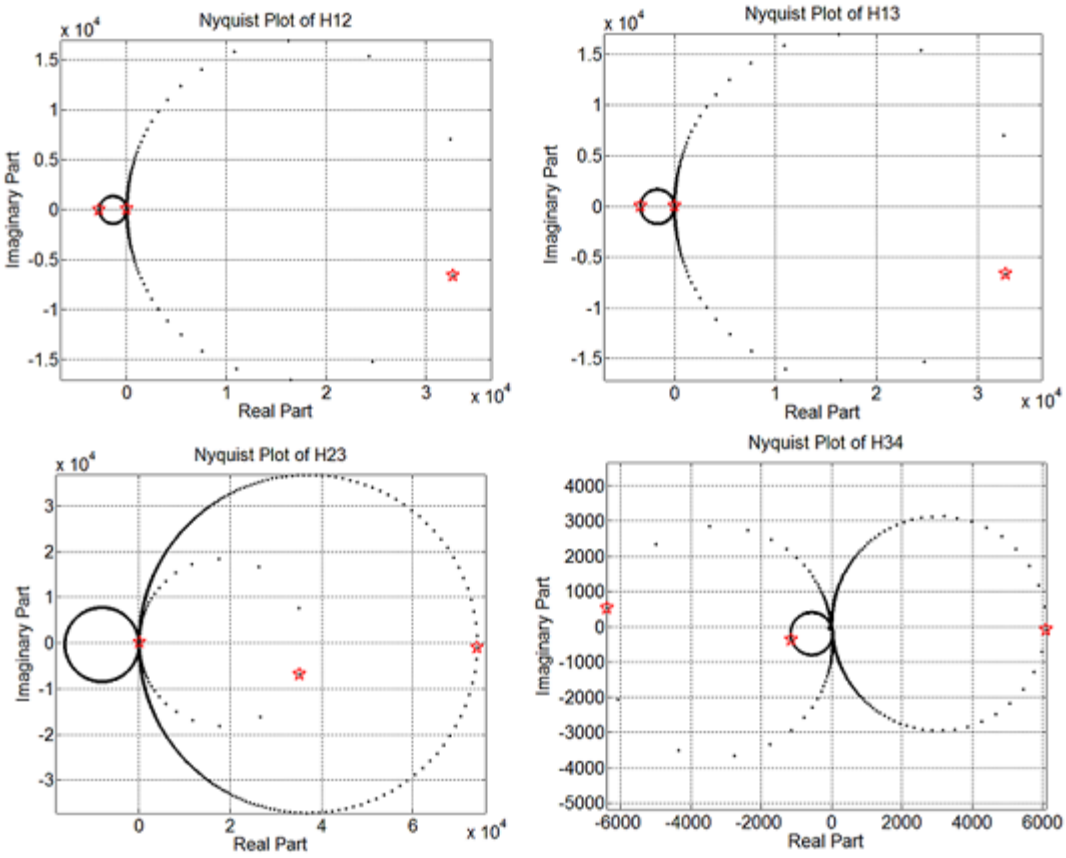

Figure 7-6 Nyquist plots of different combinations of input and output DOF. We get perfect circles (illustrating a stable system), each of them corresponding to one resonance frequency (marked with an asterisk). H_{ij} is the ratio of the response signal at DOF i, $X_i(\omega)$ to the input signal at DOF j, $F_j(\omega)$ in the frequency domain.

Plots of the real part versus the imaginary part for different combinations of input and output DOF are illustrated in Figure 7-4. The results emphasize the area of frequency response at resonance and trace out perfect circles, consistent with Kennedy et al. [270]. As already observed on the FRF, only one Nyquist plot may not allow to observe all of the modes.

The Mode Indicator Functions (MIF), computed from Eq. (7.1), are presented in Figure 7-5 for the four masses with different driving points. The existence of modes of vibration is clearly indicated by distinct peaks and these peaks locations indicate the corresponding resonance frequencies. These resonance frequency values correlate well with the ones in table 7-2.

The modal parameters extraction described in section 7.5.2 above was implemented in MATLAB and Figure 7-6 presents a stability diagram as well as a good fitting of the least squares routine to the data obtained by solving the eigenvalue problem. With a sampling frequency of 13.5 Hz (at least 10 times the highest frequency component), we have used 1024 points of the unit impulse of H_{42} to find the poles. A random noise was added to the impulse response before starting the routine, in order to avoid rank deficiency in the computation. Table 7-3 presents the estimated poles and residues, compared with those obtained analytically from the system matrices M, C, and K in Eq. (7.13). The poles appear to be exactly the same, but the residues slightly differ.

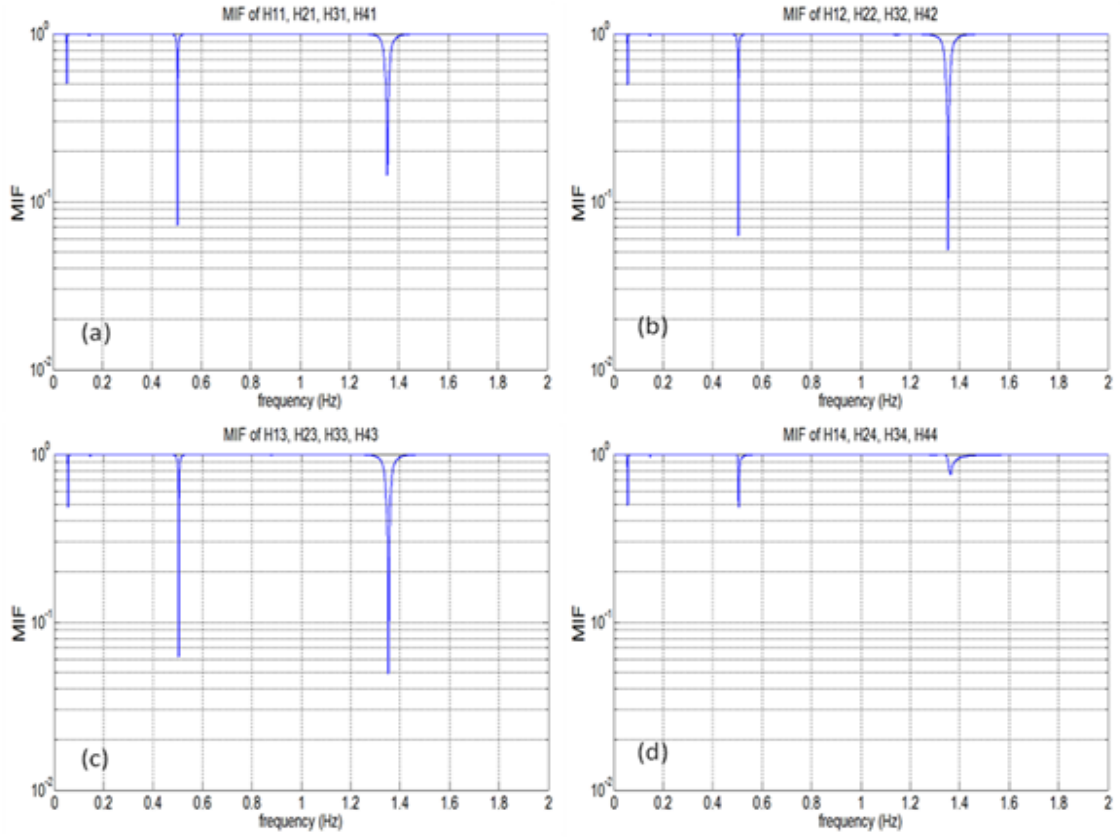

Figure 7-7 MIF plots of the four masses with: (a) the body as the driving point; (b) the liver as the driving point; (c) the heart as the driving point; (d) the brain as the driving point. Note: H_{ij} is the ratio of the response signal at DOF i, $X_i(\omega)$ to the input signal at DOF j, $F_j(\omega)$ in the frequency domain.

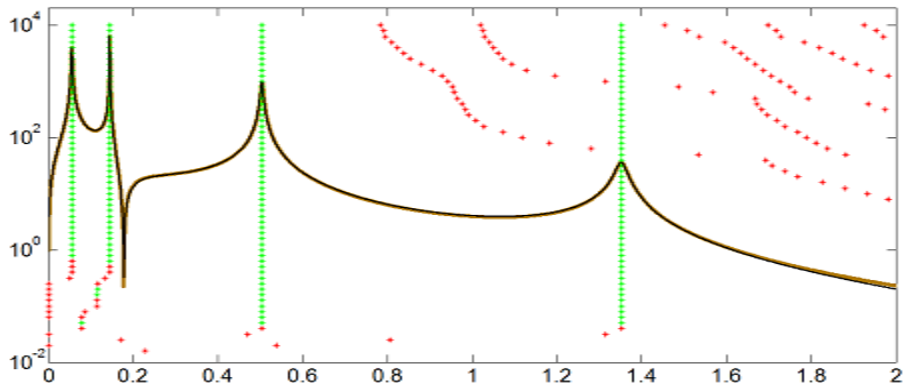

Figure 7-8 Typical stability diagram obtained from the transfer mobilityH_{42} and curve fitting. The implemented Prony estimation routine applied to a transient signal fits the data obtained from solving the eigenvalue problem.

Table 7-3 Comparison of H42 estimated poles and residues by the Prony method. The poles are exactly the same, but the residues slightly differ.

Mode	***Prony estimation (least squares)***		***Resonance method (analytical)***	
	Poles	*Residues*	*Poles*	*Residues*
1	-0.0059+0.3484i	2.4360-68.4428i	-0.0059+0.3484i	2.4358-68.4460i
2	-0.0015+0.9114i	-1.0628+10.7251i	-0.0015+0.9114i	-1.0632+10.7291i
3	-0.0176+3.1677i	-1.5948+5.1661i	-0.0176+3.1677i	-1.6024+5.1898i
4	-0.0838+8.4984i	0.2221-0.2706i	-0.0838+8.4984i	0.2298-0.2795i

Our model can further be validated by checking the modal vector orthogonality. Assuming a proportionally damped system by $C=0.003*K$, we may calculate the diagonalized mass and stiffness matrices with the formulation from Eq. (7.6) and Eq. (7.7). For the original system, the matrices are:

$$M =$$

$$\begin{matrix} 4*10^{-4} & -2.03*10^{-7}+5.81*10^{-6}i & -5.15*10^{-8}+1.3*10^{-6}i & 2.47*10^{-8}-5.41*10^{-7}i \\ -2.03*10^{-7}+5.81*10^{-6}i & 31*10^{-4} & 1.60*10^{-8}+1.13*10^{-6} & -8.89*10^{-9}-4.16*10^{-7}i \\ -5.15*10^{-8}+1.3*10^{-6}i & 1.60*10^{-8}+1.13*10^{-6}i & 1.87*10^{-4} & 9.05*10^{-9}-6.63*10^{-7}i \\ 2.47*10^{-8}-5.41*10^{-7}i & -8.89*10^{-9}-4.16*10^{-7}i & 9.05*10^{-9}-6.63*10^{-7}i & 1.28*10^{-4} \end{matrix}$$

and

$$K =$$

$$\begin{matrix} 0.48*10^{-4} & -9.27*10^{-8}+1.84*10^{-6}i & -7.34*10^{-8}+1.46*10^{-6}i & 8.46*10^{-8}-1.60*10^{-6}i \\ -9.27*10^{-8}+1.84*10^{-6}i & 26*10^{-4} & 3.37*10^{-8}-3.27*10^{-6} & -4.24*10^{-8}+3.22*10^{-6}i \\ -7.34*10^{-8}+1.46*10^{-6}i & 3.37*10^{-8}-3.27*10^{-6} & 19*10^{-4} & -1.66*10^{-7}+1.78*10^{-5}i \\ 8.46*10^{-8}-1.60*10^{-6}i & -4.24*10^{-8}+3.22*10^{-6}i & -1.66*10^{-7}+1.78*10^{-5}i & 93*10^{-4} \end{matrix}$$

For the proportionally damped system, these matrices are:

$$M = 10^{-4} * \begin{matrix} 4.0015 & 0 & 0 & 0 \\ 0 & 31.2558 & 0 & 0 \\ 0 & 0 & 1.8774 & 0 \\ 0 & 0 & 0 & 1.2840 \end{matrix}$$

$$K = 10^{-4} * \begin{matrix} 0.4858 & 0 & 0 & 0 \\ 0 & 25.9624 & 0 & 0 \\ 0 & 0 & 18.8401 & 0 \\ 0 & 0 & 0 & 92.7480 \end{matrix}$$

which are consistently diagonalized.

7.6 Conclusion

Modal analysis was successfully performed on an 4 DOF lumped elements system mimicking a stage 14 chicken embryo. Using a data set of physical properties obtained from the literature, we demonstrate that the transmitted power from any source to the

receiving system is dependent on the mobilities of the source and the receiver. The Mode Indicator Function, derived from an eigenvalue solution approach and using FRF matrix data, was applied to damped sinusoids and transient exponential signals to determine the position of resonances in the frequency range of interest. A least squares based modal parameters extraction was also successively applied to the impulse response function. These approaches were shown feasible on the real data set obtained from the literature. Therefore, given a realistic lumped elements model and knowing the physical properties of each element, our approach can be considered, contributing to limit the cost of experiments, which could be invasive and complicated to set up in vivo.

Knowledge gained from our study on the modal parameters estimated from organ (considered cell aggregates here) properties will help illuminate the investigation of the influence of mechanical vibrations during morphogenesis. This will also guide the design of implantable medical devices and the choice of the biomaterials used in their fabrication. Ultimately, this bio-application of modal analysis can be applied toward the development of a basic mammalian model, eventually leading to a realistic model.

CHAPTER 8. General conclusion and future works

8.1 Conclusions

The cells response to SWCNTs, low power ultrasound, cell culture substrate mechanical and surface energy changes as well as vibration of cell aggregates have been investigated in this thesis. Feeding HNBE cells with SWCNTs solution, we have identified marked changes in the expression of 14,294 genes, with 7,029 being up regulated and 7,265 being down regulated. Most of these genes are reported in this work for the first time as targets of SWCNTs exposure in human normal bronchial cells.

With a low power ultrasound of the order of 10^{-3} W/cm^2, we succeeded to reduce the proliferation rate of BT20 and BT20-E6/E7 breast cancer cells by 74.6% and 50.2% respectively in 48 hours in vitro. Moreover, the invasion ability of cervical cancer cells, HeLa, was reduced by 59.1%. These reductions were confirmed by up regulation of specific genes known to be responsible of cell proliferation and cell invasion.

For the influence of substrate mechanical properties on cell growth, the dosage of the curer in the base polymer in PDMS preparation was varied from 3.33% to 33.3%, yielding different values of the substrate stiffness. We were able to consistently show that cells viability and differentiation increase with an increasing substrate stiffness value. Additionally, increasing the plasma RF power exposure of the substrate from 7.16 W to 29.6 W significantly increased the biocompatibility of PDMS substrates.

In order to extend our investigation from cellular level to organs, we have analyzed the mechanical behavior of cell aggregates exposed to a transient signal. An inverse problem was formulated and successively solved with the purpose of extracting modal parameters of specific organs. We found a good agreement between the forward problem (analytical solution) and the inverse problem (least squares estimation) on a 4 DOF mimicking chick embryo system made of brain, heart, liver and limbs.

Overall, it appears that genome-wide monitoring of gene expression, in a translational approach involving engineering techniques, is important to understand the effect of mechanical and chemical conditioning of cells *in vitro*. The determination of biological or biomechanical parameters of cells and cell aggregates brings to biologists and biochemists, additional information essential to the advancement of knowledge on cell metabolism. These parameters include specific genes expression, cell differentiation, absorbance level and NAC in surrounding medium generated by cell growth, modal parameters of cell aggregates in morphogenesis, and others, which have been investigated in this thesis. The parameters might provide important information for improving therapeutic strategies applicable in a clinical setting. The techniques presented offer the opportunity to minimize the use of invasive diagnosis methods while avoiding loss of time due to repeated investigations of different sets of samples. Moreover, they provide new avenues for non-invasive characterization of cells or cell aggregates in response to different types of excitation. This new direction can help elucidating the effect of common chemical, physical, or mechanical potential pollutants on cells (or cell aggregates) in vitro. These pollutants include absorption of nanoparticles, changes in surface energy and mechanical properties, and can be used in conjunction with drug

testing. Therefore, an effective new drug discovery and development can be implemented based on some of the techniques presented in this thesis.

8.2 Future works

MEMS in biology is becoming one of the most spectacular fields of applications nowadays in the Microsystems community. In fact, MEMS technology and its applications have in general grown at a tremendous pace, while structural dimensions have grown smaller and smaller, reaching down even to the molecular level. Consequently, due to the low cost and biocompatibility of PDMS, the implementation of a time-limited and low-cost high-throughput-screening protocol for cell analysis and drug testing is achievable. This can be performed in real time, so that cell responses can be monitored as they happen. This will be advantageous in that it is non-invasive, meaning that cell behavior is not compromised and can be studied by several methods.

There are over 200 different known cancers that afflict humans and the results obtained in this thesis open to more extensive future collaboration between engineers and biologists toward the investigation of other markers relevant to the pathogenesis of cancer in vitro. More generally, a biomarker is anything that can be used as an indicator of a particular state of a disease; therefore, the techniques suggested in this thesis could be extended to the measure of characteristics that reflects the severity or presence of some disease state. This would lead to new avenues to noninvasively monitor the physiological state of an organism.

These future developments will most probably enhance knowledge of semi-analytical and experimental methods to be used for more extensive engineering analysis in the field of biomedicine.

References

1. Miron, L., 2000. *Oncologie general*¸ Ed. Egal, Bacau, 9-131.
2. Owens, J. Something old and something new: taking cancer therapy forward. *Drug Discovery Today* 2001, 6(23):1203–1206.
3. Stroescu, V., 1998. *Bazele farmacologice ale practicii medicale*, Ed. Med. Bucureuti.
4. Adams, J. Proteasome inhibition: a novel approach to cancer therapy. *Trends Mol. Med*. 2002, 8:49–54.
5. Anderson, S., Chiplin, J. Structural genomics: shaping the future of drug design? *Drug Disc. Today* 2002, 7(2):105–107.
6. Habeck, M. Starving cancer cells. *Drug Discovery Today* 2002, 7(12):635–637.
7. Lyden, D., Hu, Z., Caren, A., Kresty, L.A. Cancer targets and mechanisms. *Drug Discovery Today* 2001, 6:1252–1254.
8. Wong, J.M.Y. An end to immortal cancer cells? *Drug Discovery Today* 2002, 7:1072–1073.
9. Labhasetwar V. What is next for nanotechnology? J Biomed Nanotechnol 2005;1:373–374.
10. Park GE, Webster TJ. A review of nanotechnology for the development of better orthopedic implants. J Biomed Nanotechnol 2005;1:18–29.
11. Watari F, Abe S, Koyama C, Yokoyama A, Akasaka T, Uo M, Matsuoka M, Totsuka Y, Esaki M, Morita M, Yonezawa T. Behavior of in vitro, in vivo and internal motion of micro/nano particles of titanium, titanium oxides and others. J Ceram Soc Jpn 2008; 116:1–5.

12. Watari F, Yokoyama A, Omori M, Hirai T, Kondo H, Uo M, Kawasaki T. Biocompatibility of materials and development to functionally graded implant for bio-medical application. Compos Sci Technol 2004;64:893–908.

13. Yokoyama A, Sato Y, Nodasaka Y, Yamamoto S, Kawasaki T, Shindoh M, Kohgo T, Akasaka T, Uo M, Watari F, Tohji K. Biological behavior of hat-stacked carbon nanofibers in the subcutaneous tissue in rats. Nano Lett 2005;5:157–161.

14. Harrison BS, Atala A. Carbon nanotube applications for tissue engineering. Biomaterials 2007;28:344–353.

15. Mattson MP, Haddon RC, Rao AM. Molecular functionalization of carbon nanotubes and use as substrates for neuronal growth. J Mol Neurosci 2000;14:175–182.

16. Firkowska I, Olek M, Pazos-Perez N, Rojas-Chapana J, Giersig M. Highly ordered MWNT-based matrixes: Topography at the nanoscale conceived for tissue engineering. Langmuir 2006;22:5427–5434.

17. Aoki N, Yokoyama A, Nodasaka Y, Akasaka T, Uo M, Sato Y, Tohji K, Watari F. Strikingly extended morphology of cells grown on carbon nanotubes. Chem Lett 2006;35:508–509.

18. Correa-Duarte MA, Wagner N, Rojas-Chapana J, Morsczeck C, Thie M, Giersig M. Fabrication and biocompatibility of carbon nanotube-based 3D networks as scaffolds for cell seeding and growth. Nano Lett 2004;4:2233–2236.

19. Uo M, Tamura K, Sato Y, Yokoyama A, Watari F, Totsuka Y, Tohji K. The cytotoxicity of metal-encapsulating carbon nanocapsules. Small 2005;1:816–819.

20. Akasaka T, Watari F. Nano-architecture on carbon nanotube surface by biomimetic coating. Chem Lett 2005;34:826–827.

21. MacDonald RA, Laurenzi BF, Viswanathan G, Ajayan PM, Stegeman JP. Collagen-carbon nanotube composite materials as scaffolds in tissue engineering. J Biomed Mater Res A 2005;74:489–496.

22. Kam NWS, Jessop TC, Wender PA, Dai H. Nanotube molecular transporters: Internalization of carbon nanotube-protein conjugates into mammalian cells. J Am Chem Soc 2004;126: 6850–6851.

23. Kam NWS, Liu Z, Dai H. Functionalization of carbon nanotubes via cleavable disulfide bonds for efficient intracellular delivery of siRNA and potent gene silencing. J Am Chem Soc 2005;127:12492–12493.

24. Supronowicz PR, Ajayan PM, Ullmann KR, Arulanandam BP, Metzger DW, Bizios R. Novel current-conducting composite substrates for exposing osteoblasts to alternating current stimulation. J Biomed Mater Res 2002;59:499–506.

25. Chen RL, Bangsaruntip S, Drouvalakis KA, Kam NWS, Shim M, Li Y. Noncovalent functionalization of carbon nanotubes for highly specific electronic biosensors. Proc Natl Acad Sci USA 2003;100:4984–4989.

26. Kiura K, Sato Y, Yasuda M, Fugetsu B, Watari F, Tohji K, Shibata K. Activation of human monocytes and mouse splenocytes by single-walled carbon nanotubes. J Biomed Nanotechnol 2005;1:359–364.

27. Sato Y, Yokoyama A, Shibata K, Akimoto Y, Ogino S, Nodasaka Y, Kohgo T, Tamura K, Akasaka T, Uo M, Motomiya K, Jeyadevan B, Ishiguro M, Hatakeyama R, Watari F, Tohji K. Influence of length on cytotoxicity of multi-walled carbon

nanotubes against human acute monocytic leukemia cell line THP-I in vitro and subcutaneous tissue of rats in vivo. Mol Biosyst 2005;1:176–182.

28. Bianco A, Kostarelos K, Prato M. Applications of carbon nanotubes in drug delivery. Curr Opin Chem Biol 2005;9:674–9.

29. Smart SK, Cassady AI, Lu GQ, Martin DJ. The biocompatibility of carbon nanotubes. Carbon 2006;44:1028–33.

30. Pantarotto D, Briand J, Prato M, Pianco A. Translocation of bioactive peptides across cell membranes by carbon nanotubes. Chem Commun 2004;10:16–17.

31. Mwenifumbo S, Shaffer MS, Stevens MM. Exploring cellular behaviour with multi-walled carbon nanotube constructs. J Mater Chem 2007;17:1894–1902.

32. Lu Q, Moore JM, Huang G, Mount AS, Rao AM, Larcom LL. RNA polymer translocation with single-walled carbon nanotubes. Nano Lett 2004;4:2473–2477.

33. Cherukuri P, Bachilo SM, Litovsky SH, Weisman RB. Nearinfrared fluorescence microscopy of single-walled carbon nanotubes in phagocytic cells. J Am Chem Soc 2004;126: 15638–15639.

34. Bianco A, Hoebeke J, Godefroy S, Chaioin O, Pantarotto D, Briand JP. Cationic carbon nanotubes bind to CpG oligodeoxynucleotides and enhance their immunostimulatory properties. J Am Chem Soc 2005;127:58–59.

35. Zanello LP, Zhao B, Hu H, Haddon RC. Bone cell proliferation on carbon nanotubes. Nano Lett 2006;6:562–567.

36. Hu H, Ni Y, Montana V, Haddon RC, Parpura V. Chemically functionalized carbon nanotubes as substrates for neuronal growth. Nano Lett 2004;4:507–511.

37. Chen X, Tam UC, Czlapinski JL, Lee GS, Rabuka D, Zettl A. Interfacing carbon nanotubes with living cells. J Am Chem Soc 2006;128:6292–6293.

38. Hu H, Ni Y, Mandal SK, Montana V, Zhao B, Haddon RC. Polyethyleneimine functionalized single-walled carbon nanotubes as a substrate for neuronal growth. J Phys Chem B 2005;109:4285–4289.

39. Lacerda L, Raffa V, Prato M, Bianco A, Kostarelos K. Cellpenetrating carbon nanotubes in the delivery of therapeutics. Nano Today 2007;2:38–43.

40. Liu Z, Winters M, Holodniy M, Dai H. siRNA delivery of human T cells and primary cells with carbon-nanotube transporters. Angewandte Chemie 46(12): 2023-2027, 2007.

41. Kostarelos K, Lacerda L, Pastorin G, Wu W, Wieckowski S, Luangsivilay J, et al. A cellular uptake of functionalized carbon nanotubes is independent of functional group and cell type. Nat Nanotech 2007;2:108–13.

42. Margarita P, Quinteiro R. Fourier transform Infrared (FT-IR) Technology for the Identification of Organisms. Clinical Microbiology newsletter 22(8), 2000.

43. Wood, B.R., Quinn, M.A., Burden, F.R., and McNaughton, D. (1996) An investigation into FT-IR spectroscopy as a bio-diagnostic tool for cervical cancer. Biospectroscopy, 2: 143–153.

44. Wood, B.R., Quinn, M.A., Tait, B., Ashdown, M., Hislop, T., Romeo, M., and McNaughton, D. (1998) FTIR microspectroscopic study of cell types and potential confounding variables in screening for cervical malignancies. Biospectroscopy, 4: 75–91.

45. Sindhuphak, R., Issaravanich, S., Udomprasertgul, V., Srisookho, P., Warakamin, S., Sindhuphak, S., Boonbundarlchai, R., and Dusitsin, N. (2003) A new approach for the detection of cervical cancer in Thai women. Gynecologic Oncology, 90: 10–14.

46. Mordechai, S., Sahu, R.K., Hammody, Z., Mark, S., Kantarovich, K., Guterman, H., Podshyvalov, J., Goldstein, J., and Argov, S. (2004) Possible common biomarkers from FTIR microspectroscopy of cervical cancer and melanoma. Journal of Microscopy, 215 (1): 86–91.

47. Wang, H.P., Wang, H.-C., and Huang, Y.-J. (1997) Microscopic FTIR studies of lung cancer cells in pleural fluid. Science of the Total Environment, 204: 283–287.

48. Yano, K., Ohoshima, S., Grotou, Y., Kumaido, K., Moriguchi, T., and Katayama, H. (2000) Direct measurement of human lung cancerous and noncancerous tissues by fourier transform infrared microscopy: can an infrared microscope be used as a clinical tool? Analytical Biochemistry, 287: 218–225.

49. Yang Y, Sule-Suso J, Sockalingum GD, Kegelaer G, Manfait M, and El Haj AJ. Study of tumor cell invasion by Fourier transform infrared microspectroscopy. Biopolymers 78:311-317, 2005.

50. Eckel, R., Huo, H., Guan, H.-W., Hu, X., Che, X., and Huang, W.-D. (2001) Characteristic infrared spectroscopic patterns in the protein bands of human breast cancer tissue. Vibrational Spectroscopy, 27: 165–173.

51. Shafer-Peltier, K.E., Haka, A.S., Fitzmaurice, M., Crowe, J., Dasar, R.R., and Feld, M.S. (2002) Raman microspectroscopic model of human breast tissue: implications for breast cancer diagnosis in vivo. Journal of Raman Spectroscopy, 33: 552–563.

52. Weng, S.F., Ling, X.F., Song, Y.Y., Xu, Y.Z., Li, W.H., Zhang, X., Yang, L., Sun, W., Zhou, X., and Wu, J. (2000) FT-IR fiber optics and FT-Raman spectroscopic studies for the diagnosis of cancer. American Clinical Laboratory, 19 (7): 20.

53. Mordechai, S., Salman, A.O., Argov, S., Cohen, B., Erukhimovitch, V., Goldstein, J., Chaims, O., and Hammody, Z. (2000) Fourier-transform infrared spectroscopy of human cancerous and normal intestine. Proceedings of the SPIE, 3918: 66–77.

54. Fujioka, N., Morimoto, Y., Arai, T., and Kikuchi, M. (2004) Discrimination between normal and malignant human gastric tissues by Fourier transform infrared spectroscopy. Cancer Detection & Prevention, 28: 32–36.

55. Li, Q.B., Sun, X.J., Xu, Y.Z., Yang, L.M., Zhang, Y.F., Weng, S.F., Shi, J.S., and Wu, J.G. (2005) Diagnosis of gastric inflammation and malignancy in endoscopic biopsies based on Fourier transform infrared spectroscopy. Clinical Chemistry, 51 (2): 346–350.

56. Choo, L.-P., Mansfield, J.R., Pizzi, N., et al. (1995) Infrared spectra of human central nervous system tissue: Diagnosis of Alzheimer's disease by multivariate analyses. Biospectroscopy, 1 (2): 141–148.

57. Dovbeshko, G.I., Gridina, N.Y., Kruglova, E.B., and Pashchuk, O.P. (1997) FTIR spectroscopy studies of nucleic acid damage. Talanta, 53: 233–246.

58. Yoshida, S., Miyazaki, M., Sakai, K., Takeshita, M., Yuasa, S., Sato, A., Kobayashi, T., Watanabe, S., and Okuyama, H. (1997) Fourier transform infrared spectroscopic analysis of rat brain microsomal membranes modified by dietary fatty acids: possible correlation with altered learning behavior. Biospectroscopy, 3 (4): 281–290.

59. Gazi, E., Dwyer, J., Gardner, P., Ghanbari-Siakhani, A., Wde, A.P., Lockyer, N.P., Vickerman, J.C., Clarke, N.W., Shanks, J.H., Scott, L.J., Hart, C.A., and Brown, M. (2003) Applications of Fourier transform infrared microspectroscopy in studies of benign prostate and prostate cancer. A pilot study. Journal of Pathology, 201: 99–108.

60. Paluszkiewicz, C. and Kwiatek, W.M. (2001) Analysis of human cancer prostate tissues using FTIR microscopy and SXIXE techniques. Journal of Molecular Structure, : 565–566, 329–334.

61. Argov, S., Sahu, R.K., Bernshtain, E., Salam, A., Shohat, G., Zelig, U., and Mordechai, S. (2004) Inflammatory bowel diseases as an intermediate stage between normal and cancer: a FTIR-microspectroscopy approach. Biopolymers, 75: 384–392.

62. Richter, T., Steiner, G., Abu-Id, M.H., Salzer, R., Gergmann, R., Rodig, H., and Johannsen, B. (2002) Identification of tumor tissue by FTIR spectroscopy in combination with positron emission tomography. Vibrational Spectroscopy, 28: 103–110.

63. Rigas, B., Morgello, S., Goldman, I.S., and Wong, P.T.T. (1999) Human colorectal cancers display abnormal Fourier-transform infrared spectra, Proceedings of the National Academy of Sciences USA, 87: 8140–8144.

64. Rigas, B. and Wong, P.T.T. (1992) Human colon adenocarcinoma cell lines display infrared spectroscopic features of malignant colon tissues. Cancer Research, 52: 84–88.

65. Huleihel, M., Salman, A., Erukhimovich, V., Ramesh, J., Hammody, Z., and Mordechai, S. (2002) Novel optical method for study of viral carcinogenesis in vitro. Journal of Biochemical and Biophysical Methods, 50: 111–121.

66. Mossoba, M.M., Al-Khaldi, S.F., Kirkwood, J., Fry, F.S., Sedman, J., and Ismail, A.A. (2005) Printing microarrays of bacteria for identification by infrared microspectroscopy. Vibrational Spectroscopy, 38: 229–235.

67. Naumann, D. (1998) Infrared and NIR Raman spectroscopy in medical microbiology 3257: 245–257.

68. Dovbeshko, G.I., Chegel, V.I., Gridina, N.Y., Repnytska, O.P., Shirshov, Y.M., Tryndiak, V.P., Todor, I.M., and Solyanik, G.I. (2002) Surface enhanced IR absorption of nucleic acids from tumor cells: FTIR reflectance study. Biopolymer (Biospectroscopy), 67: 470–486.

69. Jalkanen, K.J., Würtz Jürgensen, V., Claussen, A., Rahim, A., Jensen, G.M., Wade, R.C., Nardi, F., Jung, C., Degtyarenko, I.M., Nieminen, R.M., Herrmann, F., Knapp-Mohammady, M., Niehaus, T.A., Frimand, K., and Suhai, S. (2006) Use of vibrational spectroscopy to study protein and DNA structure, hydration, and binding of biomolecules: A combined theoretical and experimental approach. Journal of Quantum Chemistry, 106: 1160–1198.

70. Binoy, J., Abraham, J.P., Joe, I.H., Jayakumar, V.S., Petit, G.R., and Nielsen, O.F. (2004) NIR-FT Raman and FT-IR spectral studies and ab initio calculations of the anti-cancer drug combretastatin-A4. Journal of Raman Spectroscopy, 35:939–946.

71. Faolain, E.O., Hunter, M.B., Byrne, J.M., Kelehan, P., McNamer, M., Byrne, H.J., and Lyng, F.M. (2005) A study examining the effects of tissue processing on

human tissue sections using vibrational spectroscopy. Vibrational Spectroscopy, 38: 121–127.

72. Sahu, P.K. and Mordechai, S. (2005) Fourier transform infrared spectroscopy in cancer detection. Future Oncology, 1: 635–647.

73. Pleshko, N.L., Boskey, A.L., and Mendelsohn, R. (1991) An FT-IR microscopic investigation of the effects of tissue preservation on bone. Calcified Tissue International, 51 (1): 72–77.

74. R.J. Pelham, Y. Wang. Proc Natl Acad Sci USA 94 (1997) 13661-13665.

75. S. Huang. J. Mol. Med. 77 (1999) 469–480.

76. L. Tranqui, P. Tracqui. C R Acad Sci III 323 (2000) 31-47.

77. E.K. Yim, R.M. Reano, S.W. Pang, A.F. Yee, C.S. Chen, K.W. Leong. Biomaterials 26 (2005) 5405-5413.

78. J. Folkman, A.Moscona. Nature 273 (1978) 345-349.

79. W.H. Guo, M.T. Frey, N.A. Burnham, Y.L. Wang. Biophysical Journal 90 (2006) 2213-2220.

80. K.A. Beningo, Y.L. Wang. Trends Cell Biol 12 (2002) 79-84.

81. S. Fereol, R. Fodil, B. Labat, S. Galiacy, V.M. Laurent, B. Louis, D. Isabey, E. Planus. Cell Motil Cytoskeleton 63 (2006) 321-340.

82. S. Li, S. Bhatia, Y.L. Hu, Y.T. Shiu, Y.S. Li, S. Usami, S. Chien. Biorheology 38 (2001) 101-108.

83. M.J. Paszek, V.M. Weaver. J Mammary Gland Biol Neoplasia 9 (2004) 325-342.

84. T. G. van Kooten, H. T. Spijker, and H. J. Busscher, "Plasma-treated polystyrene surfaces: model surfaces for studying cell-biomaterial interactions," *Biomaterials,* vol. 25, pp. 1735-1747, 2004.

85. T. Groth and G. Altankov, "Studies on cell-biomaterial interaction: role of tyrosine phosphorylation during fibroblast spreading on surfaces varying in wettability," *Biomaterials,* vol. 17, pp. 1227-1234, 1996.

86. B. A. Langowski and K. E. Uhrich, "Microscale Plasma-Initiated Patterning (pPIP)," *Langmuir,* vol. 21, pp. 10509-10514,2005.

87. Michael Junkin, Jennifer Watson, Jonathan P. Vande Geest, and Pak Kin Wong, "Template-Guided Self-Assembly of Colloidal Quantum Dots using Plasma Lithography", *Advanced Materials* 21, 1247-1251, 2009

88. Junkin M and Wong PK, "Probing Cell Migration in Confined Environments by Plasma Lithography", *Biomaterials* 32, 1848-1855, 2011.

89. Junkin M, Leung SL, Yang Y, Lu Y, Volmering J, and Wong PK. Plasma lithography surface patterning for creation of cell networks. *Journal of Visualized Experiments* 52, 2011.

90. Fuard D, Tzvetkova-Chevolleau T, Decossas S, Tracqui P, Schiavone P. Optimization of Poly-Di-Methyl-Siloxane (PDMS) substrates for studying cellular adhesionand motility. *Microelectronic Engineering* 85, 5-6 (2008) 1289-1293.

91. Bailey MR, Khokhlova VA, Sapozhnikov OA, et al. Physical mechanisms of the therapeutic effects of ultrasound. *Acoust. Phys*. 49 (2003) 369.

92. Riesz P, Berdahl D, Christman CL. Free radical generation by ultrasound in aqueous and nonaqueous solutions. *Environ. Health Perspect*. 64 (1985) 233.

93. Kondo T, Umemura S, Tanabe K, Jpn. J. Hyperthermic Oncol. 16 (2000) 203.

94. Feril LB, Kondo T, Umemura S, Tashibana K, et al. J. Med. Ultrason. 29 (winter) (2002) 173.

95. Rosenthal I, Sostaric JZ, Riesz P. Sonodynamic therapy - a review of the synergistic effects of drugs and ultrasound. Ultrasonics Sonochemistry 11 (2004) 349-363.

96. Miller DL, Bao S, Gies RA, Thrall BD. Ultrasonic enhancement of gene transfection in murine melanoma tumors. Ultrasound Md Biol 1999; 25:1425-1430.

97. Miller DL, pislaru SV, Greenleaf JE. Sonoporation: mechanical DNA delivery by ultrasonic cavitation. Somat Cell Mol genet 2002; 27: 115-134.

98. Ward M, Wu J, Chiu JF. Experimental study of the effects of Optison concentration on sonoporation in vitro. Ultrasound Med Biol 2000; 26:1169-1175.

99. Pan H, Zhou Y, Sieling F, Shi J, Cui J, Deng C. Sonoporation of cells for drug and gene delivery. Conf Proc IEEE Eng Med Biol Soc. 2004;5:3531-4.

100. Frenkel V, Oberoi J, Stone MJ, Park M, et al. Pulsed high-intensity focused ultrasound enhances thrombolysis in an in vitro model. Radiology 239: 86-93, 2006.

101. Frenkel V. Ultrasound mediated delivery of drugs and genes to solid tumors. Advanced drug delivery reviews 60: 1193-1208, 2008.

102. Burks SR, Ziadloo A, Hancock HA, et al. Investigation of cellular and molecular responses to pulsed focused ultrasound in a mouse model. PLoS ONE 6 (9): e24730, 2011.

103. Snider P, Conway SJ. Developmental biology: the power of blood. Nature 2007, 450:180-1.

104. Pierce GB. The cancer cell and its control by the embryo. Rous-Whipple Award lecture. Am J Pathol. 1983; 113:117-24.

105. William JW 3rd, Carlson DL, Gadson RG, et al. Cytogenetic analysis of triploid renal carcinoma in Rana pipiens. Cytogenet. Cell Genet. 1993; 64: 18-22.

106. Monk M, Holding C. Human embryonic genes re-expressed in cancer cells. Oncogene 2001; 20:8085-91.

107. Zhang N, Yan X, Jiang S, et al. Experimental study on co-culture of early embryo and cancer cells in vitro. Journal of Biomedical Engineering 26(2): 334-337, 2009.

108. Wang Y. Wnt/Planar cell polarity signaling: a new paradigm for cancer therapy. Mol Cancer Ther. 2009; 8: 2103–9.

109. Ma Y, Peng J, Liu W, et al. Proteomics identification of desmin as a potential oncofetal diagnostic and prognostic biomarker incolorectal cancer. Mol Cell Proteomics. 2009; 8: 1878–90.

110. Wilczynski JR. Cancer and pregnancy share similar mechanisms of immunological escape. Chemotherapy. 2006; 52: 107–10.

111. Xie K, Abbruzzese JL. Developmental biology informs cancer: the emerging role of the hedgehog signaling pathway in upper gastrointestinal cancers. Cancer Cell. 2003; 4: 245–7.

112. Wu F, Stutzman A, Mo YY. Notch signaling and its role in breast cancer. Front Biosci. 2007; 12: 4370–83.

113. Vogelstein B, Kinzler KW. Cancer genes and the pathways they control. Nat Med. 2004; 10: 789–99.

114. Ingber DE, Tensegrity I. Cell structure and hierarchical systems biology. J. Cell Sci 2003; 116: 1157-73.

115. Ingber DE. Cellular tensegrity: defining new rules of biological design that govern the cytoskeleton. J. Cell Sci 1993; 104: 613-27.

116. Chen J, Fabry B, Schiffrin EL, Wang N. Twisting integrin receptors increases endothelin-1 gene expression in endothelial cells. Am J Physiol 2001; 280:C1475-84.

117. Stamenovic D, Liang Z, Chen J, Wang N. Effect of the cytoskeletal prestress on the mechanical impedance of cultured airway smooth muscle cells. J Appl Physiol 2002; 92: 1443-50.

118. Balaban NQ, Schwarz US, Riveline D, Goichberg P, et al. Force and focal adhesion assembly: a close relationship studied using elastic micropatterned substrates. Nat Cell Biol 2001; 3: 466-72.

119. Riveline D, Zamir E, Balaban NQ, Scwarz US, et al. Focal contacts as mechanosensors: externally applied local mechanical force induces growth of focal contacts by an mDia1-dependent and ROCK-independent mechanism. J Cell Biol 2001; 153: 1175-86.

120. G. ter Haar, Therapeutic and surgical applications. Physical Principles of Medical Ultrasonics, Ellis Horwood Ltd., Chichester (1986), pp. 436-461.

121. G.K. Von Schulthess and H.J. Smith, The Encyclopaedia of Medical Imaging, Vol.1: Physics, techniques, and procedures, The Nicer Institute: Isis Medical Media, 1999.

122. Burgers, J.M. A Mathematical Model illustrating the theory of Turbulence. Advances in Applied Mechanics, vol. 1, 1948.

123. Cappella B, Dietler G. Surf. Sci. Rep. 1999, 34, 1.

124. Mandeville, C.W., Webster, J.D., Rutherford, M.J., Taylor, B.E., Timbal, A., and Faure, K. (2002) Determination of molar absorptivities for infrared absorption bands of H2O in andesitic glasses. American Mineralogist, 87: 813–821.

125. Seaman, S.J., Dyar, M.D., Marinkovic, N., and Dunbar, N.W. (2006) An FTIR study of hydrogen in anorthoclase and associated melt inclusions. American Mineralogist, 91: 12–20.

126. Fabian, H., Jackson, M., Murphy, L., Watson, P.H., Fichtner, I., and Mantsch, H.H.

127. (1995) A comparative infrared spectroscopic study of human breast tumors and breast tumor cell xenografts. Biospectroscopy, 1 (1): 37–45.

128. Alazzam A, Mfoumou E, Stiharu I, Kassab A, et al. Identification of deregulated genes by single wall carbon nanotubes in human normal bronchial epithelial cells. Nanomedicine 2010 Aug; 6(4):563-9.

129. Etienne Mfoumou, Narayanswami Sivakumar, Amber Yasmeen, Ala-Eddin Al Moustafa, and Ion Stiharu. A new concept to measure cell proliferation using Fourier transform infrared spectroscopy. Medical Hypotheses 79:171-173, 2012.

130. Etienne Mfoumou, Sivakumar Narayanswamy, Ion Stiharu, and Ala-Eddin. Al Moustafa. Low Power Ultrasound Inhibits Cell Proliferation and Invasion of

Human Cancer Cells in Vitro. Clinical Cancer Investigation Journal, 2012, 1(2):51-6.

131. Etienne Mfoumou, Sivakumar Narayanswamy, Ion Stiharu, and Ala-Eddin. Al Moustafa. On the feasibility of an *in vitro* noninvasive absorbance-based cell proliferation analysis technique, using cell culture media. In press. Spectroscopy Letters, 2012. ID: 686143 DOI:10.1080/00387010.2012.686143.
132. Etienne Mfoumou, Ion Stiharu, Sivakumar Narayanswamy, and Ala-Eddin. Elasticity-triggered biological responses of SH-SY5Y neuroblastoma cells in vitro. Under review, Biomedical Materials and Engineering, 2012.
133. Etienne Mfoumou, Ion Stiharu, Jean Atangana A., Sivakumar Narayanswamy, and Ala-Eddin. Al Moustafa. Mechanical vibration analysis and its application to modal parameters estimation in early avian embryo. Under review, Mechanics of Research Communications, 2012.
134. Service RF. Nanotoxicology. Nanotechnology grows up. Science 2004;304:1732-4. 134. Sun YP, Fu K, Lin Y, Huang W. Functionalized carbon nanotubes: properties and applications. Acc Chem Res 2002;35:1096-104.
135. Donaldson K. Resolving the nanoparticles paradox. Nanomed 2006;1:229-34.
136. Tsuji JS, Maynard AD, Howard PC, James JT, Lam CW, Warheit DB, et al. Research strategies for safety evaluation of nanomaterials, part IV: risk assessment of nanoparticles. Toxicol Sci 2006;89:42-50.
137. Lam CW, James JT, McCluskey R, Hunter RL. Pulmonary toxicity of single-wall carbon nanotubes in mice 7 and 90 days after intratracheal instillation.Toxicol Sci 2004;77:126-34.

138. Warheit DB, Laurence BR, Reed KL, Roach DH, Reynolds GA, Webb TR. Comparative pulmonary toxicity assessment of single-wall carbon nanotubes in rats. Toxicol Sci 2004;77:117-25.

139. Muller J, Huaux F, Moreau N, Misson P, Heilier JF, Delos M, et al. Respiratory toxicity of multi-wall carbon nanotubes. Toxicol Appl Pharmacol 2005;207:221-31.

140. Shvedova AA, Kisin ER, Mercer R, Murray AR, Johnson VJ, Potapovich AI, et al. Unusual inflammatory and fibrogenic pulmonary responses to single-walled carbon nanotubes in mice. Am J Physiol Lung Cell Mol Physiol 2005;289:L698-708

141. Mangum JB, Turpin EA, Antao-Menezes A, Cesta MF, Bermudez E, Bonner JC. Single-walled carbon nanotube (SWCNT)-induced interstitial fibrosis in the lungs of rats is associated with increased levels of PDGF mRNA and the formation of unique intercellular carbon structures that bridge alveolar macrophages in situ. Part Fibre Toxicol 2006;3:15.

142. Li Z, Hulderman T, Salmen R, Chapman R, Leonard SS, Young SH, et al. Cardiovascular effects of pulmonary exposure to single-wall carbon nanotubes. Environ Health Perspect 2007;115:377-82.

143. Mercer RR, Scabilloni J, Wang L, Kisin E, Murray AR, Schwegler-Berry D, et al. Alteration of deposition pattern and pulmonary response as a result of improved dispersion of aspirated single-walled carbon nanotubes in a mouse model. Am J Physiol Lung Cell Mol Physiol 2008;294:L87-97.

144. Simon-Deckers A, Gouget B, Mayne-L'hermite M, Herlin-Boime N, Reynaud C, Carrière M. In vitro investigation of oxide nanoparticle and carbon nanotube

toxicity and intracellular accumulation in A549 human pneumocytes. Toxicology 2008;253:137-46.

145. Tabet L, Bussy C, Amara N, Setyan A, Grodet A, Rossi MJ, et al. Adverse effects of industrial multiwalled carbon nanotubes on human pulmonary cells. J Toxicol Environ Health 2009;72:60-73.

146. Chou CC, Hsiao HY, Hong QS, Chen CH, Peng YW, Chen HW, et al. Single-walled carbon nanotubes can induce pulmonary injury in mouse model. Nano Lett 2008;8:437- 45.

147. Cui D, Tian F, Ozkan CS, Wang M, Gao H. Effect of single wall carbon nanotubes on human HEK293 cells. Toxicol Lett 2005;155:73-85.

148. Brush MH, Shenolikar S. Control of cellular GADD34 levels by the 26S proteasome. Mol Cell Biol 2008;28:6989-7000.

149. Harding HP, Zhang Y, Scheuner D, Chen JJ, Kaufman RJ, Ron D. Ppp1r15 gene knockout reveals an essential role for translation initiation factor 2 alpha (eIF2alpha) dephosphorylation in mammalian development. Proc Natl Acad Sci U S A 2009;106:1832-7.

150. Morton E, Macrae IM, McCabe C, Brown SM, White F. Identification of the growth arrest and DNA damage protein GADD34 in the normal human heart and demonstration of alterations in expression following myocardial ischaemia. Int J Cardiol 2006;107:126- 9.

151. Huang X, Li X, Guo B. KLF6 induces apoptosis in prostate cancer cells through upregulation of ATF3. J Biol Chem 2008;283:29795-801.

152. Yin X, Dewille JW, Hai T. A potential dichotomous role of ATF3, an adaptiveresponse gene, in cancer development. Oncogene 2008;27:2118-27.

153. Hayakawa H, Hayakawa M, Kume A, Tominaga S. Soluble ST2 blocks interleukin-33 signaling in allergic airway inflammation. J Biol Chem 2007;282:26369-80.

154. Schmitz J, Owyang A, Oldham E, Song Y, Murphy E, McClanahan TK, et al. IL-33, an interleukin-1-like cytokine that signals via the IL-1 receptor-related protein ST2 and induces T helper type 2-associated cytokines. Immunity 2005;23:479-90.

155. Greiner J, Ringhoffer M, Taniguchi M, Schmitt A, Kirchner D, Krähn G, et al. Receptor for hyaluronan acid-mediated motility (RHAMM) is a new immunogenic leukemia-associated antigen in acute and chronic myeloid leukemia. Exp Hematol 2002;30:1029-35.

156. Hamilton SR, Fard SF, Paiwand FF, Tolg C, Veiseh M, Wang C, et al. The hyaluronan receptors CD44 and Rhamm (CD168) form complexes with ERK1,2 that sustain high basal motility in breast cancer cells. J Biol Chem 2007;282:16667-80.

157. Proost P, Mortier A, Loos T, Vandercappellen J, Gouwy M, Ronsse I, et al. Proteolytic processing of CXCL11 by CD13/aminopeptidase N impairs CXCR3 and CXCR7 binding and signaling and reduces lymphocyte and endothelial cell migration. Blood. 2007;110:37-44.

158. Satish L, Blair HC, Glading A, Wells A. Interferon-inducible protein 9 (CXCL11)-induced cell motility in keratinocytes requires calcium flux-dependent activation of mucalpain. Mol Cell Biol 2005;25:1922-41.

159. Madhavan J, Mitra M, Mallikarjuna K, Pranav O, Srinivasan R, Nagpal A, et al. KIF14 and E2F3 mRNA expression in human retinoblastoma and its phenotype association. Mol Vis 2009;15:235-40.

160. Taniuchi K, Nakagawa H, Nakamura T, Eguchi H, Ohigashi H, Ishikawa O, et al. Down-regulation of RAB6KIFL/KIF20A, a kinesin involved with membrane trafficking of discs large homologue 5, can attenuate growth of pancreatic cancer cell. Cancer Res 2005;65:105-12.

161. Miki H, Setou M, Kaneshiro K, Hirokawa N. All kinesin superfamily protein, KIF, genes in mouse and human. Proc Natl Acad Sci U S A 2001;98:7004-11.

162. Belyaev IY, Koch CB, Terenius O, Roxström-Lindquist K, Malmgren LO, H Sommer W, et al. Exposure of rat brain to 915 MHz GSM microwaves induces changes in gene expression but not double stranded DNA breaks or effects on chromatin conformation. Bioelectromagnetics 2006;27:295-306.

163. Qutob SS, Chauhan V, Bellier PV, Yauk CL, Douglas GR, Berndt L, et al. Microarray gene expression profiling of a human glioblastoma cell line exposed in vitro to a 1.9 GHz pulse-modulated radiofrequency field. Radiat Res 2006;165:636-44.

164. Paparini A, Rossi P, Gianfranceschi G, Brugaletta V, Falsaperla R, De Luca P, et al. No evidence of major transcriptional changes in the brain of mice exposed to 1800 MHz GSM signal. Bioelectromagnetics 2008; 29:312-23.

165. Sharma P, Rajalingam D, Krishnaswamy T, Kumar S, Singh S. A light scattering study of the interaction of Fibroblast Growth Factor (FGF) with its receptor. Biophysical Journal 2008; 94(9):L71-73.

166. Crissman H A, Steinkamp J A. A new method for rapid and sensitive detection of bromodeoxiuridine in DNA-replicating cells. Experimental Cell Research 1987; 173:256-261.

167. Gratzner H G. Monoclonal antibody to 5-bromo- and 5-iododeoxyuridine: A new reagent for detection of DNA replication. Science 1982; 218:474-475.

168. Boddington S, Henning T D, Sutton E J, Daldrup-Link H E. Labeling stem cells with fluorescent dyes for non-invasive detection with optical imaging. Journal of Visualized Experiments 2008; 14:686.

169. Daldrup-Link H E, Rudelius M, Metz S, et al. Stem cell tracking with Gadophrin-2 –a bifunctional contrast agent for MR imaging, optical imaging and fluorescence microscopy. European Journal of Nuclear Medicine and Molecular Imaging 2004; 31(9):1312-1321.

170. Simon GH, Daldrup-Link HE, Kau J, et al. Optical imaging of experimental arthritis using allogeneic leukocytes labeled with a near-infrared fluorescent probe. European Journal of Nuclear Medicine and Molecular Imaging 2006; 33:998-1006.

171. Sutton E, Henning T, Pichler B, Bremer C, Daldrup-Link HE. Cell tracking with optical imaging. Eur Radiol. 2008; May 28 [Epub ahead of print], & Eur Radiol 2003; 2:350-357.

172. Funovics MA, Alencar H, Su HS, Khazaie K, Weissleder R, Mahmood U. Miniaturized multichannel near infrared endoscope for mouse imaging. Molecular imaging 2003; 2:350-357.

173. Rye HS, Drees BL, Nelson HC, Glazer AN. Stable fluorescent dye-DNA complexes in high sensitivity detection of protein-DNA interactions. Application to

heat shock transcription factor. The Journal of Biological Chemistry 1993; 268(33):25229-25238.

174. Ishibashi J, Yamashita K, Ishikawa T, et al. The effects inhibiting the proliferation of cancer cells by far-infrared radiation (FIR) are controlled by the basal expression level of heat shock protein (HSP) 70A. Medical Oncol 2008; 25:229-237.

175. Shima H, Yamamoto S, Qiu J, et al. Far-infrared rays control prostate cancer cells *in vitro* and *in vivo*. Nature Precedings 2008, http://hdl.handle.net/10101/npre.2008.1980.1

176. Wong PTT, Rigas B. Infrared spectra of microtome sections of human colon tissues. Applied spectroscopy 1990; 44:1715-1718.

177. Wong PTT Papavassiliou ED, Rigas B. Phosphodiester stretching bands in the infrared spectra of human tissues and cultured cells. Applied spectroscopy 1991; 45(9):1563-1567.

178. Yazdi HM, Bertrand MA, Wong PT. Detecting structural changes at the molecular level with Fourier transform infrared spectroscopy. Acta Cytologica 1996;40:664-668.

179. Benedetti E, Bramanti E, Rossi I. Determination of the relative amount of nucleic acids and proteins in leukemic and normal lymphocytes by means of FTIR microspectroscopy. Applied spectroscopy 1997; 51:792-797.

180. Chiriboga L, Xie P, Zarou D, Diem M. Infrared spectroscopy of human tissue. IV. Detection of dysplastic and neoplastic changes of human cervical tissue via infrared microscopy. Cellular and molecular biology 1998; 44:219-229.

181. Yang D, Castro D, El-Sayed I, El-Sayed M, Saxton R, Nancy Y. A Fourier transform infrared spectroscopic comparison of cultured human fibroblast and fibrosarcoma. SPIE 1995; 2389:543-550.

182. Mantsch HH, Chapman D. Infrared spectroscopy of biomolecules. John Wiley 1996; New York.

183. Jackson M, Tetteh J, Mansfield B, et al. Cancer diagnosis by infrared spectroscopy: methodology aspects. SPIE 1998; 3257:24-34.

184. Diem MS, Boydsom W, Chiriboga L. Infrared spectroscopy of cells and tissues: shining light onto a novel subject. Applied spectroscopy 1999; 53:148-161.

185. Franck P, Nabet P, Dousset B. Applications of infrared spectroscopy to medical biology. Cellular and molecular biology 1998; 44:273-275.

186. Huleihel M, Talyshinsky M, Erukhimovitch V. FTIR microscopy as a method for detection of retrovirally transformed cells. Spectroscopy 2001; 15:57-64.

187. Wong P, Goldstein S, Grekin R, Godwin A, Pivik C, Rigas B. Distinct infrared spectroscopic pattern of human basal cell carcinoma of the skin. Cancer research 1993; 53:762-765.

188. Afanasyeva NI, Kolyakov FS, Artjushenko SG, Sokolov VV, Franck GA. Minimally invasive and ex vivo diagnostics of breast cancer tissues by fiber optic evanescent wave Fourier transform IR (FEW-FTIR) spectroscopy. SPIE 1998; 3250:140-146.

189. Lasch P, Naumann D. FTIR microspectroscopic imaging of human carcinoma thin sections based on pattern recognition techniques. Cellular and molecular biology 1998; 44:189-202.

190. Mordechai S, Argov S, Salman A, et al. FTIR microscopic comparative study on normal, premaligant and malignant tissues of human intestine. SPIE 2000; 4129:231-242.

191. Wang HP, Wang HC, Huang YJ. Microscopic FTIR studies of lung cancer cells in pleural fluid. The Science of the Total Environment 1997; 204:283-287.

192. Gao T, Feng J, Ci Y. Human breast carcinoma tissues display distinctive FTIR spectra: implication for the histological characterization of carcinomas. Analytical cellular pathology 1999; 18:87-93.

193. Yasmeen A, Bismar AT, Kandouz M, Foulkes WD, Desprez PY, Al Moustafa AE. E6/E7 of HPV type 16 promotes cell invasion and metastasis of human breast cancer cells. Cell cycle 2007; 6(16):2038-2042.

194. Lawri SR. The analysis of exfoliated cervical cells by infrared microscopy. Cellular and molecular biology 1998; 44:169-177.

195. Malins DC, Polissar NL, Gunselman SJ. Models of DNA structure achieve almost perfect discrimination between normal prostate, benign prostatic hyperplasia (BPH) and prostate cancer. Proceedings of the national academy of sciences 1994; 94:259-264.

196. Dyson M. Mechanisms involved in therapeutic ultrasound. Physiotherapy 1987; 73:116-120.

197. Kitchen SS, Partridge CJ. A review of therapeutic ultrasound. Physiotherapy 1990; 76: 593-600.

198. Draper DO, Schulthies S, Sorvisto P, Hautala AM. Temperature changes in deep muscles of humans during ice and ultrasound therapies: an *in-vivo* study. J Orthop Sports Phys Ther 1995; 21:153-157.

199. Chan AK, Myrer J, Measom G, Draper DO. Temperature changes in human patellar tendon in response to therapeutic ultrasound. J Athl Train 1998; 33:130-135.

200. Loch EG, Fischer AB, Kuwert E. Effect of diagnostic and therapeutic intensities of ultrasonics on normal and malignant human cells in vitro. Am J Obstet Gynecol 1971; 110:457-460.

201. Pizzarello DJ, Wolsky A, Becker MH, Keegan AF. A new approach to testing the effects of ultrasound on tissue growth and differentiation. Oncology 1975; 31:226-232.

202. Webster DF, Pond JB, Dyson M, Harvey W. The role of cavitation in the in vitro stimulation of protein synthesis in human fibroblasts by ultrasound. Ultrasound Med Biol 1978; 4:343-351.

203. Naugolnykh K. Nonlinear Acoustics: from Research in Physics to Application (Historical Incidents), Acoustical Physics 2009; 55:335-341.

204. ter Haar G. Therapeutic and surgical applications - Physical Principles of Medical Ultrasonics (Ellis Horwood Ltd, Chichester) 1986; 436-461.

205. Mitragptri S, Blankschtein D, Langer R. Ultrasound-mediated transdermal protein delivery. Science 1995; 2269:850.

206. Everbach E, Francis C. Cavitational mechanisms in ultrasound-accelerated thrombolysis at 1 MH. Ultrasound Med Biol 2000; 26:1153-1160.

207. Hill C, ter Haar G. Review article: high-intensity focused ultrasound – potential for cancer treatment. Br. J. Radiol 1995; 68:1296.

208. Paliwal S, Mitragotri S. Ultrasound-induced cavitation: applications in drug delivery and gene delivery. Expert Opin Drug Deliv 2006; 3:713-726.

209. Mitragotri S. Innovation: healing sound: the use of ultrasound in drug delivery and other therapeutic applications. Nat. Rev. Drug. Discov 2005; 4:255-260.

210. Watanabe A, Nishimura H, Kawashima N, Takeuchi S. Consideration on suppression of cancer cell proliferation by ultrasound exposure using sonochemical and biological measurements. J Phys: Conf Ser 1 2004; 210-215.

211. Yasmeen A, Bismar T.A, Kandouz M, Foulkes W.D, Desprez P.Y, Al Moustafa A.E. E6/E7 of HPV type 16 promotes cell invasion and matastasis of human breast cancer cells. Cell Cycle 2007; 6:2038-2042.

212. Yasmeen A, Alachkar A, Dekhil H, Gambacorti-Passerini C, Al Moustafa A.E. Locking Src/Abl Tyrosine Kinase Activities Regulate Cell Differentiation and Invasion of Human Cervical Cancer Cells Expressing E6/E7 Oncoproteins of High-Risk HPV. J Oncol 2010; 530130.

213. Al Moustafa A.E, Foulkes W.D, Benlimame N, Wong A, Yen L, Bergeron J, et al. E6/E7 proteins of HPV type 16 and ErbB-2 cooperate to induce neoplastic transformation of primary normal oral epithelial cells. Oncogene 2004; 23:350-358.

214. Kong N, Fotouhi N, Wovkulich P.M, Roberts J. Cell cycle inhibitors for the treatment of cancer. Drugs Fut 2003; 28:881-896.

215. Hrazdira I, Skorpikova J, Dolnikova M. Ultrasonically induced alterations of cultured tumour cells. Eur J Ultrasound 1998; 8:43-49.

216. Lin CQ, Singh J, Murata K, Itahana Y, Parrinello S, Liang SH, et al. A role for Id-1 in the aggressive phenotype and steroid hormone response of human breast cancer cells. Cancer Res 2000; 60:1332-1340.

217. Fong S, Itahana Y, Sumida T, Singh J, Coppe JP, Liu Y, et al. Id-1 as a molecular target in therapy for breast cancer cell invasion and metastasis. Proc Natl Acad Sci USA2003; 100:13543-13548.

218. Koda M, Sulkowski S, Garofalo C, Kanczuga-Koda L, Sulkowska M, Surmacz E. Expression of the insulin-like growth factor-I receptor in primary breast cancer and lymph node metastases: correlations with estrogen receptors alpha and beta. Horm Metab Res 2003; 35:794-801.

219. Nielsen TO, Andrews HN, Cheang M, Kucab JE, Hsu FD, Ragaz J, et al. Expression of the insulin-like growth factor I receptor and urokinase plasminogen activator in breast cancer is associated with poor survival: potential for intervention with 17-allylamino geldanamycin. Cancer Res 2004; 64:286-291.

220. Sloan EK, Stanley KL, and Anderson RL. Caveolin-1 inhibits breast cancer growth and Metastasis. Oncogene2004; 23:7893-7897.

221. ter Haar GR. Biological Effects of Ultrasound in Clinical Applications. In Suslick KS (ed) Ultrasound: its chemical, physical, and biological effects, 1988, chapter 8.

222. ter Haar GR, Daniels S. Evidence for ultrasonically induced cavitation in vivo. *Phys Med Biol 1981;* 26:1145.

223. Galperin H, Kirsch M, Levi S. Fragmentation of purified mammalian DNA molecules by ultrasound below human therapeutic doses. Hum Genet 1975; 29:61-66.

224. Chapelon JY, Margonari J, Vernier F, Gorry F, Ecochard R, Gelet A. In vivo effects of high-intensity ultrasound on prostatic adenocarcinoma dunning R3327. Cancer Res 1992; 52:6353-6357.

225. Kondo T, Arai S, Kuwabara M, Yoshii G, Kano E. Damage in DNA irradiated with 1.2 MHz ultrasound and its effect on template activity of DNA for RNA synthesis. Radiat Res 1985; 104:284-292.

226. Tsai WC, Chen JY, Pang JH, Hsu CC, Lin MS, Chieh LW. Therapeutic ultrasound stimulation of tendon cell migration, Connect Tissue Res 2008; 49:367-373. 227. Mahoney CM, Morgan MR, Harrison A, Humphries MJ, Bass MD. Therapeutic ultrasound bypasses canonical syndecan-4 signaling to activate rac1. J Biol Chem 2009; 284:8898-909.

227. 228. Yeung, T.; Georges, P.C.; Flanagan, L.A.; et al. Effect of substrate stiffness on cell morphology, cytoskeletal structure, and adhesion. Cell Motil. Cytoskel., 2005, 60, 24-34.

228. 229. Evans, N.D.; Minelli, C.; Gentleman, E. et al. Substrate stiffness affects early differentiation events in embryonic stem cells. Eur. Cell. Mater., 2009, 18, 1-14.

229. 230. Junkin, M; Leung, S.L.; Yang, Y.; et al. Plasma lithography surface patterning for creation of cell networks. J. Vis. Exp., 2011, 52.

230. 231. Beaulieu, I. ; Geissler, M. ; Mauzeroll, J. *Oxygen Plasma Treatment of Polystyrene and Zeonor: Substrates for Adhesion of Patterned Cells.* Langmuir, 2009, 25(12), 7169-7176.

231. 232. Choi S.C.; Choi, W.K.; Jung, H.J.; et al. Relation between hydrophilicity and cell culturing on polystylene petri dish modified by ion-assisted reaction. J. Appl. Polym. Sci., 1999, 73-41.

232. 233. Shahidzadeh-Ahmadi, N; Chechimi, M.M.; Arefi-Khonsari, F. et al. A physicochemical study of oxygen plasma-modified polypropylene. Colloids Surf. Physicochem. Eng. Asp., 1995, 105-277.

233. 234. Cotter, T. G.; Al-Rubeai, M. Cell death (apoptosis) in cell culture systems. Trends Biotechnol., 1995, 13, 150–155.

234. 235. Koopman, G.; Reutelingsperger, C. P.; Kuijten, G. A.; Keehnen, R. M.; et al. Annexin V for flow cytometric detection of phosphatidylserine expression on B cells undergoing apoptosis. Blood, 1994, 84, 1415–1420.

235. 236. Taatjes, D.; Sobel, B.; Budd, R. Morphological and cytochemical determination of cell death by apoptosis. Histochem. Cell Biol., 2008, 129(1), 33–43.

236. 237. Park et al., BioChips J. 4(3):230-236, 2010

237. 238. Ciccarone, V., Spengler, B. A., Meyers, M. B., Biedler, J. L., and Ross, R. A. Phenotypic Diversification in Human Neuroblastoma Cells: Expression of Distinct Neural Crest Lineages, Cancer Research. *49:* 219-225, 1989.

238. 239. Ross, R., Spengler, B., Domenech, C., Porubcin, M., Rettig, W., and Biedler, J. Human neuroblastoma I-type cells are malignant neural crest stem cells, Cell Growth & Differentiation. *6:* 449-456, 1995.

239. 240. Ross, R. A., Spengler, B. A., Rettig, W. J., and Biedler, J. L. Differentiation-Inducing Agents Stably Convert Human Neuroblastoma I-Type Cells to

Neuroblastic (N) or Nonneuronal (S) Neural Crest Cells, Advances in Neroblastoma Research. *4:* 253-259, 1994.

240. 241. Biedler JL, Helson L, Spengler BA. Morphology and growth, tumorigenicity and cytogenetics of human neuroblastoma cells in continuous culture. Cancer Res 1973; 33: 2643-2652

241. 242. Singh J, Kaur G. Transcriptional regulation of polysialylated neural cell adhesion molecule expression by NMDA receptor activation in retinoic acid-differentiated SH-SY5Y neuroblastoma cultures. Brain Res 2007; 1154: 8-21

242. 243. Fagerstrom S, Pahlman S, Gestblom C, Nanberg E. Protein kinase C-epsilon is implicated in neurite outgrowth in differentiating human neuroblastoma cells. Cell Growth Differ 1996; 7: 775-785.

243. 244. Brunetti V, Maiorano G, Rizzello L, Sorce B, Sabella S, et al. Neurons sense nanoscale roughness with nanometer sensitivity. PNAS 107(14):6264-6269, 2010.

244. 245. Carlsson J, Gabel D, Jarsson E, et al. Protein-coated agarose surfaces for attachment of cells. In vitro cellular and developmental biology - Plant 15(11):844-850, 1979.

245. 246. Hirokazu Kaji, Masamitsu Kanada, Daisuke Oyamatsu, Tomokazu Matsue, and Matsuhiko Nishizawa. Microelectrochemical Approach to Induce Local Cell Adhesion and Growth on Substrates. *Langmuir*, 2004, *20* (1), pp 16–19

246. 247. Buttiglione et al.,Behaviour of SH-SY5Y neuroblastoma cell line grown in different media and on different chemically modified substrates. Biomaterials, Vol 28, Issue 19, July 2007, pp. 2932-2945.

247. 248. Yeung T, Georges PC, Flanagan LA, Marg B, et al. Effects of substrate stiffness on cell morphology, cytoskeletal structure, and adhesion. Cell Motility and the Cytoskeleton 60:24-34, 2005.

248. 249. Shannon, S.G., Moran, A.W., Shackelford, L.C., Mason, K.T., 1995. Effect of Vibration Frequency and Amplitude on Developing Chicken Embryos. Biodynamics Research Division, United States Army Aeromedical Research Laboratory (USAARL) Report No. 95-1.

249. 250. Taggart, L.C., Alem, N.M., Frear, H.M, 1991. Effect of Vibration Frequency and Acceleration Magnitude of Chicken Embryos on Viability and Development, Phase I. Biodynamics Research Division, United States Army Aeromedical Research Laboratory (USAARL) Report No. 91-1.

250. 251. Vladimir, S., Koloman, B., Vladimir, P., 1982. Effect of vibration on the hatchability and mortality of embryoes of Japanese quails. Polnohospodarstvo 28,6.

251. 252. Coucke, P., Dewil, E., Decuypere, E., De Baerdemaeker, J., 1999. Measuring the mechanical stiffness of an eggshell using resonant frequency analysis. BR Poult Sci 40(2), 227–232.

252. 253. Coucke, P., 1998. Assessment of some physical egg quality parameters based on vibration analysis. PhD Thesis, Katholieke Univ. Leuven, Belgium.

253. 254. Coucke, P., De Ketelaere, B., De Baerdemaeker, J., 2003. Experimental Analysis of the dynamic, mechanical behaviour of a chicken egg. J. Sound Vib. 266(3), 711-721.

254. 255. Bain, M.M., Fagan, A.J., Mullin, J.M., McNaught, L., LcLean, J., Condon, B., 2007. Noninvasive Monitoring of Chick Development in Ovo Using a 7T MRI System from Day 12 of Incubation Through to Hatching. J. Magn. Reson Imaging 26, 198-201.

255. 256. Heylen, W., Lammens, S., Sas, P., 1998. Modal Analysis Theory and Testing, KULeuven (ISBN: 90-73802-61-X).

256. 257. Forgacs, F., Foty, R.A., Shafrir, Y., Steinberg, M.S., 1998. Viscoelastic Properties of Living Embryonic Tissues: a Quantitative Study. Biophys. J. 74, 2227-2234.

257. 258. Haba, G., Nishigori, H., Tezuka, Y., Kagami, K., Sugiyama, T., Nishigori, H., 2011. Effect of antithyroid drug on chick embryos during the last week of development: Delayed hatching and decreased cerebellar acetylcholinesterase activity. J. Obstet. Gynaecol. Res. Vol. 37, No. 11, 1549–1556.

258. 259. Xu, G., Kemp, P.S., Hwu, J.A., Beagley, A.M., Bayly, P.V., Taber, L.A., 2010. Opening Angles and Material Properties of the Early Embryonic Chick brain. J. Biomech. Eng. 132, 011005-1 to 011005-7.

259. 260. Fuellekrug, U., 2008. Computational of real normal modes from complex eigenvectors. Mech. Syst. Signal Process 22(1), 57-65.

260. 261. Breitbach, E.J., 1973. A semi-automatic modal survey test technique for complex aircraft and spacecraft structures. Proceedings of the 3rd ESA Testing Symposium, 519-528.

261. 262. Van Woensel, G., Verdonck, E., Snoeys, R., De Baerdemaeker, J., 1984. Measuring the mechanical properties of apple tissue using modal analysis. J. Food Process Eng. 10, 151-163.

262. 263. Chester, W.L., Wilkie, W.K., Paul, H.M., 1997. Rotating Shake Test and Modal Analysis of a Model Helicopter Rotor Blade. NASA TM- 4760.

263. 264. Hermans, L., Van Der Auweraer, H., 1999. Modal testing and analysis of structures under operational conditions: Industrial applications, Mech. Syst. Signal Process13, 193-216.

264. 265. Yang, J.P., Chen, S.X., 2002. Vibration predictions and verifications of disk drive spindle system with ball bearings. J. Comput. Struct. 80, 1409-1418.

265. 266. Meirovitch, L., 1967. Analytical methods in vibrations. 1st Edn, Macmillan Publishing Co., Inc., NY, USA, pp:135-154.

266. 267. Allemang, R.J., Brown, D.L., 2002. Experimental Modal Analysis. Chap. 21 In: Harris' Shock and Vibration Handbook, 5th edition, Edited by: Harris C.M. and Piersol A.G., McGraw-Hill.

267. 268. Voronov DA, Taber LA. Cardiac Looping in Experimental Conditions: Effects of Extraembryonic Forces. Dev Dyn 2002;224:413–421. [PubMed: 12203733]

268. 269. Ilinskii YA, Meegan GD, Zabolotskaya EA, Emilianov SY. Gas bubble and solid sphere motion in elastic media in response to acoustic radiation force. J. Acoust. Soc. Am. 117, 2338-2346, 2005.

269. 270. Kennedy, C.C., Pancu, C.D., 1947. Use of vectors in vibration measurement and analysis. J. Aeronaut. Sci. 14, 603-625.

Appendix A: Index of biological and medical terms used in this thesis

Antigenic: something that is of or related to antigen. An antigen is a substance that when introduced into the body stimulates the production of an antibody.

Antineoplastic: acting to prevent, inhibit or halt the development of a tumor.

Apoptosis: process of programmed cell death that may occur in multicellular organisms.

Carcinogenesis: process by which normal cells are transformed into cancer cells.

Chemotherapy: treatment of cancer with an antineoplastic drug or with a combination of such drugs into a standardized treatment regimen.

Cell differentiation: process by which a less specialized cell becomes a more specialized cell type.

Cytokines: small cell-signaling protein molecules that are secreted by numerous cells and are a category of signaling molecules used extensively in intracellular communication.

Cytophysiology: the study of the biochemical processes involved in the functioning of individual cells.

Downregulated genes: genes that regulate some aspect of the cell or body by downing the production (or sequencing) of something.

Ectomesenchyme: a mass of tissue consisting of neurocrest cells present in the early formation of an embryo.

Endocytosis: process by which cells absorb molecules (such as proteins) by engulfing them.

Fibroblast: a type of cell that synthesizes the extracellular matrix and collagen, the structural framework (stroma) for animal tissues, and plays a critical role in wound healing.

Genomics: a discipline in genetics concerned with the study of the genomes of organisms. The genome is the entirety of an organism's hereditary information.

Immunocytochemistry: a common laboratory technique that uses antibodies that target specific peptides or protein antigens in the cell via specific antigenic determinants **Immunofluorescence**: a technique used for light microscopy with a fluorescence microscope and used primarily on biological samples.

Immunotherapy: medical term defined as the treatment of disease by inducing, enhancing, or suppressing an immune response.

Macrophage activation: process of altering the morphology and functional activity of cells produced by the differentiation of monocytes in tissues, so that they become avidly phagocytic.

Metabolomics: scientific study of chemical processes involving the intermediates and products of the set of chemical reactions that happen in the cells of living organisms to sustain life.

Metastasis: spread of a disease from one organ or part to another non-adjacent organ or part.

Neuroblastoma: most common extracranial solid cancer in childhood and most common cancer in infancy.

Oncolytic agent: an agent that preferentially destroys cancer cells.

Phagocytosis: the engulfing of microorganisms or other cells and foreign particles by white blood cells that protect the body.

Pharmacogenomics: branch of pharmacology which deals with the influence of genetic variation on drug response in patients by correlating gene expression with a drug's efficacy or toxicity.

Phenotype: composite of an organism's observable characteristics or traits such as its morphology, development, biochemical or physiological properties, behavior, and products of behavior.

Primer: a strand of nucleic acid that serves as a starting point for DNA synthesis.

Proteins: vital parts of living organisms that are the main components of the physiological transformation of cells.

Proteomics: large-scale study of proteins, particularly their structures and functions.

Sympathoblast: a pluripotential cell in the embryo that will develop into a sympathetic nerve cell.

Toxicogenomics: field of science that deals with the collection, interpretation and storage of information about gene and protein activity within particular cell or tissue of an organism in response to toxic substances.

Transcription regulation: change in gene expression levels by altering transcription rates.

Transdifferentiation: process where one mature biological cell transforms into another mature biological cell without undergoing an intermediate pluripotent state or progenitor cell type.

Trypsinization: a process of using trypsin, a proteolytic enzyme which breaks down proteins, to dissociate adherent cells from the vessel in which they are being cultured.

Upregulated genes: genes that regulate some aspect of the cell or body by upping the production (or sequencing) of something.

Western blot: a widely accepted analytical technique used to detect specific proteins in the given sample of tissue homogenate or extract.